

Alma Mater Studiorum – Università di Bologna

DOTTORATO DI RICERCA IN

Ingegneria Biomedica, Elettrica e dei Sistemi (IBES)
Curriculum in Bioingegneria

Ciclo XXXI

Settore Concorsuale: 09/G2

Settore Scientifico Disciplinare: ING-INF/06

EEG-BASED BRAIN-COMPUTER INTERFACES FOR
NEUROREHABILITATION AND CONTROL

Presentata da: Valeria Mondini

Coordinatore Dottorato

Prof. Daniele Vigo

Supervisore

Prof. Angelo Cappello

Co-supervisore

Dott.ssa Anna Lisa Mangia, Ph.D.

Esame finale anno 2019

External reviewers

Dott.sa Laura Astolfi, PhD

Neuroelectrical Imaging and Brain Computer Interface Laboratory, Fondazione Santa Lucia
IRCCS, Rome, Italy

Prof. Gernot Müller-Putz

Institute of Neural Engineering, Graz University of Technology, Graz, Austria

Overview

The research field of this dissertation are noninvasive, electroencephalography (EEG)-based, Brain-Computer Interfaces (BCIs), and their use for both neurorehabilitation and control purposes.

Brain-Computer Interfaces are systems enabling a straightforward communication between the brain and the outside, by recording the neural activity and directly translating it into control signals for various types of devices (e.g. a robotic arm, a machine, or a computer). Given their independence from the natural neuromuscular pathways, BCIs have long been envisioned as tools to restore communication and control in patients with severe motor impairments. In addition, BCIs have recently emerged in the context of neurorehabilitation, where they are employed to objectify the desired modulations of the neural features, to guide the practice and boost rehabilitation.

This dissertation includes several research activities from the two above-mentioned contexts. Each study builds up on the advancements of previous research and introduces a further step, either by investigating new configurations of the available technology (chapter 2), introducing some novel design elements (chapter 3), contributing into the practical implementation of new approaches (chapter 4), or improving the efficiency of available algorithms (chapter 5).

The work is organized into five chapters. **Chapter 1** serves as introduction to the field of EEG-based BCIs and their use for neurorehabilitation and control purposes. After introducing the general concept of BCI, the chapter briefly reviews the possible invasive and noninvasive recording techniques, then focuses on the EEG, its rhythms, and challenges (e.g. the sensitivity to artifacts), and finally introduces the four classes of EEG signals viable for BCI control. In the last two sections of the chapter, the concepts of BCIs for neurorehabilitation and control are introduced, linking to chapter 2 in the first case, and presenting the line of arguments of chapter 3, chapter 4 and chapter 5 in the second case. In the last four chapters of the thesis, the core of the research activity is described. The content of chapter 2, chapter 3 and chapter 5 is based on published scientific papers, so the original article structure was kept, and the same organization was given to chapter 4. This way, each chapter is also self-contained, and can be read independently from the others.

In **chapter 2**, a novel combination of two neurorehabilitation tools is investigated, namely i) BCI-guided motor imagery training and ii) transcranial direct current stimulation (tDCS). As tDCS can modulate event-related desynchronization (ERD), i.e. the neural signature of motor imagery detected by the BCI, a combination of the techniques has been recently suggested. One limitation of the approach is that the area targeted for stimulation is the same from which the BCI signal is acquired. As tDCS may induce artifacts in the proximal EEG electrodes, stimulation is usually given *before* BCI training, although the practice is not optimal due to the quickly vanishing effects of tDCS over time. In order to promote the practicality of the combination, the aim of our study was testing whether contralateral tDCS could have interhemispheric effects on the spectral power of the unstimulated hemisphere, possibly mediated by transcallosal connections, and whether such effects could be used to enhance ERD. The study involved the recording of twenty healthy volunteers, and the influence of tDCS over spectral power and ERD was assessed.

Chapter 3 and **chapter 4** are ideally in prosecution, and in line with the progressive effort to make BCI control more natural and intuitive.

The work in **chapter 3** describes a BCI control system based on the modulation of sensorimotor rhythms (SMR) by means of different motor imaginations. The work lies in the category of co-adaptive BCIs, aiming at the improvement of user training through short calibration and adaptivity of the system. The work in **chapter 3** integrates the already explored concepts of co-adaptive BCIs, introducing some novel elements to improve the flexibility and tailoring of the design.

The activity in **chapter 4** was carried out during an internship at the Institute of Neural Engineering, Graz University of Technology, Austria. The chapter lies in the context of the development of a new control framework for noninvasive BCIs, to allow for intuitive and natural control of a neuroprosthesis. The idea is to decode the trajectories of real or imagined movements from the EEG, and use these as input for the prosthetic device. Feasibility of EEG decoding had been shown in previous studies although, so far, it had only been performed offline. In **chapter 4**, a system enabling for the first time online control of a robotic arm by means of continuously EEG-decoded movements is presented. The chapter details the methods used for the purpose, and discusses the results from ten healthy participants, in reference to the findings of previous offline studies.

Chapter 5 closes the thesis with a case-of-study of a four-class BCI based on SSVEP. The chapter presents two simple but effective ways to improve SSVEP recognition based on Canonical Correlation Analysis (CCA). The two variations could significantly improve classification accuracy with no or minimal impact on computational load, and no required additional user training. When used in combination, they led to accuracy increments of 7-8% on average and 25-30% peak. The possible reasons underlying these increments are also discussed in the chapter.

Summary

Overview	4
Summary	8
Chapter 1. Brain-Computer Interfaces for neurorehabilitation and control	13
1.1 Brain-Computer Interfaces	13
1.2 Neural recording techniques.....	14
1.2.1 Intracortical recordings	15
1.2.2 Electrocorticography (ECoG)	16
1.2.3 Magnetoencephalography (MEG) and electroencephalography (EEG).....	16
1.2.4 Functional Magnetic Resonance Imaging (fMRI) and functional Near-Infrared Spectroscopy (fNIRS).....	16
1.3 Electroencephalography.....	17
1.3.1 EEG, origin and measurement	17
1.3.2 EEG rhythms	18
1.3.3 EEG artifacts (and how to deal with them).....	19
1.4 EEG signals for BCI control.....	20
1.4.1 Slow Cortical Potentials	21
1.4.2 P300 evoked potential.....	21
1.4.3 Steady-State Visual Evoked Potentials (SSVEPs).....	23
1.4.4 Sensorimotor Rhythms (SMR).....	23
1.5. Brain-computer interface for neurorehabilitation	25
1.5.1 Stroke patients.....	26
1.5.2 Upper limb rehabilitation	26
1.5.3 Mental practice in the form of motor imagery, and the role of BCIs	27
1.5.4 Transcranial direct current stimulation (tDCS)	27
1.5.5 Combining tDCS and BCI-guided MI training.....	28
1.6. Brain computer interfaces for control.....	28
1.6.1 Towards a more intuitive and natural control of noninvasive BCIs.....	29
1.6.2 Case of study: improving the efficacy of CCA for SSVEP recognition	32

Chapter 2. Contralateral tDCS during BCI-guided motor imagery training	34
2.1 Introduction	34
2.2 Methods	37
2.2.1 Participants	37
2.2.2 tDCS stimulation	37
2.2.3 EEG recording	38
2.2.4 Experimental paradigm	39
2.2.5 The neurofeedback software	40
2.2.6 Offline analyses	43
2.2.7 Statistical analyses	44
2.3 Results	45
2.3.1 tDCS effect on ERDs	45
2.3.2 tDCS effect on spectral power	47
2.3.3 Side-effects questionnaire	49
2.4 Discussion	49
2.4.1 tDCS effect on ERDs	50
2.4.2 tDCS effect on spectral power	52
2.4.3 Limitations of the study and generalizability to a patient population	54
2.5 Conclusion	55
2.6 Supplementary Material	56
Chapter 3. A co-adaptive BCI based on motor imagery	59
3.1 Introduction	59
3.2 Methods	60
3.2.1 Signal acquisition and preprocessing	60
3.2.2 The online BCI system: the three modules	61
3.2.3 Experimental setup and participants	66
3.2.4 Experimental paradigm (the “flexible” training session)	67
3.2.5 System evaluation	67
3.3 Results	71
3.3.1 Accuracy	71

3.3.2 Time effect.....	71
3.3.3 Efficacy of the adaptive thresholds.....	72
3.4 Discussion	74
3.4.1 Accuracy.....	74
3.4.2 Time effect.....	74
3.4.3 Efficacy of the adaptive thresholds.....	74
3.4.4 Possible improvements.....	75
3.4.5 Overall comments	75
3.5 Conclusion.....	76
3.6 Appendix.....	77
3.7 Supplementary Material.....	79

Chapter 4. Online decoding of hand movement for the natural control of an assistive robotic arm.....	83
4.1 Introduction.....	83
4.2 Methods.....	84
4.2.1 Participants	84
4.2.2 Experimental setup	84
4.2.3 Experimental procedure.....	85
4.2.4 Data recording and processing.....	87
4.2.5 Decoder fitting and Kalman filter	91
4.2.6 Decoding performance and Kalman filter effect	94
4.2.7 Pattern source mapping.....	94
4.2.8 Source space statistics	95
4.3 Results.....	96
4.3.1 Decoder correlations	96
4.3.2 Effect of the Kalman filter	98
4.3.3 Amplitude of the decoder output.....	99
4.3.4 Source space statistics	100
4.3.5 Cross-correlation curves	102
4.4 Discussion	103
4.4.1 Decoding performance and Kalman filter effect	103

4.4.2 Amplitude of the decoder output.....	104
4.4.3 Source space analysis: tuning of neural activity to the velocities.....	105
4.4.4 Activation of the parieto-occipital areas, and efficacy of the eye artifact correction algorithm	106
4.4.5 Feedback effect and adaptation.....	107
4.5 Limitations.....	108
4.6 Conclusion.....	108
4.7 Supplementary Material.....	109
Chapter 5. Two simple but effective ways to improve SSVEP recognition based on Canonical Correlation Analysis.....	111
5.1 Introduction.....	111
5.2 Methods.....	112
5.2.1 The standard CCA method for SSVEP recognition	112
5.2.2 Variation 1: number of considered canonical correlations.....	113
5.2.3 Variation 2: pre-processing with sinc-windowing.....	114
Data acquisition	115
5.2.5 Experimental paradigm	115
5.2.6 Performance evaluation.....	116
5.2.7 Statistical analyses.....	116
5.3 Results.....	116
5.4 Discussion	121
5.5 Conclusion.....	123
General conclusions.....	125
Acknowledgments	129
References.....	131

Chapter 1. Brain-Computer Interfaces for neurorehabilitation and control

In this chapter, I will review some of the basic concepts of EEG-based Brain-Computer Interfaces, which I believe may be useful to better understand and frame the work. After briefly introducing the definition of Brain-Computer Interfaces, I will review some possible invasive and noninvasive neural recording techniques, focus on the EEG, with its rhythms and artifacts, and finally introduce the four classes of EEG signals viable for BCI control. In the last two sections of the chapter, I will introduce the concept of Brain-Computer Interfaces for neurorehabilitation, linking to chapter 2, and finally the concept of Brain-Computer Interfaces for control, linking to chapter 3, chapter 4 and chapter 5.

1.1 Brain-Computer Interfaces

According to a very general definition by Johnatan Wolpaw in (Wolpaw and Wolpaw, 2012), a Brain-Computer Interface is a system able to “measure and convert the activity of the central nervous system (CNS) into an artificial output to replace, restore, emphasize, substitute or improve the natural CNS outputs, thus changing the interaction between the brain and the internal or the external environment”. In other words, a BCI is a system able to directly translate the neural activity into commands for various types of devices (e.g. a computer, a prosthesis, a machine...), without needing the mediation of peripheral nerves and muscles (Wolpaw et al., 2000).

For their properties, BCIs have long been envisioned as tools to restore communication and control in patients with severe neuromuscular disorders or, more recently, to foster neurorehabilitation, i.e. to facilitate recovery of neural functions (Chaudhary et al., 2016).

From a conceptual point of view, a BCI system is composed of three parts (Figure 1.1): i) signal acquisition, ii) signal processing, and iii) feedback.

After being recorded from the user, either invasively or noninvasively, the signal is processed to extract the information, and convert it into commands for the device to be controlled. The processing step can be further decomposed in three parts:

- i) pre-processing: usually consisting in spatial and temporal filters, this step encompasses the operations to enhance the significant components of the signal, better the signal-to-noise ratio, or attenuate artifacts
- ii) feature extraction: extraction of a set of meaningful features from the signal to be classified, as e.g. the spectral powers in a particular frequency band
- iii) classification: using machine learning techniques, the features are classified and translated into control signal for the device

As a final element, feedback is the tangible consequence of the brain activity (e.g. movement/behavior of the neuroprosthesis, of a cursor on the screen, etc), allowing the user to learn voluntary modulation of his/her neural activity and gain control over the system.

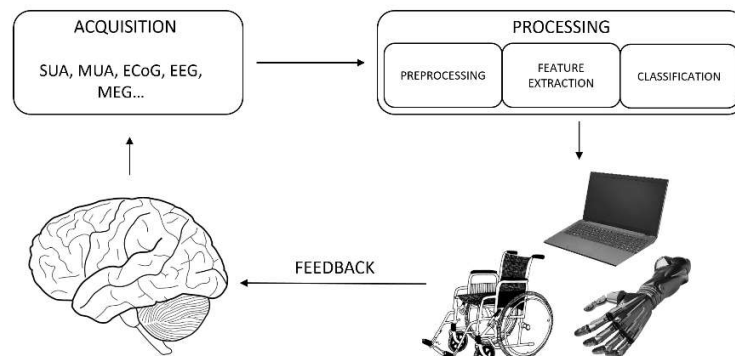


Figure 1.1 Conceptual scheme of a Brain-Computer Interface.

1.2 Neural recording techniques

One possible classification of the BCI systems may be based on the underlying neural recording technique. Recordings may be either invasive or noninvasive, and may either monitor the i) electrophysiological or the ii) hemodynamic activity of the brain (Nicolas-Alonso and Gomez-Gil, 2012).

With the term “electrophysiological activity”, one refers to the exchange of information between neurons through electro-chemical transmitters (Baillet et al., 2001). The cumulative change in electromagnetic field resulting from the communication between neuronal assemblies can be captured through several recording modalities (Figure 1.2), like the invasive intracortical recordings and electrocorticography

(ECoG), or the noninvasive magnetoencephalography (MEG) and electroencephalography (EEG).

The “hemodynamic signal” is a consequence of the fact active neurons require more oxygen from the blood with respect to inactive areas. This results in a local variation of the ratio between oxyhemoglobin and deoxyhemoglobin, proportional to the level of activity of the region (Laureys et al., 2009). This ratio, and therefore the level of activity, is quantifiable by methods like functional magnetic resonance imaging (fMRI) and functional near infrared spectroscopy (fNIRS).

The focus of this thesis are EEG-based Brain-Computer Interfaces. However, as some of the other terms will appear in the work, a very brief introduction on each recording technique will be given below.

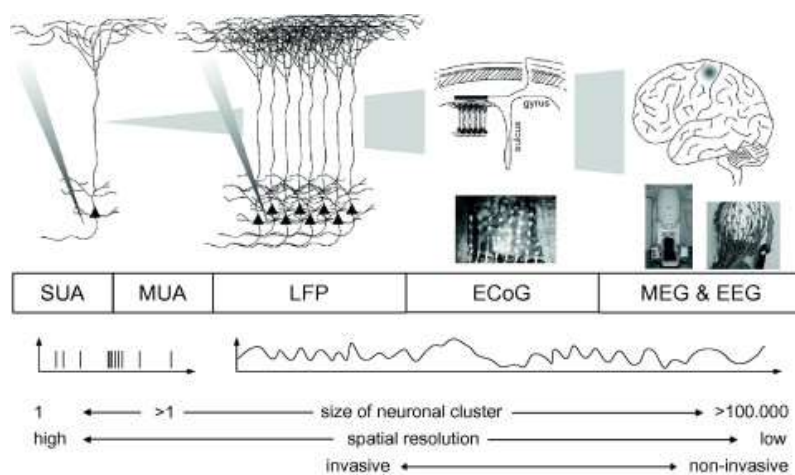


Figure 1.2 Overview of the electrophysiological recording techniques from invasive intracortical recordings, to ECoG, MEG, and EEG, and qualitative comparison of spatial resolution (figure from (Waldert et al., 2009)).

1.2.1 Intracortical recordings

Intracortical recordings are obtained through invasive implantation of microelectrode arrays into the cortex. This permits to capture the spiking activity and local field potentials of the neurons close to each electrode tip (Waldert et al., 2009). If applying different processing pipelines, three possible signals can be collected, notably: i) single-unit activity (SUA), ii) multi-unit activity (MUA), and iii) local field potentials (LFP). Intracortical recordings provide the best spatial and temporal resolution and are portable systems. However, their invasivity and the possible reaction of the brain tissue to the implant (Polikov et al., 2005) limit their use.

1.2.2 Electrocorticography (ECoG)

Slightly less invasive than intracortical recordings, in electrocorticography (ECoG) a grid of electrodes is placed on the cortical surface (instead of penetrating the brain). The electrode array may be laid inside (subdural) or outside (epidural) the dura mater (Nicolas-Alonso and Gomez-Gil, 2012), while the ECoG recordings reflect the overall activity of the neuronal population under each electrode.

Spatial resolution is lower than intracortical recordings, but still high. Due to their invasivity and problems in the long-term stability (Hill et al., 2006), ECoG implants are not widespread, although they are sometimes used in epileptic patients, temporally implanted for the localization of epileptic sources before surgery.

1.2.3 Magnetoencephalography (MEG) and electroencephalography (EEG)

Similarly to ECoG, but with lower amplitude and spatial resolution, both magnetoencephalography (MEG) and electroencephalography (EEG) capture the activity of large neuronal populations, although noninvasively from outside the head (Waldert et al., 2009).

While EEG reflects the electrical activity of pyramidal neurons in the cortex (He, 2007) (see the next section for more details), MEG reflects the related magnetic fluctuations, captured with superconducting sensors (Min et al., 2010). One advantage of measuring magnetic fields is that they are less susceptible to distortion when crossing the skull and the scalp (Salmelin et al., 1995). Nevertheless, for its need to be carried out in magnetically shielded rooms and the immobility of the recording system (until very recently, see the first portable system presented in (Boto et al., 2018)), MEG recordings so far have been limited to research purposes.

1.2.4 Functional Magnetic Resonance Imaging (fMRI) and functional Near-Infrared Spectroscopy (fNIRS)

In contrast to the previous recording techniques, functional magnetic resonance (fMRI) and functional near-infrared spectroscopy (fNIRS) provide an indirect measure of neural activity based on the blood oxygenation level, exploiting the magnetic (fMRI) or optical (fNIRS) properties of the oxygenated and deoxygenated forms of hemoglobin (Nicolas-Alonso and Gomez-Gil, 2012). Temporal resolution of both techniques is intrinsically limited by the physiological delay of the hemodynamic response, having latencies from three to six seconds (Weiskopf et al., 2004). Although benefiting of a high spatial resolution (deCharms et al., 2004), fMRI is not suitable for practical BCIs applications, due to the bulky and expensive hardware. On the other hand, fNIRS is increasingly attracting attention, for its portability and ability to complement the electrophysiological information, for example in the hybrid fNIRS-EEG systems (Hong et al., 2018).

1.3 Electroencephalography

1.3.1 EEG, origin and measurement

Electroencephalography (EEG) is a noninvasive recording technique, capturing the activity of large neuronal populations from an array of electrodes placed the scalp.

EEG rhythms are largely believed to be representative of the synchronous activity of pyramidal neurons in the cortex (Baillet et al., 2001). When communicating between each other, neurons behave as current dipoles, being crossed by intracellular currents and experiencing a difference in potential at their ends. For their properties of synchronous activity, parallel arrangement with respect to each other, and perpendicular orientation with respect to the cortex, the electrical fields from the pyramidal neurons can be effectively summated, giving birth to a cumulative signal which can be measured from outside the scalp (Da Silva, 2009)(Figure 1.3).

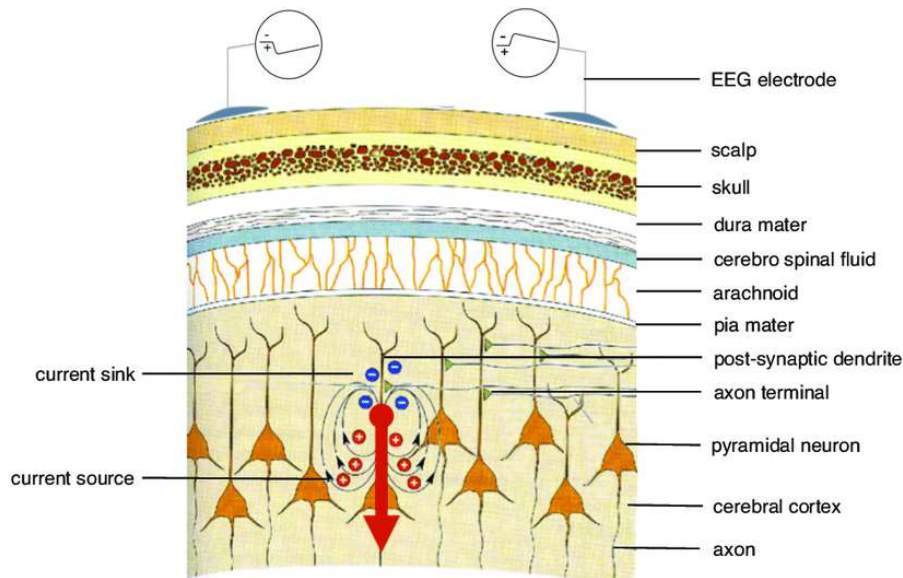


Figure 1.3. Pyramidal neurons arrangement and EEG generation according to the dipole model (figure from (Strobbe, 2015))

The EEG signal is obtained as the difference in potential between two electrodes, of which at least one is placed on the scalp. The minimal configuration for an EEG measurement consists of one active and one reference electrode, together with a third electrode serving as ground for the two. Electrodes are placed on the scalp according to an international system, defining the locations' names at the relative distances with respect to four anatomical landmarks (namely the nasion, the inion, and the two preauricular points) (Klem et al., 1999). The original 10-20 international system (Klem

et al., 1999), so called because the electrode locations are placed at the 10% or 20% of the distance between the landmarks, originally defined the position and names of 21 electrode locations (Figure 1.4). Recent extensions to 10-10 and 10-5 can define up to 300 locations (Nuwer et al., 1998; Oostenveld and Praamstra, 2001).

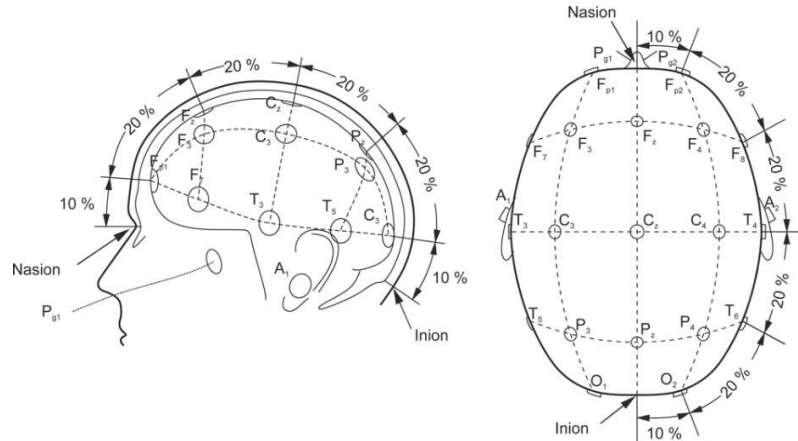


Figure 1.4. The 10-20 system for EEG recordings. The letters in each location correspond to specific brain regions (A for the ear lobes, C for the central, P for the parietal, F for the frontal, Fp for the frontal polar, and O the occipital region).

Electrodes are usually made of silver chloride (AgCl) and may be either active or passive, depending on the presence or not of preamplification circuits (Teplan, 2002). Electrode-scalp contact impedance should be kept between 1 k Ω and 10 k Ω in order to record an accurate signal (Usakli, 2010). For this reason, the interposition of conductive gel between electrode and skin is usually required.

1.3.2 EEG rhythms

The EEG spectrum (0.5 to \sim 100Hz) is commonly divided into six frequency bands, related to different biological significance and distribution over the scalp. These bands are named delta (δ), theta (θ), mu (μ), alpha (α), beta (β) and gamma (γ). Relevant features of each band are briefly given below.

In the following, the EEG bands will be defined according to their average frequency limits. A relative definition of the bands with respect to the Individual Alpha Frequency (IAF) is also possible, to account for the inter-subject variability of the alpha peak (Klimesch, 1999).

Delta band (δ): delta is the EEG frequency range below 4Hz, and it tends to be the highest in terms of amplitude. It is normally seen in the posterior areas in babies, while the amplitude tends to decrease with the increase of age. In adults, delta rhythms are normally seen frontally during slow wave sleep, while an increased activity in the awake person may be associated to neurological diseases (Niedermeyer and Silva,

2005). Recently, the EEG delta band has also been shown to encode information related to the trajectories of voluntary movement (Robinson and Vinod, 2016).

Theta band (θ): theta is the frequency band between 4Hz and 7Hz, and it is normally more enhanced in young children. Theta rhythms may be seen in drowsiness in adults, they might arise in meditation (Bazhenov et al., 2002), and may be associated with a wide range of cognitive processes, like mental calculation (Fernández et al., 1995), maze task demands (Caplan et al., 2001), or conscious awareness (Klimesch et al., 2001).

Alpha band (α): alpha is the frequency range between 8 Hz to 12Hz. It was the first rhythmic activity observed in the EEG by its inventor, Dr Hans Berger (Berger, 1929). The activity was first observed in (Berger, 1929) in the posterior areas, with closed eyes or relaxation, and attenuated when opening the eyes. EEG rhythms in the alpha range have historically been considered resting rhythms for the brain (Pfurtscheller et al., 1997; Suffczynski et al., 2001) and, more recently, related to active inhibition and timing of processes (Klimesch et al., 2007).

Mu rhythm (μ): the mu rhythm is a characteristic activity in the alpha range, with a typical frequency peak in the 9-11Hz band and a topographical distribution over the sensorimotor areas. The rhythm characteristically attenuates (desynchronizes) with the real or imagined movement of the contralateral arm (Pfurtscheller and Silva, 1999), as explained in the next sections.

Beta band (β): beta is the frequency range from 12Hz to about 30Hz. It is usually present on both hemispheres and most evident frontally. Beta activity is closely related to motor behavior, and generally desynchronized during active movements (Pfurtscheller and Silva, 1999), and synchronized after the cessation of the same ("beta rebound").

Gamma band (γ): gamma rhythms are the ones above 30Hz. They are thought to represent binding of different neuronal populations together into a network for the purpose of carrying out a certain cognitive or motor function (Niedermeyer and Silva, 2005; Ursino et al., 2009). Recently, gamma rhythms have also been associated with trajectory encoding, although to a lesser extent with respect to the delta band (Korik et al., 2014).

1.3.3 EEG artifacts (and how to deal with them)

As the amplitude of EEG is in the range of 10 to 100 μ V, it is very susceptible to noise coming from various external and internal factors. In the following, the most common artifactual sources will be reviewed.

Ocular-related artifact: ocular-related artifacts are caused by the difference in potential between the cornea and the retina, which is quite large with respect to brain potentials. As the eyes move, either voluntarily (e.g. tracking of an object) or

involuntarily (e.g. saccadic movements, blinks), they generate a potential (the electro-oculographic potential, EOG) interfering with several EEG locations, and most prominent in the frontopolar and frontal ones. Ocular artifacts affect the same frequency bands of eye movements, i.e. the delta (0-4Hz) and theta (4-7Hz) bands. One way to deal with these artifacts is by experimental design, i.e. by instructing participants to keep their gaze fixed during the recordings. Alternatively, eye artifact removal algorithms were developed for the purpose (Kobler et al., 2017), with the goal to subtract ocular activity, while minimally removing the underlying brain waves.

Muscle-related artifacts: muscle-related artifacts are generated by the EMG activity and interfere with the highest part of the spectrum (>20Hz). They are particularly evident over the temporal locations, due to chewing movements or to even subtle activity of the jaw muscles. Several algorithms have been proposed for muscular artifact attenuation (Urigüen and Garcia-Zapirain, 2015), most of them based on blind-source-separation methods (Jung et al., 1998, 2000).

Heart beat: the electrical field generated by the heart (electrocardiogram, ECG) can directly interfere with the EEG recordings. The ECG interference depends on the orientation of the equivalent heart dipole, and may affect several electrodes simultaneously. As such, re-referencing of the signals to common average reference (CAR) or Laplacian derivations can drastically attenuate the ECG artifacts (McFarland et al., 1997a).

Movement artifact: movement-related mechanical artifacts, associated with head movements or locomotion, can have amplitudes an order of magnitude larger than the underlying brain EEG signals (Gwin et al., 2010). Mechanical pulling of the wires on the electrodes, with the consequent temporary change of contact impedance, induces the artifacts. Body and head movements may induce slow potential shifts, which might be misinterpreted as delta activity (Anderer et al., 1999), or even higher frequency artifacts if induced by e.g. locomotion (Gwin et al., 2010). Several removal algorithms have been developed for the purpose (Gwin et al., 2010; Kim et al., 2015).

Power-line artifact: power line interference (50/60Hz) is caused by capacitive coupling of the body with the environment, and can be removed by notch filters, together with proper grounding and shielding of the recording system.

1.4 EEG signals for BCI control

This section will describe the four electrophysiological sources typically used in EEG-based BCIs, namely i) Slow Cortical Potentials, ii) P300, iii) Steady-State Visual Evoked Potentials (SSVEPs), iv) voluntary modulation of Sensorimotor Rhythms (SMR). One additional approach, which is being arising in recent years, investigates the possibility to directly infer movement trajectories from the low frequency components of the EEG, to provide a more natural and intuitive way of control (Müller-Putz et al., 2016). In

contrast to the first four established control signals, feasibility of the latter approach for online control is still object of investigation, being this at the cutting edge of noninvasive restorative BCIs. For these reasons, the latter will be introduced only later, in section 1.6 of this chapter, and will be the object of the research study described in **chapter 4**.

1.4.1 Slow Cortical Potentials

Slow Cortical Potentials (SCP) are small, slow shifts in EEG potential lasting from ~300ms to a few seconds (Birbaumer et al., 2000; Wolpaw et al., 2002). As such, SCPs are part of the EEG spectrum <1Hz. Slow cortical potentials are related to changes in the level of cortical activity in such a way that negative shifts correspond to an increased level of activity, while positive shifts correspond to a decrease (Wolpaw et al., 2002). It has been shown that, with training, both healthy and paralyzed patients could learn to voluntarily control SCPs, making it a viable control signal for the BCI (Birbaumer et al., 2000; Wolpaw et al., 2002).

One of the first BCIs using SCPs is the one from Birbaumer et al., presenting in year 2000 their “Thought Translation Device” (TTD) (Birbaumer et al., 2000), tested over five paralyzed patients. The TTD system was used both for the training of the person through operant conditioning and for communication, once classification accuracy consistently exceeded 75%. The system recorded the EEG signal from five electrodes and was completed by an eye tracker to remove ocular-related artifacts. During the first training phase, participants learned to control both positive and negative shifts. The feedback was the display of a cursor on the screen, with the additional positive reinforcement of a smiling face, as soon as the cursor reached the top/bottom. After training, the person could decide whether using positive or negative SCPs, thus continuing the training in the “free spelling” phase. In this last phase, each letter was selected by halving the alphabet from time to time, up to the selection of the desired character. Of the five patients tested, three reached the spelling stage, one of these after three weeks of training and the other two after a few months (Birbaumer et al., 2000). With a BCI of this type, a user with accuracies between 65% and 90% could write from 0.15 to 3 letters per minute (Wolpaw et al., 2002). Writing speed could be possibly improved by applying prediction algorithms of the most probable words based on the first typed letters (Birbaumer et al., 2000).

1.4.2 P300 evoked potential

P300 evoked potentials appear as small positive peaks due to infrequent visual, somatosensory, or auditory stimuli, whenever they occur, interposed to more frequent or routine stimuli (Wolpaw et al., 2002). P300 evoked potentials appear in the area of the parietal cortex about 300ms after the “weird” stimulus is presented. To explain

how P300 can be used in a BCI, one of the first systems of this type, by Farwell and Donchin in 1988, will be used as example (Farwell and Donchin, 1988).

In the (Farwell and Donchin, 1988) system, a 6x6 matrix of symbols was shown on the screen. The symbols could be letters or short commands, like “space” or “backspace” (Figure 1.5). The rows and columns of the matrix flashed one at a time every 125ms, while the user was asked to carefully count how many times the row or column with the desired symbol flashed. As the row/column of interest was an improbable event interposed to many more probable, these elicited P300, making it possible to identify the desired symbol (Farwell and Donchin, 1988; Wolpaw et al., 2002).

Although BCIs continued to evolve, the basic principle of P300-based systems remains the same, and similar to the one in (Farwell and Donchin, 1988). In people with vision problems, auditory stimuli have also been attempted (Furdea et al., 2009). One advantage of P300-based BCIs is that they do not require user training. The most “improbable” is the stimulus, the higher it the amplitude of P300 (Polich et al., 1996) however, if the user gets used to the odd stimulus, the amplitude is reduced and BCI performance may get worse (Ravden and Polich, 1999). One disadvantage of P300-based BCIs is the reduced information transfer rate, allowing the selection of only few characters per minute (Nicolas-Alonso and Gomez-Gil, 2012). Given indeed the small amplitude of the P300 peak, averaging operations over several repetitions are needed. Over the years, different strategies have been proposed to improve the accuracy of P300-based BCIs, including the use of more complex algorithms for classification of the evoked potentials (Rivet et al., 2009). In spite of the reduced information transfer rate allowed by P300-based BCIs, the signal has been successfully used in the years e.g. for the control of wheelchairs (see an example in (Iturrate et al., 2009)).

MESSAGE					
BRAIN					
Choose one letter or command					
A	G	M	S	Y	*
B	H	N	T	Z	*
C	I	O	U	*	TALK
D	J	P	V	FLN	SPAC
E	K	Q	W	*	BKSP
F	L	R	X	SPL	QUIT

Figure 1.5. Matrix of symbols used in the (Farwell and Donchin, 1988) study. On the top, the composed work “B-R-A-I-N”.

1.4.3 Steady-State Visual Evoked Potentials (SSVEPs)

Visual Evoked Potentials (VEP) are changes in the ongoing EEG activity, reflecting the processing of visual information in the brain (Sutter, 1992). As such, they are recordable from the parieto-occipital cortex after presentation of a visual stimulus (Wang et al., 2008).

Depending on the frequency of the visual stimuli presentation, we can distinguish between transient and steady-state visual evoked potentials. Transient VEPs (tVEPs) occur when the frequency of stimulus presentation is lower than 2 Hz, so that there is some gap between two consecutive stimulations. If the repetition rate is $>6\text{Hz}$, then the evoked potentials will overlap, giving origin to a steady-state visually evoked potential (SSVEP)(Lin et al., 2007). Transient VEPs may be evoked with different strategies, as long as they provoke changes in the visual field of the user. They may be for example i) *flash* stimuli, if they are emitted e.g. by flashing dots, or even ii) *pattern* stimuli, if they involve sudden appearance/disappearance of a pattern on the background, or the inversion of the same pattern (e.g. of a checkerboard) (Odom et al., 2004). SSVEP responses are induced by the same visual stimuli as tVEPs, but repeated over time.

The appealing feature of SSVEPs is that they present spectral power peaks at the same frequency of the visual stimulation and related harmonics (Nicolas-Alonso and Gomez-Gil, 2012). Consequently, if several flickering objects are simultaneously presented, an analysis of the EEG frequency content may permit to conclude which one the user is gazing at. Thanks to their high signal-to-noise ratio even without user training, SSVEPs are appealing for fast and reliable BCI control (Zhu et al., 2010), and have been extensively used e.g. for the selection of buttons/letters on the screen. An example of such systems can be found e.g. in (Middendorf et al., 2000).

Traditionally used methods perform SSVEP recognition based on power spectral density analysis (PSDA)(Lin et al., 2007). In PSDA-based approaches, spectral powers are estimated from the EEG signal at the target stimulation frequencies and used as a feature for classification (Cheng et al., 2002; Müller-Putz et al., 2005; Yijun et al., 2005). More recently, an effective and increasingly used approach (Bin et al., 2009; Pan et al., 2011; Zhang et al., 2012) has become the one based on Canonical Correlation Analysis (CCA), as explained in (Lin et al., 2007).

1.4.4 Sensorimotor Rhythms (SMR)

Sensorimotor rhythms (SMR) are EEG rhythms detectable over the primary motor and sensory cortex, covering the mu (8-13Hz) and beta (13-30Hz) bands, and reflecting the processing of sensory and motor information. SMR are modulated by motor tasks, although their success in the BCI field is probably related to their being modulated also by motor imagination (Jeannerod, 1995; McFarland et al., 2000; Pfurtscheller and Neuper, 1997; Pfurtscheller et al., 2006), with similar patterns.

Modulations of SMR rhythms may result from sensory stimulation, a motor act or its imagination, and may be of two types. They may be event-related desynchronization (ERD) or event-related synchronization (ERS), either they are related to a decrease (ERD) or increase (ERS) in spectral power (Pfurtscheller and Neuper, 2001; Pfurtscheller and Silva, 1999). The dynamics of brain oscillations can form even complex space-time patterns, so that in a specific location they may simultaneously occur e.g. a desynchronization at lower and synchronization at higher frequencies (Pfurtscheller and Neuper, 2001).

It is known that voluntary movement induces the desynchronization of both mu and beta rhythms (Pfurtscheller and Neuper, 1997). Desynchronization begins ~2 seconds before movement onset, in the hemisphere contralateral to the movement, and becomes symmetric with movement execution (Pfurtscheller and Neuper, 1997). As motor imagery involves brain regions and functions similar to the ones in movement programming and preparation (Jeannerod, 1995; Pfurtscheller and Neuper, 2001), contralateral ERD in the mu and beta bands could be observed during motor imagination as well (Pfurtscheller and Neuper, 1997). In addition to contralateral ERD, ipsilateral ERS in approximately the same frequencies could sometimes accompany motor imagination (Guger et al., 2000; Pfurtscheller and Neuper, 1997).

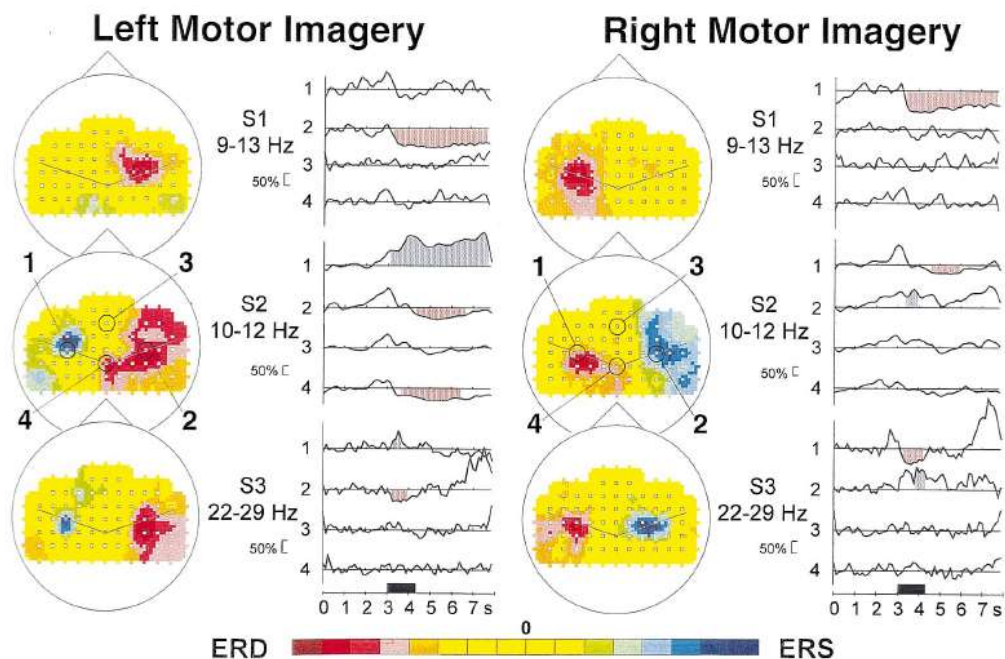


Figure 1.6. The ERD/ERS patterns during motor imagination of left and right hand in the three subjects of (Pfurtscheller and Neuper, 2001).

One important feature of SMR is their following a somatotopic organization (Pfurtscheller and Neuper, 2001), so that the patterns related to one imagination are different and distinguishable from the patterns of another one. As an example, Figure 1.6 shows the three subjects from the study in (Pfurtscheller and Neuper, 2001), during the imagination of the movement of their right vs left hand. For each subject, the frequency band with greatest differences between the two imaginations is highlighted. As previously explained, some subjects (e.g. the first one) may only report the contralateral ERD, while other ones (e.g. the second and the third one) may also show ERS on the ipsilateral side. When contrasting the two types of imaginations, it could be noted that the patterns are clearly distinguishable and, in this case, also symmetric. The basic idea of SMR-based BCIs is therefore to use several imaginations, inducing different SMR patterns, to be recognized and classified against each other to be used as control signal for the BCI (Guger et al., 2000).

Sensorimotor rhythms have been extensively explored in BCI research. The approach was one of the most used in the 1990s and 2000s, when the main research centers in the field, like Wadsworth (Wolpaw et al., 2000), Berlin (B. Blankertz et al., 2008), and Graz (G. Pfurtscheller et al., 2003), presented their BCI paradigms based on SMR modulation.

One limitation of SMR-based BCIs is that learning a stable, voluntary modulation of SMRs may be a non-intuitive and unnatural task, usually requiring from weeks to months of user training (Tan and Nijholt, 2010). To tackle this problem, co-adaptive BCI frameworks have been first proposed and, more recently, the novel approach of movement decoding is being investigated. The two approaches will be the focus of **chapter 3** and **chapter 4** of this thesis, as it will better introduced in the following section 1.6.

Apart from being used as a signal for BCI control, event-related desynchronization of sensorimotor rhythms has recently been used in neurorehabilitation, to objectify the engagement of the motor network during motor imagery. More details on this topic can be found in the next section and are the focus of the **chapter 2** presented later in the thesis.

1.5. Brain-computer interface for neurorehabilitation

Besides their employment for restoration of control, a recently emerging use of Brain-Computer Interfaces is in the area of neurorehabilitation (van Dokkum et al., 2015). With the term neurorehabilitation, one refers to the process aiming at the recovery from a neurological injury (i.e. stroke), to minimize or compensate the resulting functional alterations (Ganguly et al., 2013; Krucoff et al., 2016). In this context, BCIs may be used as a tool to objectify the desired patient's brain modulations, as he attempts to perform the desired motor task, or during mental rehearsal of the same

(van Dokkum et al., 2015). The goal is the recruitment of the desired brain areas, to promote neuroplasticity – i.e. the ability of the nervous system to reorganize its structure, function and connections (van Dokkum et al., 2015) – and enhance motor recovery.

In the following lines, I will introduce one of the main target populations of BCI-guided neurorehabilitation (i.e. stroke patients), and the two neurorehabilitation tools I focused on, i.e. motor imagery training and noninvasive brain stimulation based on transcranial direct current stimulation (tDCS). These elements will permit me to introduce the research activity later described in **chapter 2**. The content of **chapter 2** is based on the published work in (Mondini et al., 2018a).

1.5.1 Stroke patients

Stroke is the main cause of acquired disability in adults (van Dokkum et al., 2015) and the second cause of death in the world. The most common disability after stroke is the hemiparesis of the upper limb (Ang et al., 2010). More than 80% of the stroke survivors experience this condition acutely and sub-acutely, and up to 40% are left with chronic diseases (Cramer et al., 1997).

After stroke onset, three phases can be distinguished: i) a first phase called *acute*, lasting from several hours to days after the lesion, ii) a second called *subacute*, lasting up to 5-6 months after stroke, and a final one called iii) *chronic*, potentially lasting for the rest of the patient's life (Cramer, 2008; Kiran, 2012).

After the first hours/days of the *acute* phase, where inflammation/scarring processes occur, neural plasticity in the lesioned area naturally increases, to promote the reorganization of the neural connections and, therefore, the re-learning and functional recovery (Carmichael, 2003). Neurological recovery after stroke follows a nonlinear trend (Kwakkel et al., 2004), where the greatest part of recovery takes place in the first three months after stroke (Wade et al., 1983) and, although displaying considerable variability (Cramer, 2008), on average up to 6 months. Spontaneous neurological recovery can happen in the first months and most likely in the first weeks (Kwakkel et al., 2006), while it reaches a plateau in the chronic phase. Although the outcomes may be masked by spontaneous recovery (Kwakkel et al., 2006), rehabilitation usually is maximally effective in the first months after lesion, thanks to the high level of neural plasticity. For these reasons, among the goals of neurorehabilitation, there are the i) enhancement of amount and duration of natural plasticity, together with its ii) prolongation in the chronic, late phase of the disease (Kleim, 2011).

1.5.2 Upper limb rehabilitation

According to the systematic review in (Hattem et al., 2016), investigating the efficacy of treatments for the motor rehabilitation of the upper limb after stroke, interventions

can be divided in: i) main rehabilitation strategies, and ii) adjuvant therapies. While physical therapies (like the constraint-induced movement therapy, or muscle strengthening) are used as main rehabilitation strategies, the review (Hattem et al., 2016) illustrates a number of adjuvant therapies which were proved to be effective, and may considerably enhance the rehabilitation outcomes. Among these, we find i) mental practice in the form of motor imagery and ii) transcranial direct current stimulation, whose use is suggested in the treatment of both the subacute and chronic phases (Hattem et al., 2016).

1.5.3 Mental practice in the form of motor imagery, and the role of BCIs

Mental practice in the form of motor imagery (MI) has been recently suggested as a valiant add-on tool to boost post-stroke motor rehabilitation (Pichiorri et al., 2015). As already introduced in section 1.4.4, MI involves similar brain regions and functions with respect to the real movement (Jeannerod, 1995). As such, MI is able to recruit the motor system, with the advantage of being independent from the residual level of motor control. With MI training, the reiterated engagement of the motor network would be able to enhance neuroplasticity, with the final outcome of improving the efficacy of rehabilitation (van Dokkum et al., 2015).

One limitation of MI is its being a purely mental task, which makes it difficult for both the therapist and the patient to quantify the performance. In order to provide guidance to the MI exercise, the use of brain-computer interfaces (BCI) has been proposed (van Dokkum et al., 2015). The randomized control trial (RCT) in (Pichiorri et al., 2015), contrasting the conditions of i) MI training alone and ii) BCI-guided MI training, indicated significant increases in neurophysiological and functional outcomes when the mental practice was guided by a BCI.

The neural signature of motor imagery is the desynchronization (ERD) of SMR rhythms on the hemisphere contralateral to the movement (G. Pfurtscheller et al., 2000; Guger et al., 2000; Pfurtscheller and Neuper, 1997). BCIs for guiding MI training give feedback on the strength of ERD (Pichiorri et al., 2015), e.g. by showing a cursor on the screen.

1.5.4 Transcranial direct current stimulation (tDCS)

Transcranial direct current stimulation (tDCS) is a non-invasive brain-stimulation technique, which consists in delivering a low-intensity direct current (usually 1-2mA through 35cm² electrodes), through a pair of electrodes on which one at least one is placed on the scalp (Hummel and Cohen, 2006). Depending on the positioning of the active and reference electrode, tDCS may be anodal (with the anode as active electrode) or cathodal (with the cathode as active electrode). Even though partially non-linear effects were found for high stimulation intensities and durations

(Batsikadze et al., 2013), it is well established that tDCS modulates the excitability of the cortex in a polarity-dependent way, with the anodal stimulation increasing and the cathodal stimulation decreasing cortical excitability (Nitsche and Paulus, 2000). These changes are thought to be due to both modifications in membrane polarization (Nitsche and Paulus, 2000) and synaptic mechanisms (Nitsche et al., 2003). By increasing the excitability of the cortex, the plasticity is also enhanced (Lüdemann-Podubecká et al., 2014).

1.5.5 Combining tDCS and BCI-guided MI training

Several studies proved the possibility to modulate the MI-induced ERDs by means of tDCS (Ang et al., 2015; Baxter et al., 2014; Kasashima et al., 2012; Kasashima-Shindo et al., 2015; Lapenta et al., 2013; Matsumoto et al., 2010; Roy et al., 2014; Soekadar and Birbaumer, 2014; Wei et al., 2013a). Most of them agree that anodal stimulation increases the strength of ERDs, while cathodal tDCS decreases it. As such, anodal tDCS was proposed as a conditioning tool for BCI-guided MI training, as ERDs may look different or weaker in stroke patients, and so more hardly detectable (Ang et al., 2015). A limitation of this approach is that the area targeted for stimulation is the same from which the ERD is recorded to provide BCI feedback, since tDCS is known to induce artifacts on the EEG locations most proximal to the stimulation electrode (Mancini et al., 2015; Soekadar and Birbaumer, 2014). This limits the applicability of tDCS *during* recordings, indeed what it is usually performed is a preliminary tDCS followed by, as soon as possible, MI training (Kasashima et al., 2012; Kasashima-Shindo et al., 2015; Matsumoto et al., 2010; Tohyama et al., 2011; Wei et al., 2013a). However, timing of stimulation is important for motor skill learning (Stagg et al., 2011), and tDCS after-effects are sustained for a limited amount of time (Nitsche and Paulus, 2001).

With the goals to simplify the application of tDCS to BCI training, by increasing its practicality, and to investigate the interhemispheric tDCS effect, we explored in **chapter 2** the feasibility of a novel approach, applying tDCS to the contralateral (instead of the ipsilateral) hemisphere. As this was the first time the envisioned protocol was tested, we checked its feasibility on healthy people.

1.6. Brain computer interfaces for control

In this section, the line of arguments relating the last three chapters of my thesis will be introduced. The focus of these chapters are Brain-Computer Interfaces for control purposes. While **chapter 5** is a separate case-study based on SSVEPs, **chapter 3** and **chapter 4** are ideally in prosecution, and in line with the progressive effort to make BCI control more intuitive and natural, first through the implementation of the co-adaptive approach (**chapter 3**) and, very recently, envisioning a novel control

framework based on movement trajectory decoding (**chapter 4**) (Müller-Putz et al., 2016).

In the following lines, I will briefly introduce the line of arguments relating the works in **chapter 3** and **chapter 4**. A brief introduction of the case-of-study in **chapter 5** will be finally given.

1.6.1 Towards a more intuitive and natural control of noninvasive BCIs

The classic SMR-based BCI paradigms

As introduced in section 1.4.4, motor imagery-based BCIs were the most explored in 1990s and 2000s, indeed all the main research centers in the field, like Wadsworth (Wolpaw et al., 2000), Berlin (B. Blankertz et al., 2008), and Graz (G. Pfurtscheller et al., 2003), proposed in these years their paradigms based on such approach. The basic principle of these systems is that different motor imageries lead to different EEG patterns (Pfurtscheller and Neuper, 1997), which can be classified against each other and used for communication (Scherer et al., 2004) or control (Pfurtscheller et al., 2003) purposes.

The first classical BCI schemes consisted of three separate parts: i) a calibration part without feedback, ii) setting up of the classifier, and iii) online operation, with feedback. In order to be able to calibrate the system, the users were requested to perform the MI task several times without feedback, even for quite long (40-80 trials, (Pfurtscheller and Neuper, 2001)). After setting up the classifier, the online operation phase could start, and the feedback could be given to the users according to the classification of their mental state (G. Pfurtscheller et al., 2003). On one hand, feedback is essential to permit the user to see the consequence of his/her SMR modulations, and so the learning process to begin. On the other hand, feedback learning induces a modification in the user's behaviour, leading to a change in the EEG patterns (Schlögl et al., 2010) and therefore to a decrease of the classifier's performances, still trained on the calibration conditions. To regain accuracy, a novel adaptation of the system could be required, but with the effect of changing again the feedback (Schlögl et al., 2010). The possible difficulties of the interdependency between man and machine were discussed and named as "man-machine dilemma" (Pfurtscheller and Neuper, 2001). To produce learning for the user and improvement of the performances, the BCI first schemes could require several iterations of the entire loop. As a result, learning voluntary control of SMR rhythms with a satisfactory level of accuracy usually was a skilful and non-intuitive task, which could require weeks or even months of user training (G. Pfurtscheller et al., 2003; Tan and Nijholt, 2010).

The co-adaptive approach

One first step towards the simplification of BCI control came with the introduction of the so-called “co-adaptive” approach (Müller-Putz et al., 2016). Having recognized the essential role of feedback in the learning process, one of the goals of the new approach was to minimize the calibration time, in order to start giving feedback as soon as possible during training (Faller et al., 2012). The goal was pursued by either using pre-trained classifiers based on a pool of subjects’ data (Vidaurre et al., 2005, 2006, 2007, 2011a), or priming the subject-specific classifier with a very small amount of data (Faller et al., 2012, 2013, 2014; Kobler and Scherer, 2016; Schwarz et al., 2015). A second implication of the co-adaptive approach is the necessary adaptation of the preprocessing and classifier parameters, both to improve the quality of feedback and to handle the EEG non-stationarities, naturally arising from feedback training (Schlögl et al., 2010). For their promoting the simultaneous adaptation of the user and the machine, this new class of approaches was named “co-adaptive”.

In contrast to the long training process with classical BCI paradigms, when tested on healthy (Faller et al., 2012; Vidaurre et al., 2005, 2006, 2007) or physically impaired (Faller et al., 2013, 2014) users, co-adaptive systems showed online accuracies increasing in just two-three days of training. Also, the BCI paradigms were more engaging, according to the perception of participants (Faller et al., 2012; Müller-Putz et al., 2016; Schwarz et al., 2015).

A co-adaptive BCI is also the subject of **chapter 3** of this thesis. The system in this chapter is based on common spatial pattern (CSP) (Koles et al., 1990; Wang et al., 2005), and uses a linear support vector machine (SVM) for classification. Besides integrating the previously explored concepts of “short calibration” and “recurrent adaptation”, the work suggests some novel points of design which may further increase user training. With the goal of addressing the high variability in BCI performance and mental strategy, which usually occur across users (Dickhaus et al., 2009), the work suggests that a tailoring of the BCI implementation and paradigm may further promote a better synergy between user and machine, making user training even more effective and engaging. Three novel elements of design are introduced in the system, their effect is evaluated over 10 healthy participants, and the results are finally discussed in view of subsequent BCI designs. The content of **chapter 3** is based on the published work in (Mondini et al., 2016).

A novel control framework based on trajectory decoding

As already suggested in (Müller-Putz et al., 2016), although the co-adaptive approach could significantly improve user training, SMR-based control was still rather unnatural, given the discrepancy between the classified motor imaginations and the behaviour of the machine. In order to perceive naturalness of control, the BCI behaviour

should ideally be as close as possible to the users' intended movement (Ofner and Müller-Putz, 2015). A possible way to achieve this, would be to decode the (real or imagined) movement trajectories from the neural recordings, and use these as inputs for the neuroprosthesis to be controlled (Ofner and Müller-Putz, 2015).

Neural tuning to movement direction has first been shown in monkeys through invasive intracortical recordings. The studies discovered that several primary motor and parietal assemblies would mostly fire in relation to preferred movement directions (Caminiti et al., 1990; Georgopoulos et al., 1982; Kalaska et al., 1983). Following primate and human studies showed the possibility to invasively extract hand trajectories and velocity profiles (Black et al., 2003; Carmena et al., 2003; Hochberg et al., 2012; Lebedev et al., 2005; Li et al., 2009; Mulliken et al., 2008) and, in some cases, use these as control input for the movement of an end effector (Carmena et al., 2003; Hochberg et al., 2012; Lebedev et al., 2005; Mulliken et al., 2008). An effort towards decreasing the invasivity of the recordings was made in the first ECoG studies in (Pistohl et al., 2008; Schalk et al., 2007), although the possibility to decode from outside the scalp has been proved just recently, first in MEG (Bradberry et al., 2009; Georgopoulos et al., 2005; Waldert et al., 2008; Yeom et al., 2013) and lately in EEG (Bradberry et al., 2010; Kobler et al., 2018; Lv et al., 2010; Ofner and Müller-Putz, 2012; Úbeda et al., 2015). How the decoded trajectories might be used as a control signal for the BCI in motor impaired users was finally clarified in (Ofner and Müller-Putz, 2015), showing that not only performed movements but also imagined ones could be decoded from low-frequency EEG.

When coming to EEG, research agrees that kinematic information is present in the low frequency band (<3Hz) (Waldert et al., 2009), and that it can be retrieved by means of linear decoders (Robinson and Vinod, 2016). Several studies could decode the hand trajectory velocities (Bradberry et al., 2010) and/or positions (Ofner and Müller-Putz, 2012; Úbeda et al., 2015) from the linearly combined low-pass filtered EEG. While the first designs often included center-out tasks, leading to confusion in understanding which was the best encoded kinematic variable (e.g. positions or velocities), a recent work in (Kobler et al., 2018) finally clarified the spatiotemporal tuning of the EEG to each movement parameter.

Despite the considerable advancements of previous studies in understanding kinematic encoding, when coming to noninvasive EEG, movement decoding had only been performed offline. Building on the findings of the previous works, **chapter 4** presents the first attempt to go online, by implementing real-time control of an assistive robotic arm by means of continuously EEG-decoded two-dimensional movements.

As it is the first time EEG decoding is performed online, **chapter 4** details the methods used for the purpose, with particular attention to the differences and constraints arising when shifting from offline to online decoding, and closing the loop through a

robotic arm. The correlations between decoder output and real movement were evaluated, and the analysis of the contributing EEG sources was completed. The study in **chapter 4** was carried out at the Institute of Neural Engineering (Graz Technical University, Austria), where I had the opportunity to spend an internship, and in strict collaboration with Dipl.-Ing Reinmar Kobler, Ing. Dr. Andreea-Ioana Sburlea, and Prof. Dr. Gernot R. Müller-Putz.

1.6.2 Case of study: improving the efficacy of CCA for SSVEP recognition

As a separate case of study with respect to **chapter 3** and **chapter 4**, but still within the context of Brain-Computer Interfaces for control, **chapter 5** presents two simple but effective ways to significantly improve SSVEP recognition based on Canonical Correlation Analysis (CCA).

CCA is an increasingly used approach in the field of SSVEP recognition. The efficacy of the method has been widely proved, so several variations have been proposed (Chen et al., 2015; Islam et al., 2016; Nakanishi et al., 2014; Pan et al., 2011; Wang et al., 2014; Yuan et al., 2015; Zhang et al., 2011, 2013, 2015, 2014). However, most CCA variations tend to complicate the method, either proposing a subject-specific tailoring, which requires additional user training, or by increasing computational load, e.g. by multiplying the number of steps to assess each SSVEP. However, even taking simple procedures and keeping low computational costs may be relevant, especially to favor the spread of low-cost and high-portability devices. In the study of **chapter 5**, we propose two simple variations to the classical CCA method, and evaluate their impact over ten volunteers in a four-class SSVEP setup. Both variations were able to significantly improve the classification accuracy, leading to increments of 7-8% on average, and 25-30% peak. The reasons underlying these increments are also discussed. Given their modular structure and their no or minimal impact on computational load, we suggest the proposed variations may be easily included in future CCA designs even different from ours. The content of **chapter 5** is based on the published work in (Mondini et al., 2018b).

Chapter 2. Contralateral tDCS during BCI-guided motor imagery training

2.1 Introduction

Over the years, transcranial direct current stimulation (tDCS) and mental practice in the form of motor imagery (MI) have attracted considerable interest with regard to neurorehabilitation, for example in stroke patients (Hattem et al., 2016). Both techniques can indeed promote neuroplasticity, thus boosting recovery when paired with a standard rehabilitation protocol (Hattem et al., 2016).

tDCS is a noninvasive brain stimulation technique that consists in delivering a low-intensity direct current (usually 1-2mA in 35cm² electrodes) for a limited amount of time (10-20 minutes), through a pair of electrodes, of which at least one is placed on the scalp (Hummel and Cohen, 2006). It is well established that tDCS induces polarity-dependent excitability modulations, with anodal stimulation increasing and cathodal stimulation decreasing cortical excitability (Nitsche and Paulus, 2000). The modulation of cortical excitability influences neuroplasticity, which can eventually enhance motor recovery (Hattem et al., 2016; Lüdemann-Podubecká et al., 2014; Schlaug et al., 2008).

As regards motor imagery (MI), its use in neurorehabilitation was proposed given the technique's ability to recruit approximately the same areas as overt movement, regardless of the residual level of motor control (van Dokkum et al., 2015; Hattem et al., 2016; Pichiorri et al., 2015). The reiterated engagement of the motor system induced by MI training is designed to promote the neuroplasticity of the area, thus enhancing recovery (van Dokkum et al., 2015; Hattem et al., 2016; Pichiorri et al., 2015). However, as motor imagery is a purely mental task, it has recently been shown that a better rehabilitation outcome can be achieved when the practice is guided by a dedicated Brain-Computer Interface (BCI) (Pichiorri et al., 2015), and a neurofeedback system in particular, as this closes the loop by providing appropriate feedback to the user.

Generally speaking, a BCI is a system that records neural activity and translates it into a control signal for a particular device (e.g. robotic arm, machine, computer) (Wolpaw et al., 2002). In addition to being used for communication or control purposes

(Birbaumer and Cohen, 2007), BCIs have recently emerged in the context of neurorehabilitation (Daly and Wolpaw, 2008; van Dokkum et al., 2015; Soekadar et al., 2015), where they are employed to decode the neurophysiological features associated with motor imagery or attempted movements, and give feedback accordingly (neurofeedback). At a cortical level, the neural signature of motor imagery is the event-related desynchronization (ERD) of sensorimotor rhythms (SMR) in the motor area contralateral to the movement (Guger et al., 2000; Pfurtscheller and Neuper, 1997). By detecting the ERD and providing contingent feedback to the user, the BCI objectifies the motor network engagement and encourages the desired modulation of cortical rhythms, thus guiding the practice while keeping the user engaged and motivated (van Dokkum et al., 2015; Pichiorri et al., 2015).

Even though tDCS and neurofeedback-guided MI training are usually employed independently of each other, a combination of the two has been recently suggested (Ang et al., 2015; Kasashima et al., 2012; Kasashima-Shindo et al., 2015; Soekadar et al., 2014a; Wei et al., 2013b). The purpose of the combination would be to produce an ERD enhancement by means of tDCS, to facilitate BCI control (Ang et al., 2015; Kasashima et al., 2012; Kasashima-Shindo et al., 2015; Soekadar et al., 2014a; Wei et al., 2013b).

Several recent studies have shown that tDCS can modulate the motor imagery-induced ERD (Ang et al., 2015; Baxter et al., 2016; Kasashima et al., 2012; Kasashima-Shindo et al., 2015; Lapenta et al., 2013; Matsumoto et al., 2010; Roy et al., 2014; Soekadar et al., 2014b; Wei et al., 2013b). Most of them agree that anodal stimulation increases the strength of the ERD in the stimulated area (Ang et al., 2015; Kasashima et al., 2012; Kasashima-Shindo et al., 2015; Matsumoto et al., 2010; Soekadar et al., 2014b; Wei et al., 2013b), while cathodal stimulation decreases it (Matsumoto et al., 2010; Soekadar et al., 2014b). It was therefore suggested that anodal tDCS could be used as a conditioning tool to enhance neurofeedback-guided MI training (Ang et al., 2015; Kasashima et al., 2012; Kasashima-Shindo et al., 2015; Soekadar et al., 2014b; Wei et al., 2013b).

One limitation of the above-described approach is that the target area for stimulation is the same from which the ERD should be collected for neurofeedback. However, as tDCS may induce artifacts in the EEG locations proximal to the stimulation electrode (Mancini et al., 2015; Soekadar et al., 2014a), it is not possible, at least with a traditional 2-channel tDCS device, to perform neurofeedback training *during* stimulation, unless the stimulation electrode is placed in a non-optimal site, which could decrease the efficacy of tDCS (Soekadar et al., 2014a). The situation is typically solved by performing tDCS stimulation first, followed by neurofeedback training (Kasashima et al., 2012; Kasashima-Shindo et al., 2015; Matsumoto et al., 2010; Tohyama et al., 2011; Wei et al., 2013b). However, provided that the tDCS after-effects

are sustained for a limited amount of time (Nitsche and Paulus, 2001), this necessitates starting neurofeedback as quickly as possible right after stimulation. Furthermore, it has been suggested that the timing of stimulation is important for motor skill learning (Stagg et al., 2011). If it were possible to find an experimental setup to facilitate EEG-tDCS co-registration, e.g. by placing the stimulation electrode far enough from the recording sites, this would simplify the application of tDCS to neurofeedback training in both the research and clinical contexts. The configuration would also allow the characterization of tDCS effects not only after but also during stimulation, as in (Mangia et al., 2014).

As a first aim, we investigated the feasibility of an approach where tDCS is applied during neurofeedback-guided MI training not to the ipsilateral, but to the contralateral motor cortex. This would allow simplifying the experimental setup, as the stimulation electrode would be placed far from the EEG recording sites. Our idea was to test whether it was possible to produce an enhancement of the motor imagery-induced ERD on the target motor cortex by exploiting the phenomenon of interhemispheric inhibition (Ferbert et al., 1992). We hypothesize that tDCS may influence the ERD on the contralateral motor cortex with an opposite sign with respect to the ipsilateral modulation, i.e. that cathodal stimulation would bring about facilitation while anodal stimulation would produce an inhibition of contralateral ERDs. Since this is the first time contralateral tDCS is examined with regard to its rehabilitative potential, we applied our protocol to healthy users.

In addition to testing the feasibility of our approach to enhance neurofeedback-guided MI training, we also aimed at clarifying the remote effects of tDCS on contralateral EEG rhythms. Indeed, there are only a few studies that marginally address this issue, particularly during motor imagery, and their results are not fully consistent or comparable given the different experimental setups (Baxter et al., 2016; Lapenta et al., 2013; Notturmo et al., 2014; Roy et al., 2014; Wei et al., 2013b). In Notturmo et al. (Notturmo et al., 2014), where the local and remote effects of tDCS were evaluated during a finger tapping task, an increase in bilateral ERD in the alpha band was observed after anodal stimulation, while there were no effects caused by cathodal or sham (i.e. unreal) stimulation. In Lapenta et al. (Lapenta et al., 2013), an opposing effect of tDCS between hemispheres emerged over the ERDs induced by motor imagery. Conversely, in Wei et al (Wei et al., 2013b), anodal stimulation of the right motor cortex increased the ERD of both left (ipsilateral) and right (contralateral) hand motor imagery. Finally, Roy et al. (Roy et al., 2014) and Baxter et al. (Baxter et al., 2016) did not find stimulation to have an effect on contralateral ERDs.

In regard to the first aim of this study, i.e. testing the feasibility of contralateral tDCS for neurorehabilitation, we hypothesized a situation of single-hand motor imagery training, guided by a dedicated neurofeedback system. The motor imagery task was

repeated before, during, and after stimulation, so that the contralateral tDCS effects could be characterized over time. In regard to the second, more explorative nature of the study, we completed the ERD analysis with a study of EEG spectral power under “reference” or “motor imagery” conditions. By providing a complete analysis of both ERD and power over time, we believe that this work will contribute to the understanding and characterization of the distant tDCS effects on cortical rhythms.

2.2 Methods

2.2.1 Participants

Twenty healthy volunteers (aged 21 to 32, median 26, nine males) took part in the study. Since both interhemispheric connections and the modulating effects of tDCS are influenced by handedness (Bäumer et al., 2007; Kasuga et al., 2015; Vines et al., 2008), we only enrolled right-handed volunteers, as assessed by the Edinburgh Handedness Inventory (Oldfield, 1971). The study conformed to the Declaration of Helsinki and was approved by the Bioethics Committee of the University of Bologna. All participants provided written consent to participate in the study.

2.2.2 tDCS stimulation

We tested both anodal and cathodal stimulations in a sham-controlled design, so each volunteer participated in two rounds of experiments, alternatively receiving real or sham stimulation. Ten out of twenty subjects received cathodal versus sham stimulation, while the other ten underwent anodal versus sham. All participants were blinded to their stimulation condition. The two rounds of experiments were separated by at least 24 hours, but they were always completed within a week (with a median value of the interval of 2 days). On one hand, the minimum interval of 24h provided a sufficient wash-out period from the stimulation effects according to literature, as physiological after-effects of single-session tDCS with similar or superior stimulation intensities and durations were shown to last no longer than 90 (Nitsche and Paulus, 2001) or 120 minutes (Batsikadze et al., 2013). On the other hand, the choice of completing the sessions within a week was intended to have a comparable feedback-induced learning effect across participants. The order of real and sham stimulations was finally randomized and counterbalanced in each group, to compensate for the learning effect when averaging across subjects.

tDCS was delivered by a battery-driven, constant-current stimulator (neuroConn GmbH, Ehrenbergstr, Ilmenau, Germany) through a pair of round, water-soaked sponge electrodes (16 cm²). We set a current intensity of 0.7mA and a stimulation time

of 15 minutes, with 20s ramp up and 25s ramp down in addition. Under the sham condition, the current was supplied for only 60s (20s ramp up, 15s of stimulation and 25s ramp down), just to mimic the physical tingling sensation at the beginning of stimulation.

The selected stimulation parameters are justified in the following lines. We chose a stimulation time of 15 minutes to make sure that tDCS effects outlasted the end of stimulation for a sufficient time to complete the experiment. Over 11 minutes of stimulation duration, the after-effects should indeed remain for approximately 1 hour (Nitsche and Paulus, 2000). In regard to stimulation intensity, previous research showed that a current of 1 mA in 35cm² can effectively modulate cortical excitability (Nitsche and Paulus, 2000, 2001). Given the smaller area of our electrodes (16cm²) and the fact that we were testing an indirect type of stimulation (i.e. contralateral), we decided to apply a current leading to a slightly higher current density (0.0437mA/cm²), equivalent to 1.5mA in standard 35cm² electrodes.

We designed the experiment so that the dominant hemisphere was stimulated, therefore we placed the active electrode (the anode in anodal and the cathode in cathodal stimulation) over the left motor cortex and the reference over the right supraorbital region, as this montage was shown to be optimal for enhancing motor cortex excitability (Moliadze et al., 2010; Nitsche and Paulus, 2000). The stimulation sites (C3 and Fp2) were determined according to the international 10-20 system, as previous studies have confirmed the correspondence between C3, C4 and the primary motor cortices (Homan et al., 1987; Okamoto et al., 2004).

2.2.3 EEG recording

We recorded the EEG signals using a Brainbox EEG-1166 amplifier, with a 128 Hz sampling frequency and according to the extended international 10-20 layout (Sharbrough et al., 1991). We acquired twelve passive wet electrodes overlying the right motor cortex (Fcz, Fc2, Fc4, Fc6, Cz, C2, C4, C6, Cpz, Cp2, Cp4, Cp6), with an additional ground electrode in Pz. After being recorded with respect to ground (Pz), the electrodes were re-referenced to their common average reference and used for both online neurofeedback operation and offline analyses. An outline of the experimental setup is shown in Figure 2.1.

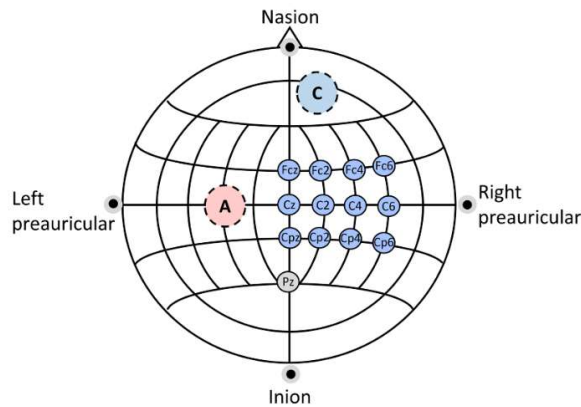


Figure 2.1. EEG recording sites. Location of the twelve EEG recording sites (right hemisphere), the ground electrode (Pz) and the two stimulation electrodes (anodal stimulation in this example).

2.2.4 Experimental paradigm

During the experiments, participants were seated in a comfortable chair in front of the pc screen running the neurofeedback system software. They were asked to keep their gaze fixed, their muscles relaxed and their eyes open.

To evaluate the effects of tDCS on ERD, each participant performed the motor imagery task (left hand motor imagery) before, during and after stimulation. All participants underwent two days of experiments, to compare real and sham stimulation conditions.

The execution of the motor imagery task was timed and guided by the neurofeedback software, which gave feedback in a cue-paced paradigm (see section 2.2.5 for details). The features controlling the feedback were selected for each participant through a short calibration phase, which preceded the first experimental day.

The execution of the neurofeedback software was organized into runs, and the runs into trials. The calibration step consisted of four or five runs, depending on the number of rejected trials (see sub-section of 2.2.5, “*Calibration*”), while the experiment consisted of fifteen runs of neurofeedback online operation: five runs before, five during and five immediately after the tDCS stimulation. The runs were repeated precisely every 3 minutes, so that they were always aligned both with the onset/offset time of stimulation and across subjects (see Figure 2.2 for an outline of the experimental paradigm).

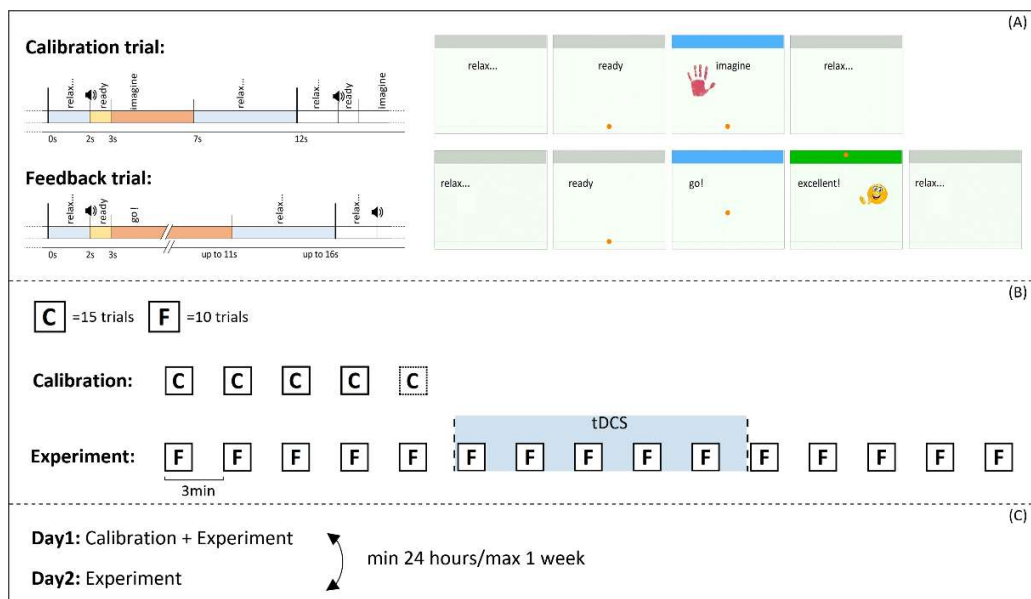


Figure 2.2. The experimental paradigm. Outline of the experimental paradigm at different levels of detail. In (A) the structure of calibration and feedback trials is recalled, while in (B) and (C) we detail the structure of runs and the composition of the experimental days.

2.2.5 The neurofeedback software

We conducted the experiments using custom neurofeedback software, specifically developed for the study. The software, based on LabVIEW (National Instruments) and MATLAB (the MathWorks, Inc), was inspired by the system presented in (Morone et al., 2015; Pichiorri et al., 2015), given its efficacy in guiding MI training in stroke patients (Pichiorri et al., 2015).

The software displayed visual feedback, encoded in a one-dimensional cursor movement, where the speed and direction of the cursor were given proportionally to the instantaneous ERD. Subjects were assigned the goal of reaching the top of the screen in the shortest possible time (i.e. to produce a strong ERD), or at least to keep the cursor on a stable direction towards the top (i.e. to produce a stable desynchronization). In order to encourage the spontaneous desynchronization pattern of the user, the ERD was computed using the pair of subject-specific locations and frequency bands that best showed SMR modulation. The software therefore included two modules: one for calibration (without feedback), and one for online operation (with feedback). The two modules are detailed in the following subsections.

Both calibration and neurofeedback were organized into runs, and the runs into trials. The calibration and neurofeedback runs consisted of fifteen and ten, respectively.

Each trial began with the word “relax” appearing on the screen. After 2 seconds, the word “ready” was displayed, together with a warning tone and the appearance of the cursor at the bottom of the screen. Starting from second 3, the subject was asked to perform the MI task (left hand grasping) for a fixed time of 4s during system calibration (no feedback) and until the cursor reached the top (or with an 8s timeout, after which the cursor disappeared, see the sub-section of 2.2.5, “*Neurofeedback*”) during online operation. The trials ended with 5 more seconds of rest (Figure 2.2).

Calibration

The features controlling cursor motion, the visual feedback, were selected through a short calibration phase. The calibration module included an automated artifact rejection algorithm, implemented as in (Faller et al., 2012). The algorithm marked the trials as outliers if their 25-40Hz power in the active period (0-7s) was higher than three standard deviations from the grand mean of this condition. The algorithm iteratively recomputed both the grand mean and the standard deviation after each outlier rejection, and stopped when no more trials matched the condition to be rejected (Faller et al., 2012).

After each calibration run, the system displayed the total number of rejected trials, therefore it was possible to evaluate if the remaining ones were sufficient for feature selection. As soon as fifty clean trials were collected, the software launched an executable MATLAB file to perform the offline analysis of the data. The aim of this analysis was to find the pair of contiguous channels and frequency bins that showed the spontaneous SMR modulation of the user.

Feature selection was accomplished similarly to (Morone et al., 2015; Pichiorri et al., 2015). After segmenting the trials into overlapping 1s epochs by shifting a 1s-Blackman-Harris-window by 0.125s, we computed the power spectrum by means of a modified periodogram, and extracted from each epoch the power values in the 8-30Hz range with 2Hz bins. We considered 8-30Hz to be a reasonable range for SMR modulation, and the choice was inspired by the work in (Pichiorri et al., 2015), where feedback features covered both the alpha and the beta bands. We labeled as “reference” the epochs in the 0-2s trial period and as “MI” the ones in the 3-7s period. In order to highlight the most discriminating features of the two conditions, the determination coefficient r^2 was computed for every channel and frequency bin, as in (Cincotti et al., 2008; Morone et al., 2015). We compiled the r^2 values both in a channel-frequency matrix and in topographical scalp maps, which made it possible to visually identify the locations and bands with the highest SMR modulation (see Figure 2.3 for an example). The candidate locations were investigated further through time-frequency analyses and ERD time-courses, both averaged across trials. The two

locations and frequency bins that best showed the spontaneous ERD were manually selected after visualization. We always selected a pair of contiguous electrodes and, if different, contiguous frequency bins. The ERDs in the selected channels would be linearly combined to form a single control signal. The weights of the linear combination were also determined manually during calibration. To guarantee better protection against the repositioning of the EEG cap between experimental days, we always tried to choose similar or identical weights for the two locations. If the ERD was significantly more evident in one of the two selected locations, we imbalanced the coefficients up to 0.6 and 0.4 in favor of the channel showing the stronger ERD. The electrodes, bands and weights chosen for each participant are reported in Table 2.S1.

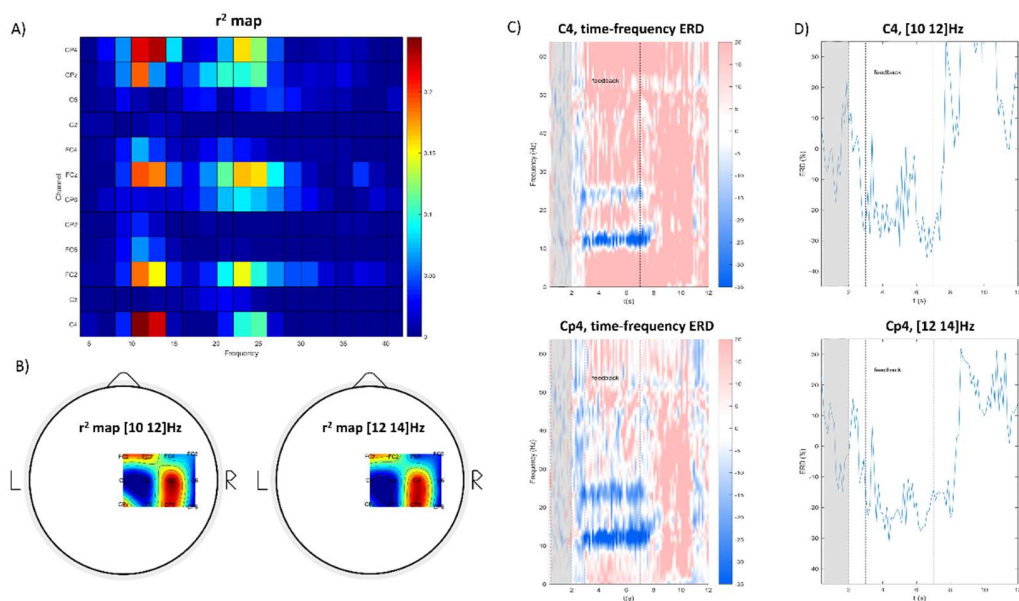


Figure 2.3. An example of the selection of subject-specific channels and frequency bands. In (A) and (B), an example of the matrixial and topographical arrangements of r^2 values computed from calibration trials is shown. In (C) and (D), the candidate channels (C4 and Cp4) and frequency bands (10-12 Hz and 12-14 Hz) are investigated further using time-frequency transforms (C) and ERD time courses (D)).

Neurofeedback (online operation)

During online operation, participants received visual feedback during motor imagery: a cursor appeared on the screen and started moving with speed and direction proportional to the ERDs composing the control signal.

The ERD at a certain frequency was computed as follows:

$$ERD(f, t) = \frac{P(f, t) - Pref(f)}{Pref(f)} \quad (2.1)$$

where $P(f, t)$ is the power in the current time-point and $Pref(f)$ is the average power in the reference period (1.5s-interval before the word “ready”). During online operation,

the power spectrum was extracted from 0.375s-long time windows every 0.125s, through a Yule-Walker autoregressive (AR) algorithm of order $p=16$. At each computation, the ERDs in the selected channels and frequency bins were linearly combined to form the control signal, and the cursor position was updated according to the module and sign of the composite ERD. Whenever a negative ERD value was detected (desynchronization), the cursor moved towards the top, while in the case of a positive value (synchronization) the cursor moved downwards. The distance spanned by the cursor was proportional to the ERD absolute value, with a gain that was trialwise adjusted in order to maintain the challenge for the user.

There was a target at the top of the screen that turned green if it was hit, together with the appearance of the word “good!”. If the hit was achieved in less than 2s, or the direction of the cursor was maintained for more than 2s, the word “good!” was replaced by “excellent!”, and an additional smiley face appeared (Figure 2.2). If the cursor did not reach the top, it simply disappeared after 8s.

2.2.6 Offline analyses

We performed offline analyses with custom scripts using MATLAB (The MathWorks, Inc) and EEGLAB toolbox (Delorme and Makeig, 2004).

We extracted three outcome measures from each subject and trial: i) the ERD values, and the spectral power values in the ii) “reference” or iii) “MI” task condition.

For all analyses, signals were zero-phase band-pass filtered (using a Butterworth filter of order ten) in the 1-40Hz band and re-referenced to their common average reference. We visually checked all trials, inspecting both their time course and their spectrum, and excluded those containing muscular or movement artifacts from further investigations.

To account for the between-subject variability in the alpha peak, we determined the Individual Alpha Frequency (IAF) of each participant (Klimesch, 1999). Similarly to (Pichiorri et al., 2015), we consequently defined four IAF-based frequency bands: theta (from IAF-6Hz to IAF-2Hz), alpha (IAF-2Hz to IAF+2Hz), and two beta bands, β_{low} (IAF+2Hz to IAF+11Hz) and β_{high} (IAF+11Hz to IAF+20Hz).

We extracted the ERD values for each subject and trial by considering the same weights and locations as in the control signal. Power spectral analysis was performed as online, i.e. by means of Yule-Walker autoregressive (AR) algorithm of order $p=16$ on 0.375s-long time windows every 0.125s. For each time-window, the ERDs in the selected channels were evaluated according to Equation 2.1, and then linearly combined. The minimum value of the composite signal was considered as the output

ERD value for the trial. The ERDs were evaluated in the three frequency bands typical for SMR modulation: alpha, β_{low} and β_{high} .

In regard to power spectral analysis, we extracted from each trial the average values of power in the “reference” (0-2s period) or “MI” condition (feedback period of the trial). Differently from ERDs, the analysis was accomplished by means of a modified periodogram, on overlapping 1s epochs by shifting a 1s-Blackman-Harris-window by 0.125s. The power was computed for each channel and frequency band (theta, alpha, β_{low} and β_{high}). In order to compare the data of all subjects, we performed an intra-subject normalization by dividing the power of each band, electrode and trial by the median value of the corresponding power in the pre-stimulation trials (i.e. the median value of the first 5x10 trials, excluding the artifactual ones). The choice of the median instead of the mean was justified by the shape of the power distribution, which was found to be non-normal despite the relatively large sample size.

2.2.7 Statistical analyses

ERD and spectral power

We preliminarily tested for the normality of both spectral power and ERD distributions through a Kolmogorov-Smirnov test (Massey, 1951). Since we did not find normal distributions, we transformed all data before performing ANOVA analyses, by means of Box-Cox transformations (Box and Cox, 1964). The lambda λ parameter of the transformation was estimated separately for the families of ERD and spectral power distributions. After transformation, the data were found to be normally distributed.

We performed a multiway ANOVA analysis for both power values and ERDs, taking single trials into account. We repeated the analyses separately for the cathodal and the anodal group, using the data of all subjects in each group. The multiway ANOVA analysis was aimed at investigating the effects of the (between-subject) factors *time* and *stimulation*. However, to comprehensively describe our data and consider all dependencies among samples, we also included the between-subject factors *frequency band*, *subject* and additionally, in the case of spectral power analysis, the within-subject factor *electrode*. The factor *time* had three levels, depending on the condition of trials with respect to stimulation onset: before (runs 1-5, level *pre*), during (runs 6-10, level *during*) or after (runs 11-15, level *post*) stimulation. The factor *stimulation* had two levels, *stim* for actual or *sham* for sham stimulation, depending on which was administered. The factor *frequency band* had three levels in the case of ERD (alpha, β_{low} and β_{high}) and four levels in the case of spectral power (theta, alpha, β_{low} and β_{high}), depending on the number of bands considered in the analysis. The factor *subject* had ten levels, one for each subject. In the case of spectral power, the factor

electrode finally had twelve levels, one for each recorded electrode. The ANOVA analysis tested the existence of significant effects given by the included factors and, in particular, we were interested in significant effects due to i) *time* ii) *stimulation* or iii) interactions between *time* and *stimulation*.

When appropriate, we conducted post-hoc analyses with Bonferroni correction (Hochberg and Tamhane, 1987). These tests made it possible to compare, for each band, the sham and stimulation condition at each time point (*pre-stim* versus *pre-sham*, *during-stim* versus *during-sham* and *post-stim* versus *post-sham*). We considered a significance level $p=0.025$ for all analyses (i.e. a significance of $p=0.05$ divided by two as the analyses were repeated independently for two groups of subjects, the cathodal and the anodal group).

To allow for a global interpretation of the results on spectral power, we extracted the t-values from post-hoc comparisons between sham and real stimulation conditions and arranged them in topographical scalp maps. We then marked the electrodes corresponding to a $p<0.025$ with a cross (where the p-values were already Bonferroni-corrected for multiple comparisons).

Side-effects questionnaire

Immediately after the experiments, we administered a side-effects questionnaire to each participant to evaluate whether there were differences in their physical perception of tDCS. If no differences between real and sham stimulation are found, this supports the view that tDCS effects over EEG are not due to the physical sensations associated with actual stimulation. The questionnaire asked participants to rate the intensity of the physical perceptions of stimulation on a 1-5 discrete scale. More details on the questionnaire can be found elsewhere (Mangia et al., 2014). Since the data did not fit a normal distribution, we performed each comparison using the Mann-Whitney U test.

2.3 Results

2.3.1 tDCS effect on ERDs

We found a significant *time* effect for both the anodal and the cathodal group, with the ERDs being stronger over time on average (cathodal group: $F=32.99$, $df=2$, $p=5\cdot 10^{-15}$, anodal group: $F=9.24$, $df=2$, $p=9\cdot 10^{-5}$). On the contrary, no main *stimulation* effects were found (cathodal group: $F=0.14$, $df=1$, $p=0.71$, anodal group: $F=2.45$, $df=1$, $p=0.12$), although a significant *time* \times *stimulation* interaction was found for both stimulation groups (cathodal group: $F=4.84$, $df=2$, $p=0.0079$, anodal group: $F=7.43$, $df=2$, $p=6\cdot 10^{-4}$). For the sake of completeness, we also report the main results for the factors *frequency*

band (cathodal group: $F=1665.7$, $df=2$, $p<10^{-15}$, anodal group: $F=745.6$, $df=2$, $p<10^{-15}$) and *subject* (cathodal group: $F=249.6$, $df=9$, $p<10^{-15}$, anodal group: $F=314.5$, $df=9$, $p<10^{-15}$). The results of the (Bonferroni-corrected) post-hoc comparisons between sham and real stimulations at the different time points are detailed in the following lines and summarized in Figure 2.4.

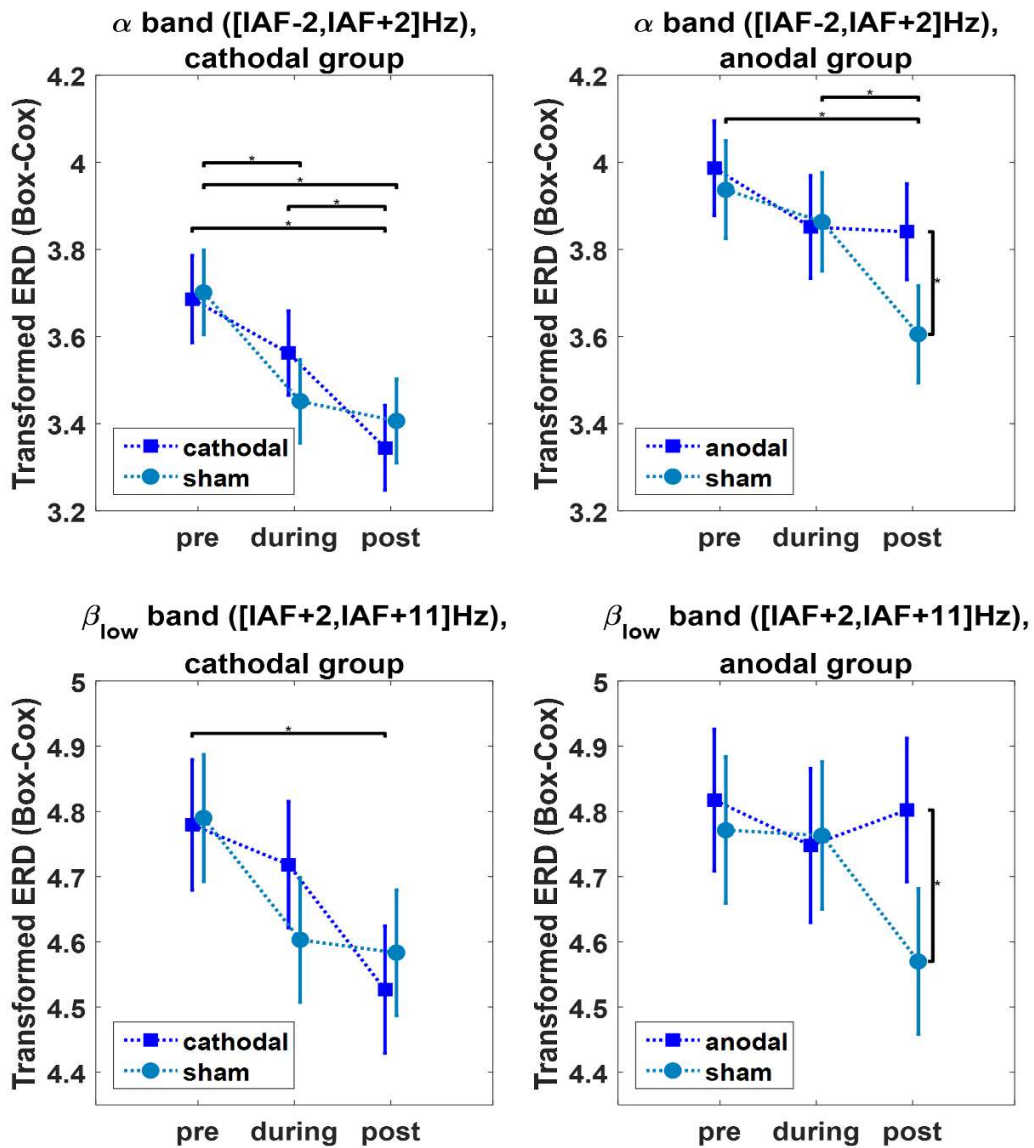


Figure 2.4. The results on ERDs. The figure shows the mean and confidence intervals ($p=0.025$, Bonferroni-corrected for multiple comparisons) of the ERDs in all the stimulation-band combinations where significant effects were found. All time points (before, during and after stimulation) and stimulation conditions (real or sham stimulation) are represented. An asterisk (*) marks the statistically different distributions ($p<0.025$, Bonferroni-corrected), according to post-hoc tests.

In the cathodal group, the magnitude of ERDs tended to increase over time (Figure 2.4), under both the real and sham stimulation conditions and in every frequency band (alpha, β_{low} and β_{high}). Notably, in the alpha band *post-stim*, ERDs were significantly stronger both with respect to the *pre-stim* ($p=8.9\cdot 10^{-7}$) and to the *during-stim* condition ($p=0.024$). In addition, *post-sham* ERDs were significantly stronger with respect both to *pre-sham* ($p=8.9\cdot 10^{-5}$), as well as *during-sham* with respect to *pre-sham* ($p=0.0021$). In the β_{low} band, only the *post-stim* ERDs were significantly stronger than *pre-stim* ERDs ($p=0.0025$), while other post-hoc comparisons were not statistically significant. In the β_{high} band, no significant post-hoc differences were revealed.

In the anodal group, the ERDs showed different behavior between the real and sham stimulation conditions overall: while they progressively tended to increase their magnitude in the sham condition (Figure 2.4), in the real stimulation condition post-stimulation ERDs were not significantly different from pre-stimulation, in each of the tested bands (alpha, β_{low} and β_{high}). Notably in the alpha band, while *post-sham* ERDs were significantly stronger with respect to both *pre-sham* ($p=7.7\cdot 10^{-5}$) and *during-sham* ($p=0.0173$), this behavior was not confirmed in the anodal condition (*post-stim* ERDs statistically identical to *pre-stim*, $p=1$). Furthermore, the comparison of real and sham stimulations at each time point revealed that *post-sham* ERDs were significantly stronger compared to *post-stim* ERDs ($p=0.0147$), while there was no difference between *pre-sham* and *pre-stim* conditions ($p=1$). In the β_{low} band a behavior similar to alpha was found (Figure 2.4), although the only significant post-hoc comparison was between *post-stim* and *post-sham* ERDs ($p=0.0183$). Finally, no significant post-hoc differences were found in the β_{high} band.

2.3.2 tDCS effect on spectral power

In regard to spectral power analysis, the detailed results of the ANOVA tests can be found in Table 2.S2, while the topographical t-value maps from post-hoc comparisons between sham and real stimulations at each time level (pre, during and post-stimulation), for each group (cathodal or anodal) and condition (reference or motor imagery) are reported in Figure 2.5. In regard to beta bands, Figure 2.5 only reports the maps relative to β_{low} , as we found approximately the same behavior for β_{low} and β_{high} .

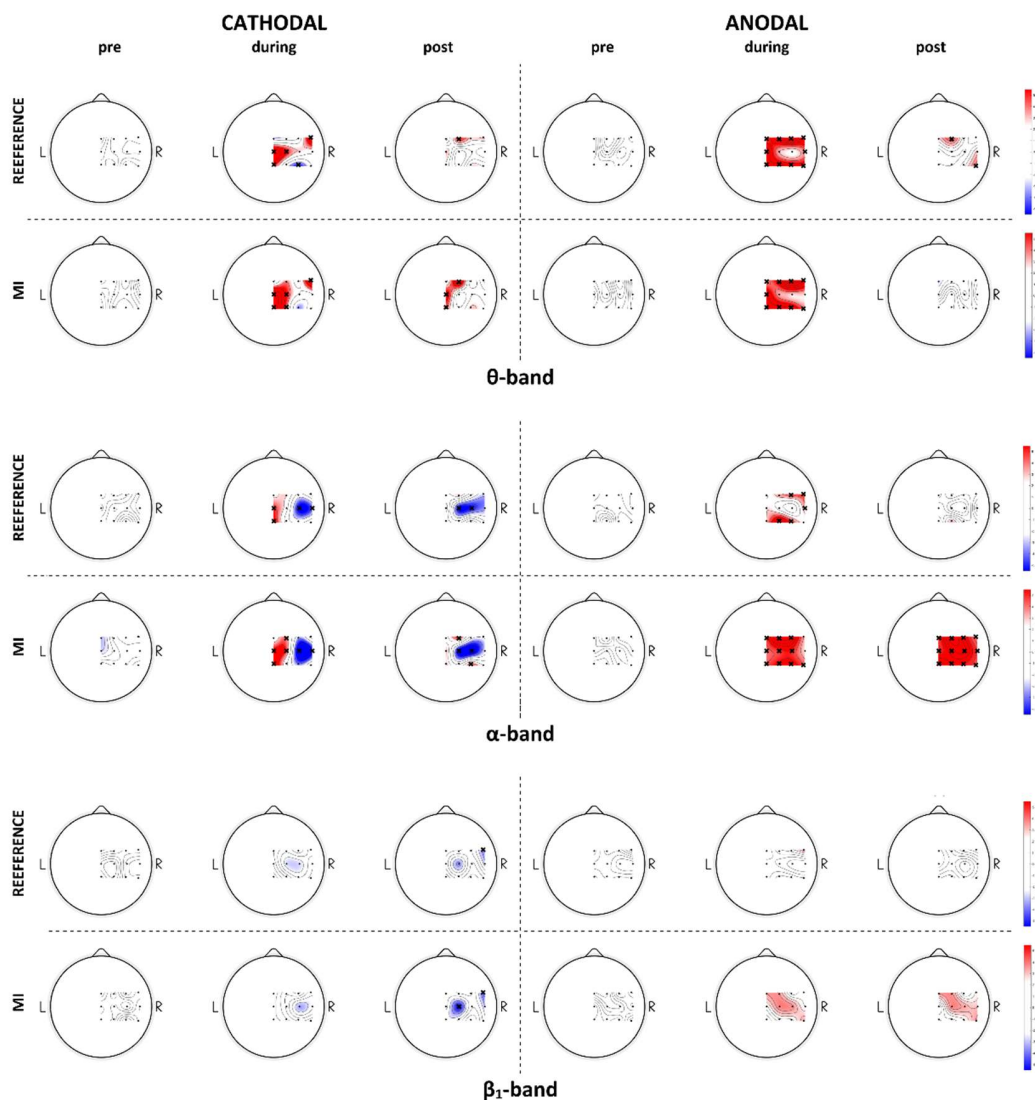


Figure 2.5. The results of spectral power analysis. Spectral power analysis in the θ (upper), α (center) and β low (lower) band: topographical representations of the t-values from post-hoc comparisons between real and sham stimulation conditions, for each time point (before, during and after stimulation) and task condition (reference or motor imagery). A cross marks the electrodes with statistically significant ($p < 0.025$, Bonferroni-corrected for multiple comparisons) difference.

Overall, spectral power analysis highlighted that tDCS stimulation mainly affected theta and alpha bands, both under rest and motor imagery conditions (Figure 2.5).

In regard to the theta band, we found a power increase both in the cathodal and in the anodal conditions with respect to sham stimulation, so there was no polarity-specific effect. However, the power increase was limited to the period concomitant with stimulation, while the differences generally vanished in the *post-stimulation* period (Figure 2.5, upper).

In regard to the alpha band, the analyses revealed both a polarity-specific and, in the anodal group, a task-specific effect. In the cathodal stimulation condition, we found a power decrease with respect to sham in the area around C4, during both rest and motor imagery. In addition, during stimulation the maps highlighted a circumscribed power increase around the central electrodes. In the anodal group, a task-specific effect was also revealed. While in the reference condition, *during-anodal* and even more *post-anodal* power values were not different from sham, in the motor imagery condition alpha-power significantly increased with respect to sham. Roughly the same behavior appeared in the *during* condition.

In regard to beta bands, we found slighter effects overall compared to theta and alpha. From a qualitative point of view, the behavior of beta power was approximately the same as in alpha, with the only exception being the circumscribed power increase occurring in the central electrodes in the cathodal group.

2.3.3 Side-effects questionnaire

According to the Mann-Whitney U test, we found no differences in the side-effect scores between sham and real stimulations. This supports the view that the tDCS impact on the EEG rhythm is not just a placebo/somatosensory effect due to the physical perception of the stimulation.

2.4 Discussion

The aim of this study was to test whether contralateral tDCS could have interhemispheric effects on the spectral power of the unstimulated hemisphere, and whether such effect could be used to enhance ERD magnitudes in the context of a neurofeedback-guided motor imagery paradigm for neurorehabilitation. Our initial hypothesis was that tDCS could exploit interhemispheric inhibition, i.e. that contralateral cathodal stimulation could result in facilitation of ERD on the unstimulated hemisphere, while contralateral anodal stimulation could result in inhibition.

As discussed more thoroughly in section 2.4.1, the analysis of ERDs did not confirm our hypothesis, at least in the case of cathodal stimulation: our results indeed suggest that, while contralateral ERDs are reduced during anodal stimulation, there is no symmetric facilitation for cathodal stimulation.

Even though ERD results suggest that contralateral tDCS is not applicable in the context of rehabilitation, spectral power analysis (see section 2.4.2) revealed the impact of both stimulation polarities on the cortical rhythms of the unstimulated

hemisphere. The discussion on spectral power results complements and completes the previous discussion on ERD, suggesting that not only anodal but also cathodal tDCS can impact the rhythms of the unstimulated hemisphere, although the effect is not task-specific.

Finally, section 2.4.3 discusses the limitations of the study and the generalizability of the findings to a patient population.

2.4.1 tDCS effect on ERDs

Statistical analyses highlighted significant *time* effects and *time*×*stimulation* interactions in both the anodal and cathodal groups, while no significant *stimulation* effects were found. However, when interpreting ERD results, it should be taken into consideration that the experiments were performed with feedback, so it is reasonable to expect a familiarization effect, both within- and between- sessions. Due to the within-session familiarization, an ERD tendency to increase their magnitude over time could be expected; the between-session effect, on the other hand, might cause the baseline ERD value at the beginning of the second day to be stronger for each subject compared to the first, provided that the participant has undergone an entire neurofeedback training session. In order to smooth the potential bias between baseline ERDs when averaging across subjects, making it possible to highlight the effect of stimulation, we designed the experiment so that the order of real and sham stimulation was counterbalanced within each group. The absence of main *stimulation* effects is encouraging in this sense, as it means that there was not a significant bias between real and sham simulation conditions. Lack of significant differences in every post-hoc comparison of baseline ERDs (*pre-stim* vs *pre-sham*) is further encouraging, and allows us to consider the results of comparisons at other time-levels (*during-stim* vs *during-sham* and *post-stim* vs *post-sham*) more reliable.

Turning now to the significant *time* effect found in both stimulation groups, we suggest it could be easily ascribable to the within-session familiarization, indeed the minimum desynchronization values tended to strengthen over the course of the experiment (Figure 2.4). However, the significant *time*×*stimulation* interaction reveals the possibility of an additional role of stimulation. When observing ERD trends in Figure 2.4, it can be seen that there is one case where the increasing ERD trend is not followed, which is the real stimulation condition in the anodal group, especially in the alpha band. The case referred to is indeed the only one where, while *post-sham* ERDs are significantly stronger than *pre-sham* (so the within-session learning effect is still present in the group in the unreal stimulation condition), *post-stim* ERDs are not different from their baseline condition. We interpret the result by hypothesizing that anodal stimulation might have reduced contralateral ERD and this compensated for

the familiarization effect, which did not manifest itself. The significant difference between the *post* conditions of real and sham stimulations further supports this point of view.

We interpret the results as follows: while in the cathodal group ERD behavior is not influenced by stimulation of the homologous contralateral region (indeed both the *stim* and *sham* ERDs show the same increasing tendency), anodal stimulation inhibits the generation of contralateral ERDs, particularly in the alpha band.

Our results on alpha-ERDs are consistent with the initial hypothesis that modulation over the hemisphere contralateral to stimulation has an opposite sign with respect to direct stimulation. Indeed, as previous studies have shown that anodal tDCS strengthens the motor imagery alpha-ERDs in the stimulated region (Ang et al., 2015; Baxter et al., 2016; Kasashima et al., 2012; Kasashima-Shindo et al., 2015; Matsumoto et al., 2010; Soekadar et al., 2014b; Wei et al., 2013b), we suggest that the same stimulation has an opposing effect when applied over the contralateral side. An opposing effect of tDCS on ERD between hemispheres was also found in (Lapenta et al., 2013), while our results are in partial disagreement with those found in (Baxter et al., 2016; Wei et al., 2013b). However, in both (Baxter et al., 2016; Wei et al., 2013b) the feedback was encoded into a left-right cursor movement, controlled by the difference in power between electrodes in opposite hemispheres during left versus right hand motor imagery, while we gave feedback on ERD in subject-specific electrodes and bands and in a single-hand motor imagery design. Furthermore, in (Baxter et al., 2016) a different stimulation setup was tested (they used HD-tDCS). Overall, although both studies mentioned involve BCI-guided motor imagery with feedback, the differences in the experimental paradigms and setups may explain the discrepancy in the outcomes.

We hypothesize that enhanced activation of the left (dominant) motor cortex by means of anodal stimulation may have inhibited the right motor cortex, thus reducing the generation of ERD. Interhemispheric inhibition between motor cortices is a well-known effect (Ferber et al., 1992), thought to be mediated by transcallosal connections (Di Lazzaro et al., 1999; Ferbert et al., 1992; Meyer et al., 1995). Several studies have shown the possibility of modifying interhemispheric balance through noninvasive stimulation (Gilio et al., 2003; Tazoe et al., 2014; Vines et al., 2006, 2008). Nevertheless, whether or not tDCS is able to directly influence transcallosal connections is still up for debate (Di Lazzaro et al., 2012; Lang et al., 2004; Tazoe et al., 2014). Although our results seem to support this point of view, it cannot be excluded that interhemispheric modulation is mediated by subcortical structures. Indeed, the loops involved in the generation of alpha-ERDs are both cortico-cortical and thalamo-cortical (Suffczynski et al., 2001) and it has recently been shown that tDCS can have effects on subcortical structures too, like the thalamus or the caudate nucleus

(Polanía et al., 2012). Given these premises, it cannot be excluded that at least part of the long-distance effect between hemispheres is subcortical in nature. Finally, since we used a contralateral supraorbital reference, there could be a direct influence of the current flow between electrodes, which could marginally affect the ipsilateral circuits of the unstimulated hemisphere (Polanía et al., 2012).

While we found reduced alpha-ERD generation by anodal stimulation, we did not find a symmetrical facilitating effect of cathodal stimulation. Our results indeed suggest that cathodal stimulation on one hemisphere does not influence the behavior of ERDs in the unstimulated one. However, anodal and cathodal stimulations have not always been found in the literature to have symmetrical effects (Notturmo et al., 2014; Polanía et al., 2012). To give an example, Notturmo et al. showed that, while anodal stimulation increased movement-related alpha-ERDs in the stimulated motor cortex, neither sham nor cathodal stimulations had any effect (Notturmo et al., 2014). We can comment that our results are in line with theirs, although mirrored to the other hemisphere. Overall, this asymmetry in the transmission of the tDCS stimulus may be supported by a model like the one in Ursino et al. (Ursino et al., 2010). Although not specific for interhemispheric communication, the model in (Ursino et al., 2010) supports the hypothesis that it is not guaranteed that the transmission of information between two cortical areas is symmetrical with respect to the type of input (inhibitory or excitatory), due to the non-linear properties of the neuronal cortical circuits. Generally speaking, the development of models to interpret the tDCS-induced modulations on cortical rhythms and their transmission between functionally related areas, e.g. specifically between motor cortices, would be useful to improve our understanding of tDCS and to guide its application. For this purpose, a model like the one in Mangia et al (Mangia et al., 2017), which already integrates interhemispheric connection between motor cortices and simulates the phenomenon of ERD/ERS induced by motor imagery, could be a good starting point to capture and interpret the additional role of tDCS.

To sum up, our results suggest that alpha-ERDs in the target motor cortex can be influenced by contralateral tDCS in a polarity-specific manner. In particular, while cathodal stimulation does not induce a global effect, anodal stimulation seems to reduce contralateral ERD.

2.4.2 tDCS effect on spectral power

The results discussed in the previous section suggest that contralateral tDCS is not applicable in the context of BCI training. However, a second, more general aim of this work was to contribute to the understanding of the impact of tDCS on EEG rhythms between hemispheres. This section, which discusses the results of power spectral analysis, complements and completes the previous discussion on ERDs, by showing

that not only anodal but also cathodal stimulation can affect contralateral EEG rhythms.

In line with previous research involving the stimulation of motor-related areas (Mancini et al., 2016; Notturmo et al., 2014; Pellicciari et al., 2013), we found that tDCS mainly influences the power in theta and alpha bands.

In regard to the theta band, we generally found power increments occurring during stimulation, regardless of stimulation type and task condition. However, since the effects tended to disappear after stimulation (Figure 2.5) and given the localization mainly close to the stimulation sites (C3 and Fp2), we suggest that this is a direct current effect. For the same reasons, we suggest that the alpha-power increase occurs during cathodal stimulation over central electrodes of the same type. This interpretation is in line with previous works (Mancini et al., 2015; Roy et al., 2014; Soekadar et al., 2014a) describing the tDCS artifact as a low-frequency power increase in the electrodes near the stimulation sites. Notably, the higher frequency component of the disturbance may be due to ongoing small voltage shifts of the stimulator to maintain a constant current despite the little changes in electrode-skin impedances (Roy et al., 2014).

In regard to more distant electrodes, the alpha-band spectral power analysis interestingly revealed both a polarity-specific and, in the anodal group, a task-specific effect of stimulation. Overall, we found that cathodal stimulation decreased contralateral alpha power, while anodal stimulation tended to increase it. Moreover, in the anodal group the power increase only appeared during motor imagery, leaving the reference condition unaffected.

The EEG rhythms in the alpha band have historically been considered resting rhythms for the brain (Pfurtscheller et al., 1997; Suffczynski et al., 2001) or, more recently, related to active inhibition and timing of processes (Klimesch et al., 2007). In the sensorimotor cortex, it has been suggested that the alpha rhythm reflects the cortico-thalamic idling rhythm, when no somatosensory input is processed and no motor output is generated (Pfurtscheller et al., 1997). As the alpha rhythm desynchronizes with movement (McFarland et al., 2000), reflecting activation of the area, synchronized alpha activity has also been related to active inhibition (for example, in situations where a response must be avoided, or non-related task areas have to be silenced) (Klimesch et al., 2007). Given these premises, the widespread increase in alpha power seen in the post-anodal phase during motor imagery can be interpreted as a more inhibited state of the right motor cortex. We further hypothesize that this increase only manifests itself when the motor cortex is actively recruited, i.e. only during motor imagery, which explains why the “reference” state is unaltered. This behavior is in line with the findings of Notturmo et al. (Notturmo et al., 2014),

suggesting that only cathodal stimulation influenced the pre-trial resting condition, while it was unaffected by anodal stimulation.

With respect to ERD analysis, spectral power analysis gives some additional insights into the effect of cathodal stimulation also. Indeed, if the ERD outcomes indicate that cathodal stimulation does not affect the contralateral side, the latter analysis suggests that not only anodal, but also cathodal stimulation has long-distance effects, which is in line with previous research (Mancini et al., 2016; Tazoe et al., 2014). Overall, cathodal stimulation was linked to a decrease in alpha power in the right hemisphere, which may be interpreted as enhanced activation. However, although slighter, we found a similar effect in the beta bands. Furthermore, the effects were not task-dependent in this case, i.e. they were not altered by motor cortex recruitment during motor imagery, so the results should be interpreted with caution.

A final interesting result of spectral power analysis concerns the overall continuity of the effects during and after stimulation. If we exclude the spectral power increase observed in the theta band and in the central electrodes of the alpha band in the cathodal group, which we previously ascribed to a direct current effect, we can indeed observe that the activation pattern in the *post* condition is generally the same as in the *during* condition. This result is in line with the work of Mangia et al. in (Mangia et al., 2014), indicating that the tDCS-induced alterations begin in the very first minutes of stimulation.

Altogether, spectral power results corroborate the hypothesis that anodal stimulation of the left motor cortex increases inhibition of the contralateral one. Indeed, the widespread increase in alpha power, reflecting a more inhibited state, only manifests itself when the motor cortex is actively recruited during motor imagery. In regard to the cathodal group, power data analyses add the information that not only anodal, but also cathodal stimulation has a long-distance effect, although it does not appear to influence ERD generation.

2.4.3 Limitations of the study and generalizability to a patient population

One potential limitation of the study design is the presence of feedback, which has introduced a familiarization effect whereby the investigated variable, the ERD, was not stable over time. Also, the reinforcement of each participant in a slightly different band by selection of the subject-specific frequencies with spontaneous SMR modulation could have increased the variability of the data. On the other hand, feedback is important to keep the participant engaged and motivated, and its absence does not guarantee stabilization of ERDs, as boredom and lack of concentration can occur after a while and affect performance. In addition, as the particular aim of this study was to

test the applicability of the setup with respect to its rehabilitative potential, we preferred using the neurofeedback-guided motor imagery training paradigm as a starting point, to evaluate the adjunctive role of stimulation. Even though both the within- and between-subject learning effects were taken into consideration when interpreting and discussing the results, it is possible that a different setup, e.g. with or without different feedback, could have led to slightly different results.

A final point we would like to discuss is the generalizability of our findings to a patient population. In particular, as this was a pilot study on healthy controls, we suggest it is not entirely correct to conclude that the same null-effect would appear in a patient population. First of all, a possible ceiling effect in SMR control could have manifested itself in healthy users. Furthermore, differences in brain physiology, e.g. the interhemispheric imbalance after stroke (Lüdemann-Podubecká et al., 2014), or the plastic reorganization of the brain, could modify the outcomes when translating to patients. For example, interhemispheric imbalance in stroke patients might result in contralateral cathodal tDCS having a beneficial effect on ERDs of the unstimulated hemisphere, as has been seen in motor recovery (Lüdemann-Podubecká et al., 2014), by inducing relief of inhibition exerted by the contralesional side, not evident in healthy subjects. Therefore, although our findings would suggest not following the contralateral cathodal tDCS approach in the context of neurofeedback-guided motor imagery training, it cannot be excluded that a similar experimentation in stroke patients might lead to a slightly different outcome.

2.5 Conclusion

Both spectral power and ERD analyses suggest that anodal tDCS of one motor cortex results in inhibition of the contralateral one. Assuming the effect of anodal tDCS to be excitatory in the stimulated cortex, this outcome would confirm our initial hypotheses that: i) the ERDs on the target motor cortex may be modulated by contralateral anodal stimulation and ii) this modulation has an opposite sign with respect to the stimulated hemisphere (which is in line with the phenomenon of interhemispheric inhibition).

Unfortunately, we did not find a symmetrical ERD enhancing effect through contralateral cathodal stimulation, which suggests that this setup is not applicable in the rehabilitation context (although differences in brain physiology and especially interhemispheric imbalance might lead to a non-null effect in the stroke patient population). Nevertheless, spectral power results suggest that not only anodal, but also cathodal stimulation can induce long-distance effects on the contralateral motor cortex. Altogether, our results support some recent findings, as in (Notturmo et al., 2014), indicating the possibility of tDCS modulation being transmitted between functionally related cortical areas. We further suggest that the development of models

to interpret the tDCS-induced modulations on cortical rhythms would be useful to improve understanding of the neuromodulatory effects of the technique and to guide its application.

2.6 Supplementary Material

Table 2.S1. Electrodes, bands and weights used for each subject for the composition of the control signal. The table shows the electrodes, bands and weights chosen for each subject after calibration for the composition of the control signal. The chosen locations and bands reflect the spontaneous SMR modulation of each participant.

CATHODAL				ANODAL			
Subject	Bands	Electrodes	Weights	Subject	Bands	Electrodes	Weights
S1	[8 10]Hz	Cp2	0.5	S1	[8 10]Hz	Cp2	0.6
	[8 10]Hz	Cp4	0.5		[8 10]Hz	Cp4	0.4
S2	[10 12]Hz	C2	0.5	S2	[10 12]Hz	Cp4	0.5
	[10 12]Hz	C4	0.5		[12 14]Hz	Cp6	0.5
S3	[12 14]Hz	C4	0.5	S3	[10 12]Hz	C4	0.5
	[10 12]Hz	Cp4	0.5		[10 12]Hz	Cp4	0.5
S4	[12 14]Hz	C4	0.5	S4	[10 12]Hz	C4	0.5
	[12 14]Hz	Cp4	0.5		[10 12]Hz	Cp4	0.5
S5	[12 14]Hz	Cp4	0.5	S5	[10 12]Hz	Cpz	0.4
	[14 16]Hz	Cp6	0.5		[10 12]Hz	Cp2	0.6
S6	[14 16]Hz	Fc4	0.5	S6	[14 16]Hz	C2	0.6
	[14 16]Hz	Fc6	0.5		[14 16]Hz	C4	0.4
S7	[16 18]Hz	Cp2	0.5	S7	[10 12]Hz	Cp2	0.4
	[16 18]Hz	Cp4	0.5		[10 12]Hz	Cp4	0.6
S8	[18 20]Hz	C4	0.4	S8	[12 14]Hz	Cp2	0.4
	[18 20]Hz	Cp4	0.6		[12 14]Hz	Cp4	0.6
S9	[20 22]Hz	C4	0.5	S9	[18 20]Hz	C2	0.5
	[20 22]Hz	Cp4	0.5		[18 20]Hz	C4	0.5
S10	[22 24]Hz	Cpz	0.5	S10	[22 24]Hz	C2	0.5
	[22 24]Hz	Cp2	0.5		[22 24]Hz	C4	0.5

Table 2.S2. Results of ANOVA tests for spectral power analysis. The table shows the complete results of the multiway ANOVA tests performed on spectral power in the two groups (cathodal and anodal) and conditions (rest or motor imagery). The factors included in the analysis were *time*, *stimulation*, *frequency band*, *subject* (between-subject factors) and *electrodes* (within-subject factor).

CATHODAL				ANODAL			
condition: "reference"				condition: "reference"			
Factor	F-value	df	p-value	Factor	F-value	df	p-value
<i>Time</i>	49.9	2	$2.7 \cdot 10^{-22}$	<i>Time</i>	8.81	2	$1.5 \cdot 10^{-4}$
<i>Stimulation</i>	0.79	1	0.37	<i>Stimulation</i>	27.3	1	$1.7 \cdot 10^{-7}$
<i>Frequency band</i>	88.1	3	$2.7 \cdot 10^{-56}$	<i>Frequency band</i>	3.74	3	0.011
<i>Subject</i>	117	9	$1.3 \cdot 10^{-109}$	<i>Subject</i>	22.2	9	$1.7 \cdot 10^{-38}$
<i>Electrodes</i>	41.3	11	$2.9 \cdot 10^{-90}$	<i>Electrodes</i>	9.45	11	$2.9 \cdot 10^{-17}$
<i>Time × stimulation</i>	0.34	2	0.72	<i>Time × stimulation</i>	21.7	2	$3.7 \cdot 10^{-10}$
condition: "motor imagery"				condition: "motor imagery"			
Factor	F-value	df	p-value	Factor	F-value	df	p-value
<i>Time</i>	62.6	2	$9.3 \cdot 10^{-28}$	<i>Time</i>	26.6	2	$1.9 \cdot 10^{-13}$
<i>Stimulation</i>	1.98	1	0.16	<i>Stimulation</i>	90.2	1	$1.9 \cdot 10^{-21}$
<i>Frequency band</i>	157	3	$2.2 \cdot 10^{-99}$	<i>Frequency band</i>	30.2	3	$2.0 \cdot 10^{-19}$
<i>Subject</i>	237	9	0	<i>Subject</i>	33.5	9	$1.0 \cdot 10^{-58}$
<i>Electrodes</i>	109	11	$1.4 \cdot 10^{-249}$	<i>Electrodes</i>	64.3	11	$4.1 \cdot 10^{-144}$
<i>Time × stimulation</i>	3.52	2	0.029	<i>Time × stimulation</i>	26.5	2	$7.2 \cdot 10^{-14}$

Chapter 3. A co-adaptive BCI based on motor imagery

3.1 Introduction

A well-established control strategy for EEG-based BCIs is the one based on motor imagery (MI). As the imagination of each movement is associated to specific modulations (called event-related desynchronizations or synchronizations, ERD/ERS) of the EEG sensorimotor rhythms (SMR), different MIs can generate different EEG patterns, which can be classified and used as control inputs for the BCI (B. Blankertz et al., 2008; G. Pfurtscheller et al., 2003; Wolpaw et al., 2000).

One limitation of these systems is that learning stable, voluntary SMR control may be a skilful and non-intuitive task, potentially requiring from weeks to months of user training (Tan and Nijholt, 2010). To tackle this problem, the first so-called “co-adaptive” BCIs have been proposed (Schlögl et al., 2010).

In contrast to classical BCI training, requiring long calibration parts (Pfurtscheller and Neuper, 2001), the newly introduced co-adaptive approach focused on giving feedback as soon as possible, to make the user aware of its SMR modulations, and ultimately boost the training process (Faller et al., 2012). One implication of this approach is the necessary adaptation of the system parameters, needed to handle the EEG non-stationarities, naturally arising from feedback training (Schlögl et al., 2010).

Examples of previous co-adaptive BCIs are the ones in (Faller et al., 2012, 2013, 2014; Qin et al., 2007; Vidaurre and Blankertz, 2010; Vidaurre et al., 2005, 2006, 2007, 2011a, 2011b; Xia et al., 2012). In (Faller et al., 2012, 2013, 2014; Vidaurre et al., 2005, 2006, 2007), adaptive autoregressive (AAR) parameters and logarithmic band power features were used in combination with quadratic or linear discriminant analysis (QDA and LDA) classifiers. The systems were fully automated, gave feedback from the beginning ((Vidaurre et al., 2005, 2006, 2007)) or after a few minutes of calibration ((Faller et al., 2012, 2013, 2014)) and updated the classifier's parameters trialwise. When tested on healthy (Faller et al., 2012; Vidaurre et al., 2005, 2006, 2007) or physically impaired (Faller et al., 2013, 2014) users, the systems showed online accuracies increasing in just two-three days. In (Xia et al., 2012) and (Qin et al., 2007), common spatial patterns (CSP) and support vector machine (SVM) classifier were adopted. In (Vidaurre and Blankertz, 2010; Vidaurre et al., 2011a) more sophisticated patterns were proposed, while the work in (Vidaurre et al., 2011b) finally introduced unsupervised adaptation.

While the concepts of “short calibration” and “adaptivity” have already been explored in previous studies, two additional and potentially relevant aspects to boost BCI training may regard the “flexibility” and “customizability” of design. As BCI performance can greatly vary across users (Dickhaus et al., 2009), tailoring of BCI implementation and paradigm might promote a better synergy between the user and the machine, making BCI training more effective and engaging.

In this work, we present a two-class MI-based co-adaptive BCI, giving online feedback in the form of the movement of a modelled arm. The system is based on common spatial pattern (CSP) for feature extraction and support-vector machine (SVM) for classification. The novel elements of design regard: i) the imbalance in the training conditions, in favour of the one which is the hardest to predict, ii) the presence of adaptive thresholds for feedback, and iii) the presence of a flexible training session, tailored to the characteristics and ability of the user. We online tested our system with 10 healthy participants, recorded for six sessions each over the course of three days. The effect of the novel design elements is evaluated, and finally discussed in view of future BCI designs.

3.2 Methods

3.2.1 Signal acquisition and preprocessing

We acquired the EEG signals through a Brainbox EEG-1166 amplifier and 128 Hz sample frequency. Eleven passive wet Ag/AgCl electrodes were recorded from sensorimotor areas (Figure 3.1), together with a reference electrode on the right ear lobe and ground electrode on the forehead.

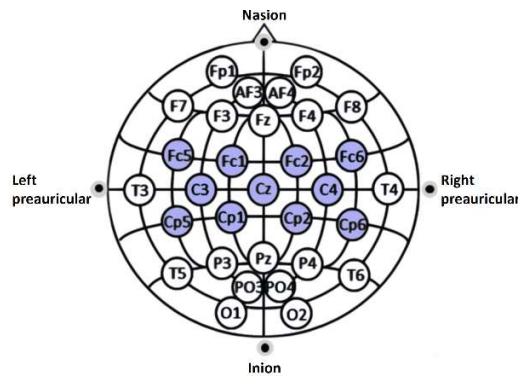


Figure 3.1. The recorded EEG channels.

EEG signals were re-referenced to their common average reference (CAR) (McFarland et al., 1997b). In order to keep the eleven brain signals linearly independent, we included the right ear potential in the averaging operation. After re-referencing, signals were filtered in the 8-30Hz band (Müller-Gerking et al., 1999).

We used common spatial pattern (CSP) for feature extraction (Koles et al., 1990). As it is known, the algorithm finds the matrix \mathbf{W} that maps the EEG multi-channel data in a space with maximal difference in variance between the 2 classes (Wang et al., 2005). Let \mathbf{X} be the $N \times t$ matrix of recorded and pre-processed signals (N channels acquired, t number of samples), the transformed EEG signals in \mathbf{Z} ($N \times t$) will be obtained as $\mathbf{Z} = \mathbf{W} \cdot \mathbf{X}$. To compute the \mathbf{W} matrix, the CSP method considers the simultaneous diagonalization of the averaged normalized covariance matrices of the two classes (right/left hand MI). Further details on the CSP algorithm may be found in (Ramoser et al., 2000).

As suggested in (Müller-Gerking et al., 1999), we composed the feature vector \mathbf{f} with considering the log-transformed normalized variances of the first and two signals in \mathbf{Z} . The feature vectors \mathbf{f} were later used to train a support vector machine (SVM) classifier (Burges, 1998; Cortes and Vapnik, 1995), with a linear kernel and a soft margin equal to 1.

3.2.2 The online BCI system: the three modules

This section will outline the three modules in our system: *Training (T)*, *Training&Updating (U)*, and *Classification (C)*. The three modules had different functions, and were designed to be assembled together to setup the training session. The entire system was developed in LabVIEW.

Training (T)

The goal of the T module was to make a first estimation of the \mathbf{W} matrix and the SVM parameters, without feedback for the user.

MI instructions and feedback: when T started, an upward/downward pointing arrow appeared on the screen over the modelled arm (Figure 3.2, left). Depending on the direction of the arrow (upward or downward), the user is requested to imagine the movement of his right or left hand, respectively. No feedback was given to the user.

Arrow balancing: each T consisted of 14 balanced arrows (7 upwards and 7 downwards), of 10s each, and with 2.5s of rest. The training process without feedback therefore lasted less than 3 minutes. The arrow presentation order was randomized.

First computation of \mathbf{W} and SVM parameters: when the arrow was visible, 2s-long EEG signal portions were extracted every 0.5s. This resulted in 17 portions from every arrow repetition, for a total of 238 (17 portions \times 14 repetitions). The 238 total portions were labelled according to the corresponding arrow's direction and used to i) estimate \mathbf{W} , ii) extract the feature vector \mathbf{f} and iii) train the SVM classifier (Figure 3.3, a). At the end of T module, the software automatically switched to U .

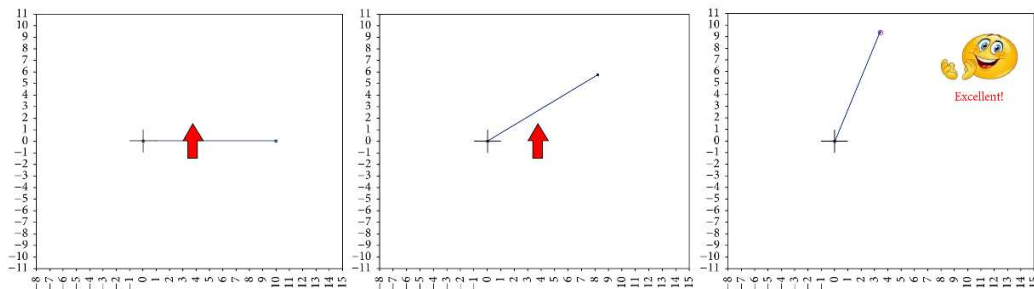


Figure 3.2. Upward pointing arrow in the T module (left) and in the U module (centre). On the right, a target reached in C module is shown.

Training & Updating (U)

U module was designed to be reiterated several times (U repetition). The main purpose of U was to guide user training by providing feedback, while adapting the system's parameters. Both \mathbf{W} matrix and the SVM classifier were adapted at the end of each U , after making a selection over the recorded signals. This module also introduces the concepts of adaptive thresholds and unbalancing in the training conditions.

MI instructions and feedback: similarly to T , MI instructions were given by presenting an upward/downward pointing arrow over the modelled arm, each arrow was visible for 10s with 2.5s rest, and 2s-long EEG signal portions were extracted every 0.5s. Nevertheless, in U module a time-discrete feedback, encoded in a 5°

increase/decrease of the model's shoulder angle, was added according to the classifier's output (Figure 3.2, centre). After filtering each new portion with \mathbf{W} , the feature vector \mathbf{f} was extracted, and the output of the SVM classifier used to give feedback to the user.

Adaptive thresholds: in order to keep challenging the user, we decided to provide feedback only if the analysed EEG signal portions were "distant enough" from the classifier's separation hyperplane. Since the user's ability to produce different MI could be imbalanced, we considered 2 independent thresholds for right and left hand MI. Both started from 0 and were continuously adapted. Their value was the 60% of the average of the right/left hand imagery feature's distances obtained from the beginning of the session. For threshold computation, only the 'correct' features (i.e. when the classifier's output agreed with the arrow direction) were taken into account. The choice of 60% was based on preliminary experiment, as a trade-off between challenging the users and frustrating them.

Updating and utilization of \mathbf{W} and SVM parameters: in each U repetition, the arrow was shown in all 10 times, and each time it was visible for 10s. At the end of each U , a total of 170 new signal portions (17 signal portions from each arrow x 10 arrow repetitions) was therefore available to update \mathbf{W} and the classifier. Out of the 170 portions, we decided to keep in the memory only the ones correctly classified and above the threshold. The resulting list was called the "best portions list" (B list). The B list was further reduced, by equalizing the number of right hand and left hand features. In the balancing operation, the B elements with the shortest distance from the hyperplane were removed first. After this operation, a list of best balanced portions (BB list) was obtained.

The BB list was first used to update \mathbf{W} (\mathbf{W}_{new}) by extracting the covariance matrices from the BB signals. Specifically, \mathbf{W}_{new} was computed by averaging the new BB covariance matrices together with all the matrices selected from the beginning of the session (i.e. those from T module and all those obtained from BB lists in each U repetition completed up to that moment). In this way, we aimed to gradually stabilize the \mathbf{W} matrix, as it resulted from the averaging of an increasing number of covariance matrices.

Once \mathbf{W}_{new} was computed, the BB list was also used to update the classifier's training set. First of all, the old training set had to be remapped according to \mathbf{W}_{new} . Once the training set had been remapped, the BBs were also transformed with \mathbf{W}_{new} , and the new features used to *replace* the older ones in the training set. We opted for *replacement* instead of simply *adding* the new features to the training to avoid an increment of computational weight. Once the training set had been updated, the new SVM classifier (SVM_{new}) could be re-trained.

To further clarify the updating procedure, we review here the steps at the end of each U repetition, and summarize them in Figure 3.3:

1. At the end of U , only the B were kept in the memory. The list was further reduced balancing the samples of the 2 classes (right hand and left hand imagery), thus obtaining the BB list.
2. New normalized covariance matrices were extracted from the BB signals. For each class, the new matrices were averaged along with the previous ones. W_{new} was therefore computed.
3. The old classifier's training set was remapped with W_{new} .
4. New features were extracted from BB according to W_{new} . These new features were used to replace the older ones in the classifier's training set. SVM_{new} could be set up.
5. Repeat U or switch to C module.

Arrow imbalancing: one last characteristic of U module was the imbalance in the presentation of the arrows. In particular, to maximize the probability of updating the classifier (given the balancing operation from B to BB) and to customize the user's training with a stronger stimulation of the most critical MI condition, the pointing arrow corresponding to the most misclassified task was presented more frequently. To clarify, at the end of each U repetition, the number of misclassifications for each class was counted, and the ratio between the two was computed. Depending on the ratio, the arrow directions in the following U repetition could be imbalanced up to 7:3 (or 3:7), in favour of the previously most misclassified class. As the user improved his/her skills in both MI conditions, the ratio between the arrow directions would tend to return to a balanced 5:5.

Accuracy: at the end of each U repetition, the classification accuracy of the current step was evaluated as the ratio between the correctly classified features and the total number of processed features. Because of the imbalance in favour of the most misclassified class, the obtained classification accuracy obtained was underestimated. As soon as the classification accuracies were stable and good enough (see Paragraph 2.3.2), the system automatically switches to C module.

Table 3.1. Overview of the characteristics of the three modules.

T	U	C
<ul style="list-style-type: none"> ▪ one T repetition ▪ MI instruction via arrow presentation ▪ no feedback ▪ first estimation of W and SVM Classifier ▪ balanced arrows 	<ul style="list-style-type: none"> ▪ several <i>U</i> repetitions ▪ MI instruction via arrow presentation ▪ feedback (above-threshold) ▪ adaptively updated thresholds ▪ use of W a SVM and its updating ▪ imbalanced arrows ▪ accuracy evaluation 	<ul style="list-style-type: none"> ▪ several C repetitions ▪ MI instruction via target position ▪ feedback (above-threshold) ▪ thresholds no longer updated ▪ use of W and SVM ▪ accuracy evaluation

Classification (C)

C module was designed to test the user’s ability to control the movement of the modelled arm to reach targets on the screen. In *C* module the adaptive thresholds, **W** and the SVM classifier were no longer updated.

MI instructions and feedback: in *C* module, the MI instruction was no longer given by presentation of the pointing arrow, but through the appearance of a ball-shaped target (Figure 3.2, right). The user had to reach the target with the arm’s end-point as soon as possible, with a timeout of 120s. As for *T* and *U*, 2s-long EEG signal portions were extracted and classified every 0.5s. Every *C* repetition consisted of 5 targets presented in succession on the screen, with a 5s pause when the target is reached. As the user reached the target, a smiling face appeared on the screen (Figure 3.2, right). A sad face was shown if the timeout expired.

Adaptive thresholds: similarly to the *U*, feedback was given only in case the extracted features were above-threshold. Thresholds in *C* module were no longer updated, using the ones computed in the last *U* repetition.

Utilisation of **W and SVM parameters:** **W** and the SVM classifier were no longer updated, using the ones computed in the last *U* repetition.

Accuracy: at the end of *C*, classification accuracy could be estimated as the ratio between the correctly classified features and the total number of processed. Since participants were asked to reach the target as quickly as possible, the “correct” label could be derived from the target’s position. Classification accuracy was computed considering i) the targets reached; ii) the first 30s of “timeout” cases. The assumption

was made as, after a while, participants tended to give up trying to reach the target and simply waited for the timeout, thereby invalidating the deduction of the “correct” label.

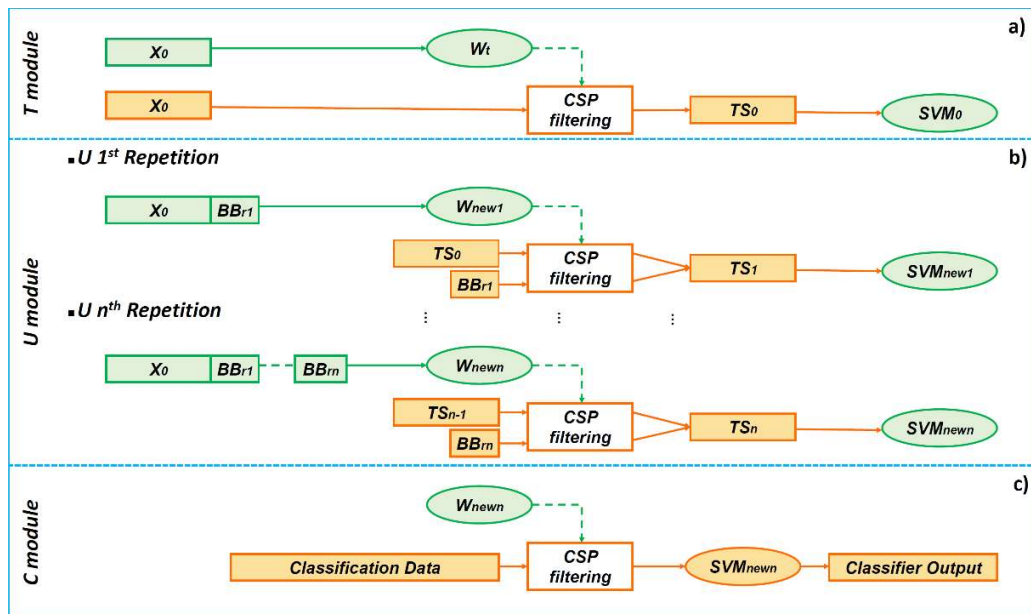


Figure 3.3. A conceptual schema describing the evaluation/use of W matrix and SVM classifier in the three modules. a) The first set-up of W and SVM, starting from the time-domain EEG signal (X_0), in T module. b) A diagram describes how W and SVM are updated in U module, starting from the stored signal portions, the current BB list and the previous training set. c) The schema shows how the definitive W and SVM are used in C module to classify the incoming signals and provide the feedback.

3.2.3 Experimental setup and participants

The system was online tested on 10 healthy volunteers (seven females), eight of them with no previous MI experience. Participants were right-handed (according to Edinburgh inventory (Oldfield, 1971)), and aged 26.5 ± 2 years (mean \pm standard deviation). The experiment conformed the Declaration of Helsinki, and was approved by the local bioethics committee.

During the experiment, the participants sat in front of the PC screen, with their arms relaxed and in a comfortable position. To avoid EEG artifacts, the participants were asked not to contract facial muscles and to keep their gaze fixed during the trials. The system did not include any on-line artifact rejection algorithm. However, to check the absence of systematically occurring artifacts, an experienced inspector examined the acquired signals after each training session. In case a systematic artifactual activation was found, the entire session was excluded from the results.

3.2.4 Experimental paradigm (the “flexible” training session)

Each participant took part in 6 training sessions (2 sessions per day). However, to fully customize the training process, we adapted the type and length of each training session depending on the participant’s performances.

First of all, each training session was composed of 1 initial T and a maximum of 16 U repetitions. However, if the average classification accuracy in the last 3 repetitions of U was below 40%, T module was automatically repeated to reset the system’s parameters (and to give the participant an opportunity to try a different imagination strategy). After the reset, the participant could complete the remaining repetitions of U module.

On the other hand, if participants proved to be skilled enough, they had the possibility to finish the session ahead of time. In particular, as soon as the average classification accuracy in the last 6 repetitions of U was above the criterion level of 70%, the participant’s performances were considered good and stable enough and the system automatically switched to C module. Every time C phase was reached, the participant performed 3 repetitions of C and the session ended. Otherwise, the session simply concluded after the 16 repetitions of U module.

To clarify, 3 examples of possible compositions of a session, according to the experimental paradigm, are given in Figure 3.4.

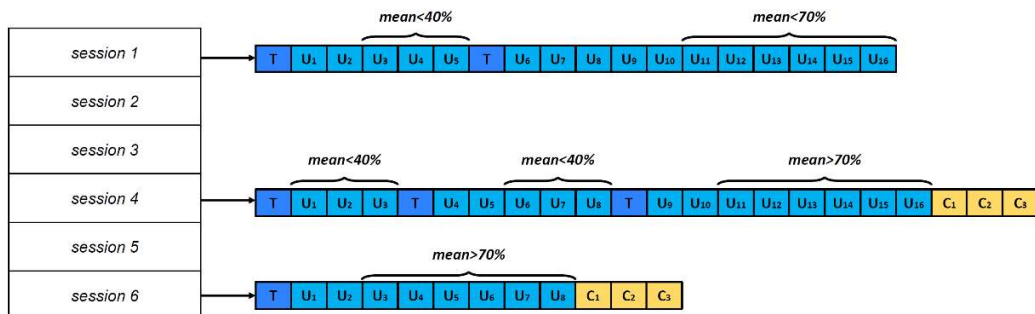


Figure 3.4. In this work, each participant took part in a total of 6 sessions (left). The right part of the figure shows 3 possible compositions of the session. In the top example, T module is repeated because the average accuracy in the previous 3 U repetitions was lower than 40%. At the end of the session, C phase is not even reached because the average accuracy in the last 6 repetitions was $<70\%$. The middle example is similar to the top one (T module is indeed repeated), but this time C phase is reached at the end of the session. Finally, the bottom example shows the case of a shorter session.

3.2.5 System evaluation

Accuracy

As emphasized in (Billinger et al., 2013), one consequence of the increasing interest in BCI research is the tendency of papers to routinely highlight results and methods that

improve accuracy or reduce illiteracy with respect to earlier work. The main limitation is that different (and barely comparable) methods of evaluation are often used, the procedures are not described in sufficient detail, and the value of chance level (i.e. the expected best performance obtainable by chance alone (Billinger et al., 2013)) is not reported for comparison. But showing classification results alone is often not enough, and even accuracies as high as 90% can be meaningless if classes are imbalanced or there are too few trials (Billinger et al., 2013).

In the present work, we report the average classification accuracy together with its chance level p_0 . Since the arrow presentation was generally imbalanced, p_0 was evaluated without loss of generality from confusion matrices, as described in (Billinger et al., 2013). The significance ($\alpha=0.05$) of the difference between mean accuracy and chance level was evaluated through confidence intervals (Billinger et al., 2013).

We briefly review here the computation of p_0 , as in (Billinger et al., 2013). Considering the confusion matrices:

		Predicted labels		
		Class1 (right)	Class2 (left)	
True labels	Class1 (right)	TP	FN	TP+FN
	Class2 (left)	FP	TN	FP+TN
		TP+FP	FN+TN	N (TP+FN+FP+TN)

Figure 3.5. Confusion matrix of the classifier.

TP is the number of “true positive” classified signal portions, FN the “false negative” ones, FP the “false positive”, TN the “true negative”, and $N = (TP + FN + FP + TN)$, the total number of classified signal portions of the session. Given the definition of p_0 from (Billinger et al., 2013)

$$p_0 = \frac{\sum C_{i,:} C_{:,i}}{N^2} \quad (3.1)$$

p_0 is computed as:

$$p_0 = \frac{(TP + FN)(TP + FP) + (FP + TN)(FN + TN)}{(TP + FN + FP + TN)^2} \quad (3.2)$$

As regards the significance of the difference between average accuracy and chance level p_0 using confidence intervals, we computed the lower bound of the confidence interval as in (Billinger et al., 2013):

$$p_l = \hat{p} - z_{1-\frac{\alpha}{2}} \sqrt{\frac{\hat{p}(1-\hat{p})}{N+4}} \quad (3.3)$$

Where $z_{1-\frac{\alpha}{2}}$ is the $1-\alpha/2$ quantile of the standard normal distribution, and

$$\hat{p} = \frac{(TP + TN) + 2}{N + 4} \quad (3.4)$$

is the adjusted average classification accuracy. If $p_0 > p_l$, the average classification accuracy cannot be considered significantly better than chance (Billinger et al., 2013).

We believe average accuracy to be a representative estimation of the user's real ability to control the system. However, as some of the previous works (Faller et al., 2012; Vidaurre et al., 2005, 2006) extensively reported only peak accuracies, we added this information to allow for comparability. Peak accuracy was obtained by computing the average classification accuracy of every time-point of the trial and reporting the peak value (Faller et al., 2012; Vidaurre et al., 2005, 2006). Finally, to be complete, we also report the values of information transfer rate (ITR) (Wolpaw et al., 2002).

As previously explained, T module could be repeated in a session in case performances were too low. The option was introduced to give users the possibility to try different strategies and avoid annoying them with discouraging feedback. In case T module was repeated, we considered for accuracy evaluation only the repetitions of U following the last T . Average accuracy and its chance level are also reported for C , in case it was reached.

As a final note, the reported accuracies reflect the obtained on-line accuracies, without rejection of artifactual trials. To be complete, in a posterior analysis an experienced inspector visually checked the EEG time-courses to reject artifactual data and re-compute the accuracies. During this analysis, the inspector was blinded to the contents of the trials. Since the average rejection rates were overall reasonably low ($8.4 \pm 4.5\%$ of artifactual trials, mean \pm standard deviation) and the re-computed accuracies were not significantly different from the ones without artifact rejection, we decided to only report the values of real obtained on-line accuracies, without artifact rejection.

To evaluate the improvements in participants' performances, we tested the significance of the difference both in peak and average accuracy between the first and the last session.

Time Effect

The system here described is a cue-paced BCI. However, going in the direction of asynchronous BCIs, we think it is important for a system to classify each time-point equally well, since the BCI should recognize the mental state whenever it occurs. To test this ability of the system, we computed the average accuracy curves of each time-point of the trial in the last session, as in (Faller et al., 2012).

Efficacy of the adaptive thresholds

In order to keep challenging the users, encouraging them to produce increasingly separable mental states, we opted for giving feedback only in case the produced EEG patterns exceeded an adaptive threshold from the decision boundary.

In order to check the effect of the thresholds, we computed the r^2 values (Cincotti et al., 2008) for each channel, frequency bin (see the later explanation), participant and session, to compare the conditions of: i) correct classification and *above* threshold, and ii) only correct classification, irrespective of the threshold.

The coefficient of determination r^2 is a commonly used (Cincotti et al., 2008; McFarland et al., 1997b; Vidaurre et al., 2011a; Wolpaw and McFarland, 2004; Wolpaw et al., 2002) index in the BCI context, quantifying how strongly the signals measured under two different task conditions differ in relation to the variance. Specifically, r^2 represents the fraction of the total signal variance which can be explained by the task condition (Cincotti et al., 2008). In this case, r^2 is computed as the square value of the correlation coefficient between the spectral powers of the EEG signal in the two MI tasks, and a fictitious independent variable which assumes one of two possible different values (e.g. “+1” and “-1”) (Cincotti et al., 2008).

For each participant and session, we extracted the power spectral densities of the signal portions using the modified periodogram (Blackman-Harris window). We then evaluated all signal powers in the range 8-30Hz, with 2Hz-large frequency bins. The r^2 value was finally determined for each power bin. For each participant and session, we therefore obtained an ensemble of r^2 values which can be grouped according to three factors:

1. the factor “threshold”, with the two levels “correctly classified and above threshold” and “correctly classified irrespective of threshold”
2. the factor “channel”, with eleven levels (the number of acquired channels)
3. the factor “frequency”, with eleven levels corresponding to the number of 2Hz-large frequency bins in the range 8-30Hz

We evaluated the effect of the “threshold” by performing statistical analysis of the r^2 values. We specifically compared the conditions of “correctly classified and over threshold” and “correctly classified independently from the threshold” signals, by using a three-way ANOVA (with factors “threshold”, “channel” and “frequency”) together with multiple comparisons (corrected with the Tukey’s Honest Significant Difference procedure). Secondly, we also evaluated the effects of the factors “channel” and “frequency”.

Besides performing statistical comparison, we arranged the r^2 values in topographical maps of the scalp, for a qualitative check of the most separable channels between MI conditions. Some examples of these maps are shown in the results.

3.3 Results

3.3.1 Accuracy

The peak accuracies, average accuracies and their chance level are detailed in Table 3.2 (see the Appendix), and summarized in Figure 3.6. Table 3.S1 in the Supplementary Materials additionally reports the detailed compositions of each training session. The sixth session of P02 is not reported because of artifacts in the EEG recordings.

Figure 3.6 shows that seven out of ten participants reached the criterion level of 70% not only with peak but also with average accuracy. All participants accessed indeed the *C* phase at least once, and confirming the average accuracy in their last *U* (Table 3.2). Participants P01-P03 also reached peak accuracies over 90% in their last session. On the other hand, participants P08-P10 did not reach the criterion level of 70% throughout the 6 sessions, although in P08 and P09 the average classification accuracy was significantly different from chance most of the time.

Despite the results of P08-P10, all the participants increased their performances (both considering peak and average accuracy) between the first and last sessions, and the increase was statistically significant over the whole group ($p < 0.01$).

3.3.2 Time effect

Figure 3.7 displays the trial average accuracy curves of all participants in their last session. The figure shows that the classifier was not optimized for any specific time-segment, indeed all time-points were generally classified equally well.

3.3.3 Efficacy of the adaptive thresholds

The three-way ANOVA revealed significantly ($p < 0.01$) higher r^2 values when considering the “correctly classified and above threshold” with respect to the generically “correctly classified” signals. In Figure 3.8, several examples of r^2 topographical maps in the two conditions are shown. In Figure 3.8, three participants with very different levels of control were picked (P03, P06, P10).

The three-way ANOVA also revealed significant ($p < 0.01$) effects for the factors “frequency” and “channel”. Specifically, the bins 8-10Hz, 10-12Hz and 12-14Hz had clearly higher r^2 values for the factor “frequency”.

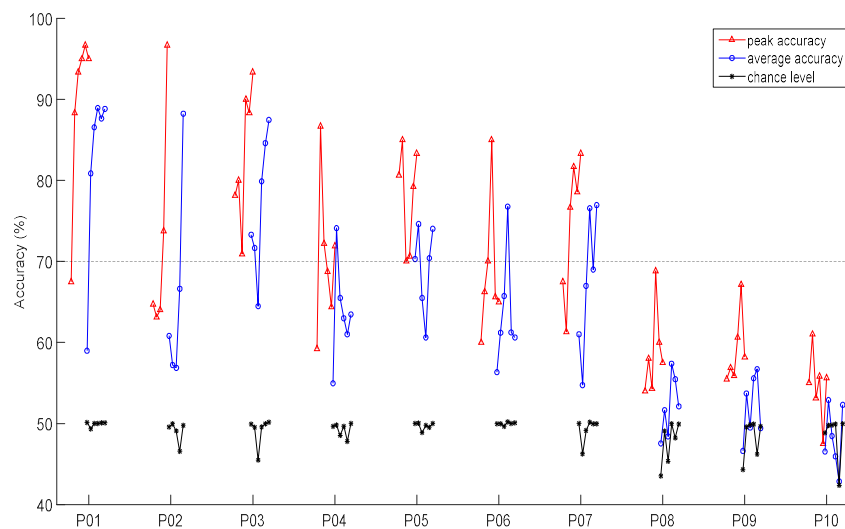


Figure 3.6. This picture shows the trends over the 6 sessions for peak accuracy (red), average accuracy (blue) and chance level p_0 (black) for each participant. As described in section 3.2.4, all the accuracies were computed considering the U repetitions following the last T of the session. Since each average accuracy should be compared to the corresponding p_0 , the blue line of the average and the black line of chance level are aligned. A black horizontal dashed lined indicating the criterion level of 70% is also added.

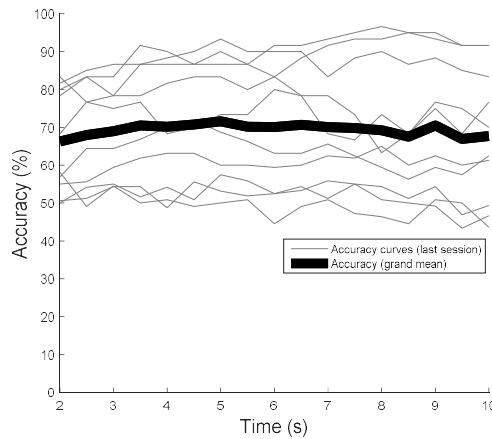


Figure 3.7. Overview of the trial average accuracy curves for the last session in all participants. Each grey line represents the average accuracy curve of a participant, while the black bold line is computed as the grand mean of the accuracy curves of all participants

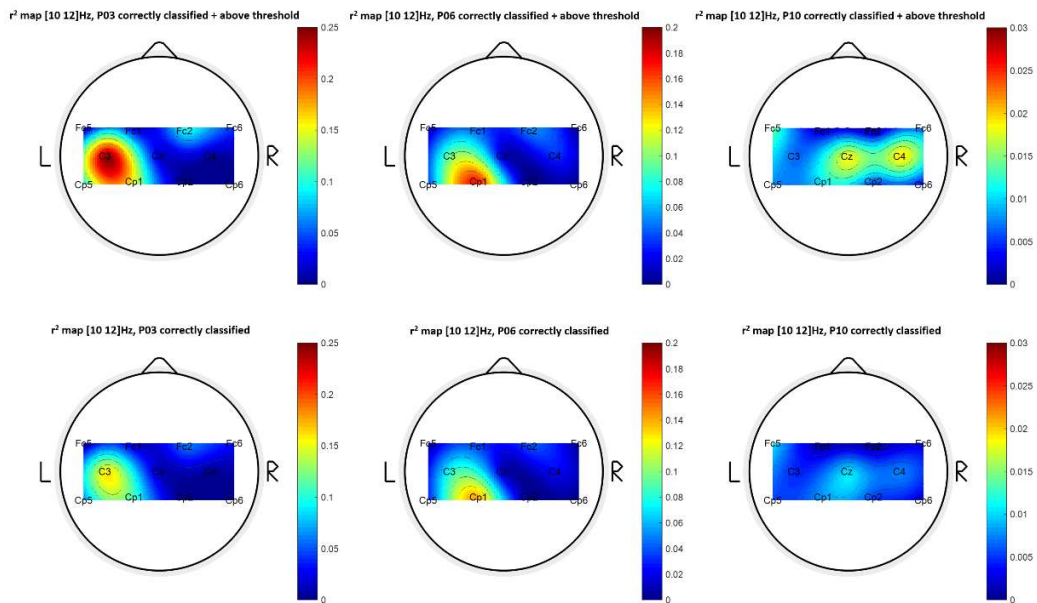


Figure 3.8. Three examples of r^2 maps in subject-specific frequency bins. We chose to display 3 participants who exhibited very different levels of BCI control: P03, P06 and P10. The figure shows how the r^2 maps resulting from “correctly classified + above threshold” signals (upper part of the figure) for each participant present approximately the same shape but higher values than the case of “correctly classified” signals without threshold (lower part of the figure). To allow for comparability, the corresponding maps in the upper/lower part of the figure share the same colourmap bounds.

3.4 Discussion

3.4.1 Accuracy

The results showed a significant ($p < 0.01$) increase in performance (both in peak and average accuracy) between the first and the last sessions over the whole set of participants. Seven out of ten participants reached the criterion level of 70% with both peak and average accuracy, and three of them (P01-P03) even obtained $>90\%$ peak accuracy in their last session. Three out of ten users did not manage to reach the criterion level throughout the six sessions. However, this result is in line with the well-known phenomenon of BCI illiteracy, estimating that BCI control does not work for the 15% to 30% of the users (Dickhaus et al., 2009).

Altogether, our results are in line with the ones of other co-adaptive BCIs, like the ones in (Faller et al., 2012; Vidaurre et al., 2005, 2006) and (Xia et al., 2012).

3.4.2 Time effect

The results in Figure 3.7 show the ability of the system to classify the EEG data in each time-point equally well and not only in a short and limited time window. The result is enhanced by the longer duration of our trial with respect to other studies (Faller et al., 2012; Vidaurre et al., 2005, 2006, 2007). This property makes the system suitable for continuous work as in a real condition of use.

3.4.3 Efficacy of the adaptive thresholds

The computed r^2 values proved to be significantly ($p < 0.01$) higher in the case of “correctly classified and above threshold” signals with respect to the simply “correctly classified” signals, and the result is enhanced by the fact that the “correctly classified” signals include the “correctly classified and above threshold” signals. The outcome suggests that the adaptive thresholds were actually useful to give feedback only on the most reliable and clear mental states the participant could produce. The feature is further independent from the participant’s level of control. The topographical maps in Figure 3.8 show indeed how the above-threshold r^2 values have similar shape but higher values with respect to the other condition, and this holds for all the three subjects, despite their very different level of control.

The beneficial effect of the thresholds is particularly evident in P10 (Figure 3.8). Even though this participant could not control the system (Figure 3.6), the adaptive thresholds allowed to select the “best” signal portions to give feedback on. The shape and frequency bins of the corresponding r^2 maps additionally resemble the

physiological ERD/ERS MI patterns, although with weaker values than participants with higher control level, like P03 and P06 (Figure 3.8).

3.4.4 Possible improvements

The stability against artifacts is the main limitation of our work, and a point of design that should be improved. An online artifact recognition algorithm, like the ones in (Faller et al., 2013), (Winkler et al., 2011) and (Nolan et al., 2010)) should be included in future designs. The real-time exclusion of artifacts would additionally increase the quality of the training set, improving the stability of the **W** matrix, the system's accuracy to recognize the classes, and therefore the quality of the feedback given to the user.

Another simple improvement that may be attempted regards the type of presented feedback. Provided that some EEG non-stationarities come up as reactions to negative feedbacks (Jatzev et al., 2008), the inclusion of only positive rewards may improve the stability of the system and the performance of the classifier. In addition, the presentation of biased feedback should help to better motivate the participants, making the training session more engaging and, definitively, more effective (Barbero and Grosse-Wentrup, 2010).

3.4.5 Overall comments

Taking the above results and discussions together, we can say that the presented adaptive system yields results in line with previously reported findings (Faller et al., 2012; Vidaurre et al., 2005, 2006, 2007). However, beyond the proposed adaptive strategy, we believe the main novelties in this work regard the way the machine interacts with the user during training.

In regard to the inclusion of adaptive thresholds, statistical results and r^2 topographies suggest not only that the threshold selected the most discriminable patterns to give feedback on, but they also worked well in users with very low BCI control (e.g. participant P10, see Figure 3.6 and 3.8), and helped to select patterns with reasonable channel/frequency distribution (Figure 3.8). The adaptivity of the thresholds may also be considered a beneficial point of design, as it challenges the user, making training more engaging. For these reasons, the inclusion of adaptive thresholds is a point that we suggest, and that might be included even in systems different from ours.

One second idea we would suggest in future designs is the unbalancing in the training conditions, in favour of the one which is currently the hardest to predict. We believe this modification may be beneficial for the training process, irrespectively of the underlying adaptive algorithm. On one side, the imbalance is beneficial for the system,

as the increased availability of “examples” of the most difficult class increases the chance the classifier learns how to recognize it. On the other side, it is beneficial for the user, who has more chance to practice his/her strategies and learn how to produce an effective modulation of his/her SMR rhythms.

A final point we would suggest to be included in future designs is the “flexible training session”. Especially with novice users, it may indeed happen that participants need some trial-and-error before coming up with a good imagination strategy (e.g. tapping a finger, playing an instrument, brushing their teeth). In these cases, if the classifier keeps performing at chance level for too long, it may be pertinent to discard all the acquired data and restart training from the beginning, thereby preventing to discourage the user and giving him/her the chance to try a different imagination strategy. On the other hand, as users reach a satisfactory level of control, the training phase should not be needlessly long to avoid boring them, and the paradigm may change to another condition (for example the *C* module, in this case, or it may be a change of environment, like for example entering a different level of a game). Beyond the possible details in the design, the concept we would like to suggest is that thinking about flexible and customizable designs may be a key aspect to boost user training, making it as much tailored as possible to the characteristics of each person.

3.5 Conclusion

In this study, we presented an automated, co-adaptive BCI system to control the behaviour of a 1DOF-modelled arm on a screen using a MI strategy. The system was tested online with ten participants, of whom seven reached the criterion level of 70% both with peak and average accuracy in just three days. Despite these results, the system presents the major limitation of not being completely robust against EEG artifacts. In particular, in the considered frequency band (8-30Hz), muscular artifacts are the most critical. The inclusion of an artifact recognition algorithm should theoretically further improve the system’s stability and the quality of the feedback. Another simple improvement to the system could stem from the decision to display only correct feedback, to prevent the EEG non-stationarities that come up as reactions to frustrating feedback, and to motivate the participants as much as possible.

The presented system falls within the category of co-adaptive BCIs, which aim at the improvement of user training by introducing i) a short calibration phase and ii) adaptivity of the system parameters, to deal with the non-stationarities induced by feedback training. Besides including these aspects, in this work we suggest three ideas/novelties that might be integrated in future designs, namely: i) the introduction of adaptive thresholds to give feedback, ii) the presentation of imbalanced training conditions, in favour of the most misclassified one, iii) the adaptation of the type and

length of the training session, depending on the user behaviour. Altogether, we suggest that going in the direction of building a fully flexible and customizable design may be a key aspect to boost user training, making it as tailored as possible to the characteristics of each person, and thus promoting a better synergy between the user and the machine.

3.6 Appendix

Table 3.2. Detailed results for each participant and session. The first 2 columns list the name of the participant and the number of sessions. The third, fourth and fifth columns show, respectively, the peak accuracy (%), average accuracy (%) and chance level (%) obtained considering the U repetitions following the last T of each session. The sixth column shows the result of the comparison via confidence intervals ($\alpha=0.05$) between the average accuracy and p_0 (Yes= average accuracy significantly different from chance, No=otherwise). The seventh column finally refers to the ITR (bits/min) of the corresponding session. In case C phase was reached, the last 4 columns show, respectively, the average accuracy (%), the chance level p_0 (%), the result of comparison between the two ($\alpha=0.05$), and the ITR (bits/min) considering the three repetitions of C .

Participant	Session	U					C					
		(peak)	(mean)	p_0 (chance)	%	α (0.05)	ITR (bits/min)	(mean)	p_0 (chance)	%	α (0.05)	ITR (bits/min)
P01	1	67.50	58.89	50.14		Yes	2.76	-	-	-	-	-
	2	88.33	80.88	49.34		Yes	35.53	89.10	51.72	Yes	60.37	
	3	93.33	86.57	50.00		Yes	51.70	90.74	61.65	Yes	66.59	
	4	95.00	88.92	50.00		Yes	59.72	84.95	58.91	Yes	46.67	
	5	96.67	87.65	50.08		Yes	55.27	96.53	51.99	Yes	93.91	
	6	95.00	88.82	50.10		Yes	59.37	91.08	49.73	Yes	67.95	
P02	1	64.71	60.83	49.56		Yes	4.09	-	-	-	-	
	2	63.13	57.21	49.95		Yes	1.80	-	-	-	-	
	3	64.00	56.88	49.08		Yes	1.64	-	-	-	-	
	4	73.75	66.62	46.56		Yes	9.75	66.46	57.35	Yes	9.56	
	5	96.67	88.24	49.78		Yes	57.29	92.22	54.78	Yes	72.67	
P03	1	78.13	73.31	49.94		Yes	19.56	83.46	54.71	Yes	42.35	
	2	80.00	71.67	49.53		Yes	16.81	58.78	48.91	Yes	2.68	
	3	70.91	64.49	45.49		Yes	7.38	87.18	58.77	Yes	53.70	
	4	90.00	79.90	49.57		Yes	33.13	81.91	54.70	Yes	38.16	
	5	88.33	84.61	49.98		Yes	45.65	77.09	54.26	Yes	26.83	
	6	93.33	87.45	50.16		Yes	54.61	82.53	51.51	Yes	39.80	

P04	1	59.23	54.98	49.66	Yes	0.86	-	-	-	-
	2	86.67	74.12	49.82	Yes	21.0	74.82	54.54	Yes	22.31
	3	72.22	65.49	48.52	Yes	8.45	60.20	48.75	Yes	3.63
	4	68.75	62.98	49.66	Yes	5.90	-	-	-	-
	5	64.38	60.99	47.80	Yes	4.22	-	-	-	-
	6	71.88	63.46	50.01	Yes	6.35	-	-	-	-
P05	1	80.63	70.29	50.00	Yes	14.68	68.01	49.83	Yes	11.49
	2	85.00	74.61	50.04	Yes	21.91	73.34	55.29	Yes	19.62
	3	70.00	65.49	48.89	Yes	8.45	50.45	45.24	Yes	0.01
	4	70.63	60.62	49.76	Yes	3.94	-	-	-	-
	5	79.23	70.41	49.54	Yes	14.85	66.13	48.81	Yes	9.17
	6	83.33	74.02	50.01	Yes	20.83	74.22	49.05	Yes	21.19
P06	1	60.00	56.32	49.95	Yes	1.39	-	-	-	-
	2	66.25	61.21	49.98	Yes	4.39	-	-	-	-
	3	70.00	65.74	49.66	Yes	8.72	47.09	39.73	Yes	0.29
	4	85.00	76.76	50.21	Yes	26.15	80.00	51.04	Yes	33.37
	5	65.63	61.25	50.00	Yes	4.42	-	-	-	-
	6	65.00	60.62	50.07	Yes	3.94	-	-	-	-
P07	1	67.50	60.99	50.00	Yes	4.22	-	-	-	-
	2	61.33	54.75	46.26	Yes	0.78	-	-	-	-
	3	76.67	66.96	49.16	Yes	10.16	50.94	42.90	Yes	0.03
	4	81.67	76.57	50.16	Yes	25.75	73.44	51.23	Yes	19.79
	5	78.57	68.99	49.96	Yes	12.81	58.49	46.54	Yes	2.51
	6	83.33	76.96	49.95	Yes	26.56	61.15	47.57	Yes	4.34
P08	1	54.00	47.53	43.53	Yes	0.21	-	-	-	-
	2	58.00	51.65	49.07	No	0.09	-	-	-	-
	3	54.29	48.40	45.33	Yes	0.09	-	-	-	-
	4	68.82	57.37	49.96	Yes	1.89	-	-	-	-
	5	60.00	55.48	48.23	Yes	1.04	-	-	-	-
	6	57.50	52.11	49.93	Yes	0.15	-	-	-	-
P09	1	55.45	46.63	44.30	Yes	0.39	-	-	-	-
	2	56.88	53.71	49.58	Yes	0.48	-	-	-	-

	3	55.88	49.48	49.84	No	0.01	-	-	-	-
	4	60.62	55.59	49.94	Yes	1.08	-	-	-	-
	5	67.14	56.72	46.21	Yes	1.57	-	-	-	-
	6	58.18	49.41	49.66	No	0.01	-	-	-	-
P10	1	55.00	46.54	48.85	No	0.41	-	-	-	-
	2	61.00	52.88	49.79	Yes	0.29	-	-	-	-
	3	53.13	48.46	49.80	No	0.08	-	-	-	-
	4	55.83	45.93	49.92	No	0.57	-	-	-	-
	5	47.50	42.87	42.37	No	1.77	-	-	-	-
	6	55.63	52.32	49.98	Yes	0.19	-	-	-	-

3.7 Supplementary Material

Table 3.S1. This table shows the detailed sequences of *T*, *U* and *C* for each participant and session. In line with the previous results, the sequences of the 6th session of S02 are not shown because of artifacts in the EEG.

Participant	S	Sequence
P01	1	T U ₁ U ₂ U ₃ U ₄ U ₅ U ₆ U ₇ U ₈ T U ₉ U ₁₀ U ₁₁ U ₁₂ U ₁₃ U ₁₄ U ₁₅ U ₁₆
	2	T U ₁ U ₂ U ₃ U ₄ U ₅ U ₆ C ₁ C ₂ C ₃
	3	T U ₁ U ₂ U ₃ U ₄ U ₅ U ₆ C ₁ C ₂ C ₃
	4	T U ₁ U ₂ U ₃ U ₄ U ₅ U ₆ C ₁ C ₂ C ₃
	5	T U ₁ U ₂ U ₃ U ₄ U ₅ U ₆ C ₁ C ₂ C ₃
	6	T U ₁ U ₂ U ₃ U ₄ U ₅ U ₆ C ₁ C ₂ C ₃
P02	1	T U ₁ U ₂ U ₃ U ₄ U ₅ U ₆ U ₇ U ₈ U ₉ U ₁₀ U ₁₁ U ₁₂ U ₁₃ U ₁₄ U ₁₅ U ₁₆
	2	T U ₁ U ₂ U ₃ U ₄ U ₅ U ₆ U ₇ U ₈ U ₉ U ₁₀ U ₁₁ U ₁₂ U ₁₃ U ₁₄ U ₁₅ U ₁₆
	3	T U ₁ U ₂ U ₃ U ₄ U ₅ U ₆ T U ₇ U ₈ U ₉ U ₁₀ U ₁₁ U ₁₂ U ₁₃ U ₁₄ U ₁₅ U ₁₆
	4	T U ₁ U ₂ U ₃ U ₄ U ₅ U ₆ U ₇ U ₈ T U ₉ U ₁₀ U ₁₁ U ₁₂ U ₁₃ U ₁₄ U ₁₅ U ₁₆ C ₁ C ₂ C ₃
	5	T U ₁ U ₂ U ₃ U ₄ U ₅ U ₆ C ₁ C ₂ C ₃

P03	1	T U ₁ U ₂ U ₃ U ₄ U ₅ U ₆ U ₇ U ₈ U ₉ U ₁₀ U ₁₁ U ₁₂ U ₁₃ U ₁₄ U ₁₅ U ₁₆ C ₁ C ₂ C ₃
	2	T U ₁ U ₂ U ₃ U ₄ U ₅ U ₆ C ₁ C ₂ C ₃
	3	T U ₁ U ₂ U ₃ U ₄ U ₅ U ₆ U ₇ U ₈ U ₉ U ₁₀ U ₁₁ C ₁ C ₂ C ₃
	4	T U ₁ U ₂ U ₃ U ₄ U ₅ U ₆ C ₁ C ₂ C ₃
	5	T U ₁ U ₂ U ₃ U ₄ U ₅ U ₆ C ₁ C ₂ C ₃
	6	T U ₁ U ₂ U ₃ U ₄ U ₅ U ₆ C ₁ C ₂ C ₃
P04	1	T U ₁ U ₂ U ₃ T U ₄ U ₅ U ₆ U ₇ U ₈ U ₉ U ₁₀ U ₁₁ U ₁₂ U ₁₃ U ₁₄ U ₁₅ U ₁₆
	2	T U ₁ U ₂ U ₃ U ₄ U ₅ U ₆ C ₁ C ₂ C ₃
	3	T U ₁ U ₂ U ₃ U ₄ U ₅ U ₆ U ₇ U ₈ U ₉ C ₁ C ₂ C ₃
	4	T U ₁ U ₂ U ₃ U ₄ U ₅ U ₆ U ₇ U ₈ U ₉ U ₁₀ U ₁₁ U ₁₂ U ₁₃ U ₁₄ U ₁₅ U ₁₆
	5	T U ₁ U ₂ U ₃ U ₄ U ₅ U ₆ U ₇ U ₈ U ₉ U ₁₀ U ₁₁ U ₁₂ U ₁₃ U ₁₄ U ₁₅ U ₁₆
	6	T U ₁ U ₂ U ₃ U ₄ U ₅ U ₆ U ₇ U ₈ U ₉ U ₁₀ U ₁₁ U ₁₂ U ₁₃ U ₁₄ U ₁₅ U ₁₆
P05	1	T U ₁ U ₂ U ₃ U ₄ U ₅ U ₆ U ₇ U ₈ U ₉ U ₁₀ U ₁₁ U ₁₂ U ₁₃ U ₁₄ U ₁₅ U ₁₆ C ₁ C ₂ C ₃
	2	T U ₁ U ₂ U ₃ U ₄ U ₅ U ₆ C ₁ C ₂ C ₃
	3	T U ₁ U ₂ U ₃ T U ₄ U ₅ U ₆ U ₇ U ₈ U ₉ U ₁₀ U ₁₁ U ₁₂ U ₁₃ U ₁₄ U ₁₅ U ₁₆ C ₁ C ₂ C ₃
	4	T U ₁ U ₂ U ₃ U ₄ U ₅ U ₆ U ₇ U ₈ U ₉ U ₁₀ U ₁₁ U ₁₂ U ₁₃ U ₁₄ U ₁₅ U ₁₆
	5	T U ₁ U ₂ U ₃ U ₄ U ₅ U ₆ U ₇ U ₈ U ₉ U ₁₀ U ₁₁ U ₁₂ U ₁₃ C ₁ C ₂ C ₃
	6	T U ₁ U ₂ U ₃ U ₄ U ₅ U ₆ C ₁ C ₂ C ₃
P06	1	T U ₁ U ₂ U ₃ U ₄ U ₅ U ₆ U ₇ U ₈ U ₉ U ₁₀ U ₁₁ U ₁₂ U ₁₃ U ₁₄ U ₁₅ U ₁₆
	2	T U ₁ U ₂ U ₃ U ₄ U ₅ U ₆ U ₇ U ₈ U ₉ U ₁₀ U ₁₁ U ₁₂ U ₁₃ U ₁₄ U ₁₅ U ₁₆
	3	T U ₁ U ₂ U ₃ U ₄ U ₅ U ₆ U ₇ U ₈ U ₉ U ₁₀ U ₁₁ U ₁₂ U ₁₃ U ₁₄ U ₁₅ U ₁₆ C ₁ C ₂ C ₃
	4	T U ₁ U ₂ U ₃ U ₄ U ₅ U ₆ C ₁ C ₂ C ₃
	5	T U ₁ U ₂ U ₃ U ₄ U ₅ U ₆ U ₇ U ₈ U ₉ U ₁₀ U ₁₁ U ₁₂ U ₁₃ U ₁₄ U ₁₅ U ₁₆
	6	T U ₁ U ₂ U ₃ U ₄ U ₅ U ₆ U ₇ U ₈ U ₉ U ₁₀ U ₁₁ U ₁₂ U ₁₃ U ₁₄ U ₁₅ U ₁₆
P07	1	T U ₁ U ₂ U ₃ U ₄ U ₅ U ₆ U ₇ U ₈ U ₉ U ₁₀ U ₁₁ U ₁₂ U ₁₃ U ₁₄ U ₁₅ U ₁₆
	2	T U ₁ U ₂ U ₃ U ₄ U ₅ U ₆ U ₇ U ₈ U ₉ U ₁₀ U ₁₁ U ₁₂ U ₁₃ U ₁₄ U ₁₅ U ₁₆
	3	T U ₁ U ₂ U ₃ U ₄ U ₅ U ₆ U ₇ U ₈ U ₉ U ₁₀ U ₁₁ U ₁₂ C ₁ C ₂ C ₃
	4	T U ₁ U ₂ U ₃ U ₄ U ₅ U ₆ C ₁ C ₂ C ₃

5 T U₁ U₂ U₃ U₄ U₅ U₆ U₇ C₁ C₂ C₃

6 T U₁ U₂ U₃ U₄ U₅ U₆ C₁ C₂ C₃

P08

1 T U₁ U₂ U₃ U₄ U₅ U₆ U₇ U₈ U₉ U₁₀ U₁₁ T U₁₂ U₁₃ U₁₄ U₁₅ U₁₆

2 T U₁ U₂ U₃ T U₄ U₅ U₆ U₇ U₈ U₉ U₁₀ U₁₁ T U₁₂ U₁₃ U₁₄ U₁₅ U₁₆

3 T U₁ U₂ U₃ U₄ U₅ U₆ U₇ U₈ T U₉ U₁₀ U₁₁ U₁₂ U₁₃ U₁₄ U₁₅ U₁₆

4 T U₁ U₂ U₃ U₄ U₅ U₆ U₇ U₈ U₉ U₁₀ U₁₁ U₁₂ U₁₃ U₁₄ U₁₅ U₁₆

5 T U₁ U₂ U₃ U₄ U₅ U₆ U₇ U₈ U₉ U₁₀ U₁₁ U₁₂ U₁₃ U₁₄ U₁₅ U₁₆

6 T U₁ U₂ U₃ U₄ T U₅ U₆ U₇ U₈ U₉ U₁₀ U₁₁ U₁₂ U₁₃ U₁₄ U₁₅ U₁₆

P09

1 T U₁ U₂ U₃ U₄ U₅ T U₆ U₇ U₈ U₉ U₁₀ U₁₁ U₁₂ U₁₃ U₁₄ U₁₅ U₁₆

2 T U₁ U₂ U₃ U₄ U₅ U₆ U₇ U₈ U₉ U₁₀ U₁₁ U₁₂ U₁₃ U₁₄ U₁₅ U₁₆

3 T U₁ U₂ U₃ U₄ U₅ U₆ U₇ U₈ U₉ U₁₀ U₁₁ U₁₂ U₁₃ U₁₄ U₁₅ U₁₆

4 T U₁ U₂ U₃ U₄ U₅ U₆ U₇ U₈ U₉ U₁₀ U₁₁ U₁₂ U₁₃ U₁₄ U₁₅ U₁₆

5 T U₁ U₂ U₃ U₄ U₅ U₆ U₇ U₈ U₉ T U₁₀ U₁₁ U₁₂ U₁₃ U₁₄ U₁₅ U₁₆

6 T U₁ U₂ U₃ U₄ U₅ U₆ T U₇ U₈ U₉ U₁₀ U₁₁ U₁₂ U₁₃ U₁₄ U₁₅ U₁₆

P10

1 T U₁ U₂ U₃ U₄ U₅ U₆ U₇ U₈ U₉ U₁₀ U₁₁ U₁₂ U₁₃ U₁₄ U₁₅ U₁₆

2 T U₁ U₂ U₃ T U₄ U₅ U₆ T U₇ U₈ U₉ U₁₀ U₁₁ U₁₂ U₁₃ U₁₄ U₁₅ U₁₆

3 T U₁ U₂ U₃ U₄ U₅ U₆ U₇ U₈ U₉ U₁₀ U₁₁ U₁₂ U₁₃ U₁₄ U₁₅ U₁₆

4 T U₁ U₂ U₃ U₄ T U₅ U₆ U₇ U₈ U₉ U₁₀ U₁₁ U₁₂ U₁₃ U₁₄ U₁₅ U₁₆

5 T U₁ U₂ U₃ U₄ T U₅ U₆ U₇ U₈ T U₉ U₁₀ U₁₁ U₁₂ U₁₃ U₁₄ U₁₅ U₁₆

6 T U₁ U₂ U₃ U₄ U₅ U₆ U₇ U₈ U₉ U₁₀ U₁₁ U₁₂ U₁₃ U₁₄ U₁₅ U₁₆

Chapter 4. Online decoding of hand movement for the natural control of an assistive robotic arm

The study described in this chapter has been conducted at the **Institute of Neural Engineering, Graz University of Technology, Austria**, where I had the opportunity to spend an internship. The study builds up on the research activities of the lab, and was conducted in strict collaboration with **Dipl.-Ing. Reinmar Kobler, Ing. Dr. Andreea-Ioana Sburlea, and Prof. Dr. Gernot R. Müller-Putz**.

4.1 Introduction

One of the latest directions of BCI research focuses on the reconstruction of the movement from neural recordings, to allow for intuitive and natural control (Müller-Putz et al., 2016). The ultimate goal is the continuous decoding of real (Ofner and Müller-Putz, 2012) or imagined (Ofner and Müller-Putz, 2015) movements, to use their neural correlates as input for the prosthetic device.

Neural tuning to movement direction has first been shown in monkeys (Caminiti et al., 1990; Georgopoulos et al., 1982; Kalaska et al., 1983). Later, both primate and human studies showed the possibility to extract hand trajectories and velocity profiles from invasive intracortical (Black et al., 2003; Carmena et al., 2003; Hochberg et al., 2012; Lebedev et al., 2005; Li et al., 2009; Mulliken et al., 2008) and ECoG (Pistohl et al., 2008; Schalk et al., 2007) recordings. The feasibility of noninvasive neural decoding has been proved just recently, first in MEG (Bradberry et al., 2009; Georgopoulos et al., 2005; Waldert et al., 2008; Yeom et al., 2013) and lately in EEG (Bradberry et al., 2010; Kobler et al., 2018; Lv et al., 2010; Ofner and Müller-Putz, 2012; Úbeda et al., 2015).

When coming to EEG, research agrees that kinematic information is present in the low frequency band ($<3\text{Hz}$) (Waldert et al., 2009) of the EEG recordings, and that it can be retrieved through linear decoders (Robinson and Vinod, 2016). Several studies could decode positions and velocities from linearly combined low-pass filtered EEG (Bradberry et al., 2010; Ofner and Müller-Putz, 2012), while a recent work clarified the spatiotemporal tuning of EEG to single movement parameters (Kobler et al., 2018).

Building on the findings of the previous works, we took in this study a step further, and implemented for the first time real-time control of an assistive robotic arm by means of continuously EEG-decoded two-dimensional movements.

Given the exploratory nature of the study, we recorded healthy participants and asked them to perform real hand movements. Starting from a condition where the robot was entirely controlled by the participants' hand movement, we gradually increased the proportion of EEG decoding, up to a final condition of 100% EEG-controlled robotic arm. Since this is the first time EEG decoding is performed online, the work will detail the methods used for the purpose, with particular attention to the differences and constraints arising when shifting from offline to online decoding, and closing the loop through the control of the robotic arm. Correlations between the decoder's output and the real movement were evaluated. Analysis of the EEG sources contributing to decoding was completed, for a comparison with previous offline decoding results.

4.2 Methods

4.2.1 Participants

Ten healthy participants (aged 26.5 ± 3.8 years, with normal or corrected-to-normal vision, 5 females) took part in the study, receiving compensatory payment for their participation. The study conformed to the Declaration of Helsinki and was approved by the ethics committee of the Medical University of Graz. All participants gave their written consent to participate in the study.

4.2.2 Experimental setup

During the experiment, participants sat in a shielded room, on a comfortable chair, approximately 1.5m away from a reclined ($\sim 45^\circ$) TV screen (Figure 4.1). An assistive robotic arm (JACO, Kinova Inc., Canada) overlaid the TV, with its hand closed in a grasp and pointing at the TV screen with its fingers.

Similarly to a recent study (Kobler et al., 2018), a planar board supported the participants' right arm. To reduce friction between the arm and the board, participants wore a sleeve and placed their hand on a circular pad. A LeapMotion controller (LeapMotion Inc., USA) held ~ 20 cm over the board, continuously recorded the right hand's palm position. After participants found a comfortable resting position, their right hand was mapped to the center of a fixation cross, displayed on the TV screen.

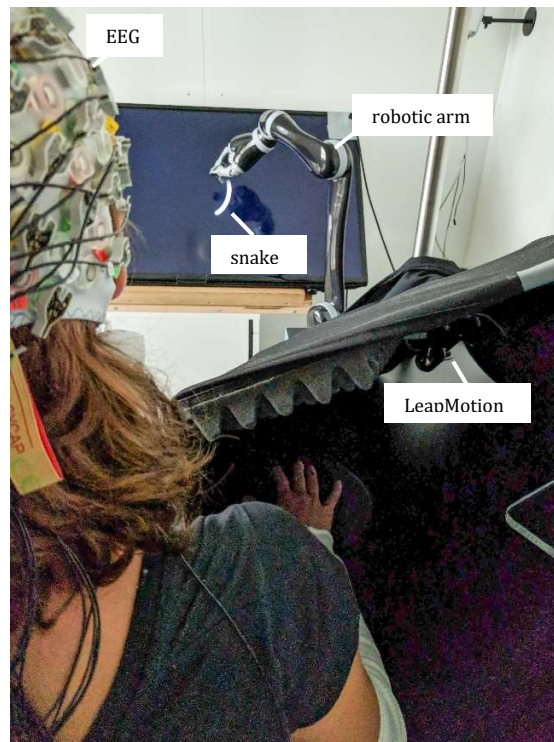


Figure 4.1. Experimental setup. A planar board supported the participants' right arm. A LeapMotion controller (LeapMotion Inc., USA) recorded the right palm movement. Participants' hand movement was 1:1 mapped to the movement of a robotic arm (JACO, Kinova Inc., Canada). 64-channel EEG + 6 EOG (actiCAP Brain Products GmbH, Germany) were recorded at the same time. A moving trace (the "snake") was displayed on the screen. A dark fabric covered the participants' right arm, to ensure it was not in their field of view.

During the experiment, a moving trace (which we called "snake") replaced the fixation cross (Figure 4.1). Participants had the goal to follow the snake with the robotic hand as closely as possible. The movement of the robot congruently mapped the movement of the participants' hand on the board. As participants slid their palm on the board, the robotic hand slid on the reclined screen with movements of the same amplitude (1:1 scaling). The hand movements were occluded from the participants' field of view..

4.2.3 Experimental procedure

The experiment consisted in thirteen runs, out of which seven were used to calibrate the system and six to implement the online decoding. All the runs lasted ~4 hours in total.

The main experimental task was implemented in the "*snakeruns*" (Figure 4.2), where participants had to track the snake with the robotic hand. Two additional "*eyeruns*" were added to calibration, to record eye artifacts (saccades, blinks) and resting activity.

During the “*eyeruns*”, a moving ball appeared on the screen and guided four possible conditions: i) rest with eyes open (9 trials), ii) horizontal eye movements (6 trials), iii) vertical eye movements (6 trials), and iv) blinks (6 trials). Trials lasted 10s each, with 2-3s breaks in between. Conditions ii), iii) and iv) were used to fit a subspace subtraction eye artifact removal algorithm, as detailed in Kobler et al (Kobler et al., 2017).

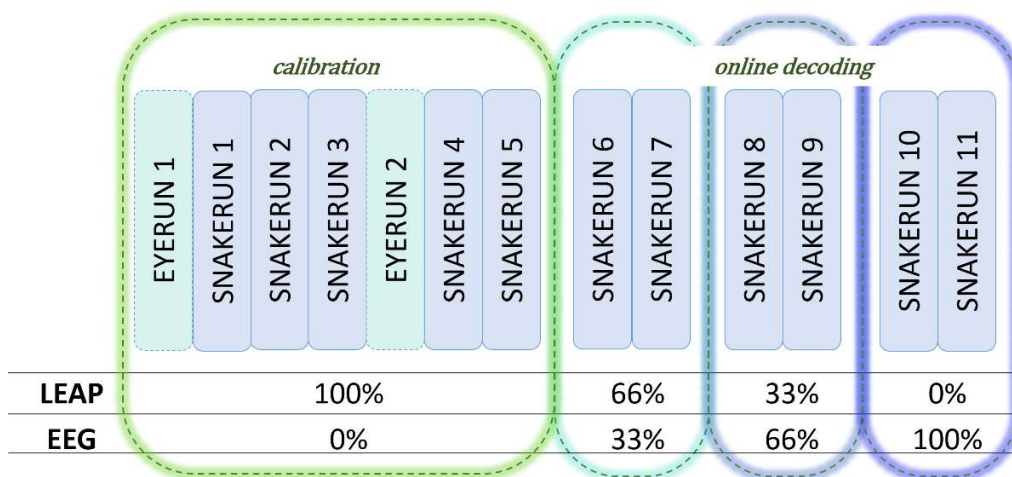


Figure 4.2. Experimental paradigm. After five runs (“*snakeruns*”) of calibration, EEG-decoded trajectories were combined with real hand movement, with an increasing proportion of the former towards the end of the experiment. Two additional runs (“*eyeruns*”) recorded eye movements and blinks, for the calibration of the eye artifact removal algorithm.

During the “*snakerun*” trials, a moving trace (the “snake”) appeared on the screen and continuously moved for 23s. As the snake appeared, participants gained control over the robot, which returned to its resting position at the end of each trial. Timing of the trials was self-paced. During breaks, a fixation cross and a cursor appeared instead of the snake, showing the relative position of the hand with respect to the participant’s resting position (the fixation cross). Whenever participants were ready for a new trial, they moved their hand to the resting position, and a new snake appeared.

As in (Kobler et al., 2018), the snake trajectories were generated offline and were the same across participants. Twelve trajectories were sampled from band-pass filtered (0.2 to 0.4Hz) pink noise, as described in (Paninski et al., 2004). The set of trajectories was extended through rotating (90°, 180° and 270°) and mirroring. This led to a total of 96 trajectories, randomly distributed over the trials of the entire experiment. The procedure ensured uncorrelated positions and velocities across and within horizontal and vertical components (Kobler et al., 2018).

Over the first five *snakeruns*, the robot’s behavior completely mapped the real hand movement. After setting up the decoder, a fraction of EEG-decoded movement was

added to the robot's control signal. The proportion of EEG control gradually increased from 33% in *snakeruns 6-7*, to 66% in *snakeruns 8-9*, to 100% in *snakeruns 10-11* (Figure 4.2). Each *snakerun* was composed of 10 trials, which were aborted and replayed in case broad drift artifacts occurred (see the next sections for details).

4.2.4 Data recording and processing

We recorded and synchronized all data with the lab streaming layer (LSL) protocol (<https://github.com/sccn/labstreaminglayer>).

EEG was recorded through 64 active electrodes (actiCAP Brain Products GmbH, Germany), placed on the scalp according to the 10-10 system (Figure 4.3, left). Reference and ground electrodes were placed at the right mastoid and AFz, respectively. Six additional active electrodes were positioned at the inferior, superior and outer canthi of the eyes to record the EOG (Figure 4.3, right). EEG and EOG signals were recorded at 500Hz through BrainAmp amplifiers (BrainAmp, Brain Products GmbH, Germany).

We implemented the *eyerun* and *snakerun* paradigms in Matlab (Matlab 2015b, Mathworks Inc., USA), using the Psychtoolbox extension (Brainard; Kleiner et al., 2007; Pelli). An additional photodiode, capturing a marker on the screen at the beginning of each trial, was used for offline synchronization.

Online processing and synchronization of data was accomplished through custom Matlab scripts, with the EEGLAB extension (version 14.1.1) (Delorme and Makeig, 2004). The processing pipelines are outlined in Figure 4.4.

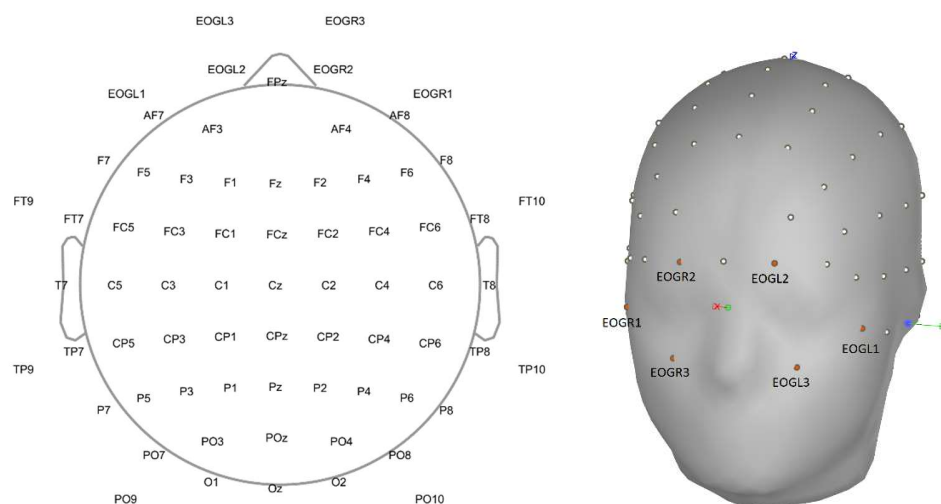


Figure 4.3. EEG and EOG electrode locations in topographical representation (left panel) and after co-registration with the template head model (right panel).

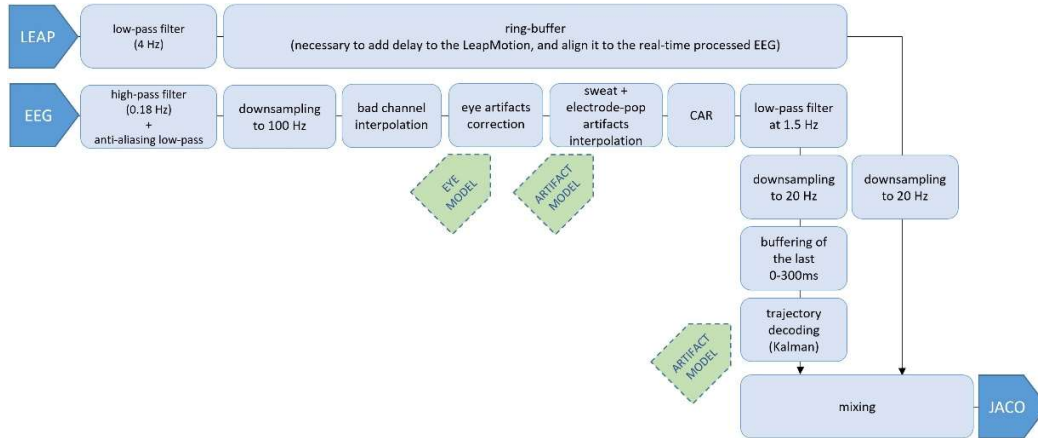


Figure 4.4. Processing pipelines of EEG and LeapMotion data. EEG was filtered in two stages. After the first filtering stage (0.18Hz high-pass + anti-aliasing low-pass), EEG was downsampled to 100Hz, bad channels were interpolated, eye artifacts attenuated, slow drifts/occasional pops detected, and signal were re-referenced to common average reference. After the second filtering stage (1.5Hz low-pass), EEG was downsampled to 20Hz, buffered for 300ms and decoded (linear decoding + Kalman filtering). Meanwhile, kinematic signal from the LeapMotion was low-pass filtered at 4Hz, delayed (ring-buffer) for synchronization with EEG, and downsampled to 20Hz. After synchronization, LeapMotion and EEG-decoded trajectories were mixed into an unique control signal, transformed to the reclined TV screen and fed to the robotic arm.

EEG data processing

EEG signals were filtered and downsampled in two different stages.

In the first stage, EEG data were high-pass filtered at 0.18Hz and downsampled to 100Hz. To avoid aliasing, the filter was composed as a cascade of: i) a first-order IIR high-pass filter with 0.18Hz cut-off frequency, ii) a second order Butterworth low-pass filter at 25Hz, and iii) two Notch filters at 50Hz and 100Hz.

Bad channels were manually selected for each subject during calibration, based on the presence of evident drift, unlikely behavior of the channel, or suspected contamination by movement artifacts (see Table 4.S1, Supplementary Material). The selected channels were online corrected during feedback, through real-time interpolation of the $N = 4$ nearest neighboring electrodes.

After interpolation, saccadic eye movements and blinks were attenuated through a subspace subtraction eye artifact removal algorithm (Kobler et al., 2017), fitted to the *eyeruns* data.

Eye-corrected data were continuously checked for low-frequency artifacts (e.g. occasional pops, drifts), through a variance-based online artifact detection algorithm. The baseline variance of each channel was estimated from the eye-corrected data of the *eyeruns*. Naming v_{base} the baseline variance of each channel, during feedback we

computed the instantaneous variance v_{inst} and compared it to a normal distribution with $\mu = 3 * v_{base}$ and $\sigma = v_{base}$:

$$v_{norm} = \frac{v_{inst} - 3 * v_{base}}{v_{base}} \quad (4.1)$$

Artifact probability was estimated as the normal cumulative probability of v_{norm} (Matlab function *normcdf*). During feedback, artifactual channels were continuously interpolated by using their $N = 4$ most proximal electrodes, with a percentage of interpolation proportional to the artifact probability. In case of contamination of the interpolating channels, we aborted the trial and replayed it at the end of the run.

After artifact detection, EEG was re-referenced to common average reference (CAR), low-pass filtered at 1.5Hz with a second-order low-pass Butterworth, and downsampled to 20Hz.

EEG was finally buffered for 300ms, for multi-lag decoding of the hand kinematics (see the next section for details).

LeapMotion data processing

LeapMotion palm positions were low-pass filtered at 4Hz through a third order low-pass Butterworth, to preserve the movement information (~ 0.2 -1Hz band) while getting rid of occasional jitters due to temporary loss of tracking.

In order to align LeapMotion with the EEG-decoded movements, we evaluated the duration of each processing pipeline, and delayed the signal acquired with the LeapMotion by 165ms by means of a ring-buffer. The computation of delays is depicted in Figure 4.5 and detailed in the following lines.

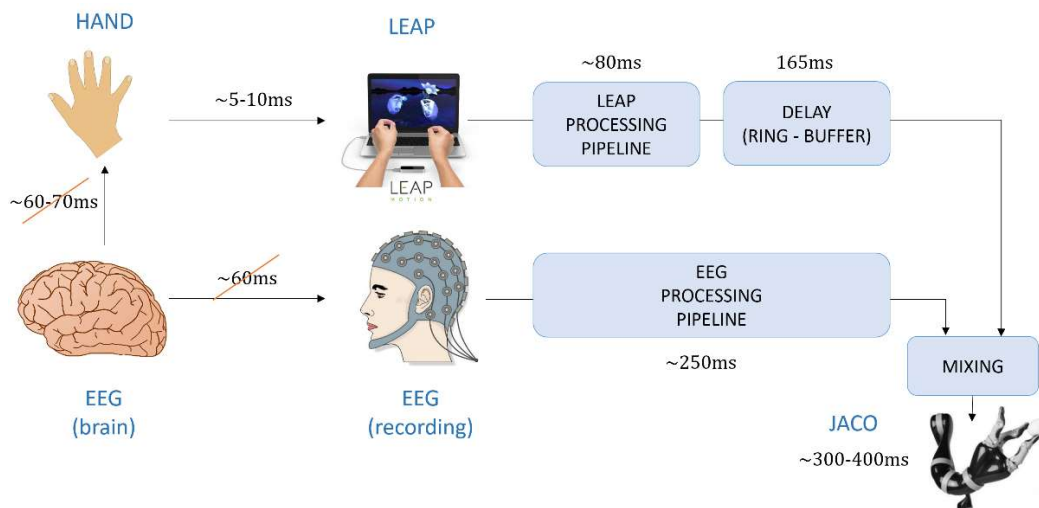


Figure 4.5. Evaluation of delays. Latencies of the recording systems were ~ 60 ms (EEG) and ~ 5 -10ms (LeapMotion). Processing pipelines lasted ~ 250 ms (EEG) and ~ 80 ms (LeapMotion). Considering a delay of ~ 60 -70ms between brain signal and motor output, the resulting delay for synchronization was 165ms.

The latencies of the recording systems were ~60ms for the EEG and ~5-10ms for the LeapMotion, while the processing pipelines lasted ~250ms and ~80ms, respectively. Processing delays were estimated considering the group delay responses of the filters and the frequency content of the signals. If considering an additional ~60-70ms delay between brain signal and inherent motor output, the resulting delay for synchronization was 165ms.

After synchronization, LeapMotion positions were downsampled to 20Hz, and mixed to the EEG.

JACO control

After alignment, real and EEG-decoded trajectories were mixed to control the JACO robotic arm. The proportion of mixing depended on the run, according to the scheme already depicted in Figure 4.2. Position coordinates were transformed with a rotation matrix to make the robot slide on the tilted plane of the TV screen, while amplitude of the movements remained unchanged (1:1 mapping).

Depending on the kinematic behavior of the subject, the robotic arm introduced a delay of 300-400ms between JACO target and actual movement. Altogether, the total delay between hand movement and robot reaction was ~550-650ms (250ms + 300-400ms).

Offline processing

Data were offline processed following the same pipelines as online (Figure 4.4). At the end of calibration, *snakerun* data were collected, processed and epoched into 23s trials. Trials were automatically marked for rejection if the EEG signal of any channel exceeded a threshold of +/- 100uV or had an abnormal probability or kurtosis (more than 5 standard deviations beyond the mean), applying the criteria twice to detect gross outliers in the first iteration and subtle outliers in the second. Marked trials were further visually checked to correct/integrate automatic artifact detection. The proportion of rejected trials was 10 out of 50 calibration trials on average. LeapMotion position data were used to compute velocities and accelerations. This was a necessary step for later decoder fitting and setting up of the Kalman filter (see the next section for details). We used a Savitzky-Golay filter (order three and eleven taps) to smooth and differentiate the hand position signals into velocities and accelerations. The first and last second of each trial were finally excluded to eliminate edge artifacts.

After the experiment, feedback runs were processed in the same way as calibration runs. One of the subjects was excluded from the analysis of the feedback runs due to technical problems in the recordings. The proportion of rejected trials was 10 out of 60 feedback trials on average.

4.2.5 Decoder fitting and Kalman filter

Decoder fitting

Likewise previous decoding studies (Kobler et al., 2018; Ofner and Müller-Putz, 2015), we applied partial least squares (PLS) (Wold et al., 2001) to find the linear decoder models of movement parameters from the EEG data. PLS is particularly appropriate in situations with strongly collinear predictor variables, as in the case of multi-lag low-frequency EEG.

Let \mathbf{X} be an $n \times P$ matrix of predictor variables, with n observations and P predictors, like the multi-lag EEG data. Let \mathbf{Y} be the $n \times M$ matrix of response variables with M responses, like the six movement parameters (positions, velocity and accelerations in x and y dimensions).

The predictor variables are modelled as:

$$X = X_S \cdot X_L^T + E \quad (4.2)$$

with \mathbf{X}_S being an $n \times N_{comp}$ matrix of latent components, \mathbf{X}_L being the $P \times N_{comp}$ matrix to relate the predictors \mathbf{X} to their latent space, and \mathbf{E} being an $n \times P$ matrix of additive independent and identically distributed (iid) noise.

With PLS regression, the idea is finding the latent components \mathbf{X}_S maximizing the covariance with the dependent variables in \mathbf{Y} , given the number of components N_{comp} . This permits to find the linear relation between the \mathbf{X} and \mathbf{Y} , while reducing the dimension from P to N_{comp} . The dependent variables are then modelled as:

$$Y = X_S \cdot Y_L^T + G \quad (4.3)$$

with \mathbf{Y}_L being the $M \times N_{comp}$ matrix relating \mathbf{Y} with the predictor scores \mathbf{X}_S , and \mathbf{G} being a matrix of additive iid noise.

\mathbf{X}_L and \mathbf{Y}_L were estimated with the SIMPLS algorithm (de Jong, 1993). The estimates may also be combined into a $P \times M$ weight matrix \mathbf{W} , to directly predict the dependent variable from the EEG:

$$\hat{Y} = X \cdot W \quad (4.4)$$

In this study, we fitted the decoder to the entire calibration set (Figure 4.2), obtained by concatenation of clean trials from *snakeruns1-5*. Although eye movement artifacts were strongly attenuated by the eye correction algorithm (Kobler et al., 2017), pilot subjects revealed that subtle residual activity might remain in the very frontal locations.

In order to rule out any residual interference, we removed the five electrodes from the Fp and AF row (Figure 4.3), fitting the model to the remaining 59 channels. The dataset was extended over the seven considered lags, i.e. lag 0, -50ms, -100ms, -150ms, -

200ms, -250ms and -300ms, with a result of 59 channels x 7 = 413 highly collinear predictor variables. For dimensionality reduction, we adopted $N_{comp} = 85$ components, explaining ~99% of \mathbf{X} variance.

Kalman filter

The Kalman filter (Kalman, 1960) is an optimal estimation algorithm to infer the internal *state* of a system, given a set of indirect noisy measurements and the system's underlying model.

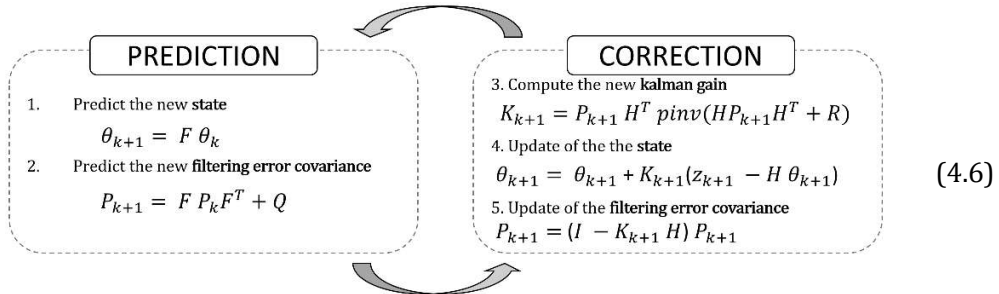
Kalman filter is composed of two equations. The first, called *process equation*, describes the evolution of the internal state over time. The second, called *measurement equation*, describes the relation between the noisy measures and the state. In its discrete-time and linear form, Kalman filter equations can be written as follows:

$$\begin{cases} \theta_{k+1} = F\theta_k + v_k & v \sim N(0, Q) \\ z_k = H\theta_k + w_k & w \sim N(0, R) \end{cases} \quad (4.5)$$

The first line the *process equation*, where θ is the n_θ -dimensional state of the system, \mathbf{F} is the $n_\theta \times n_\theta$ transition matrix between the present k and next $k+1$ sample, and v is additive Gaussian noise with zero-mean and covariance matrix \mathbf{Q} , modelling the uncertainty over the process equation.

The second line is the *measurement equation*, linking the n_z -dimensional vector of measurements z to the n_θ -dimensional state θ through the linear relation described by the $n_z \times n_\theta$ matrix \mathbf{H} , while w is additive Gaussian noise with zero-mean and covariance matrix \mathbf{R} , modelling the measurement and model errors.

When setting up the Kalman filter, a reasonable estimation of the covariance matrices \mathbf{Q} and \mathbf{R} is needed. The idea of Kalman filtering is to find the optimal combination of the noisy state predictions (process equation) and noisy estimations (measurement equation), based on the characteristics of the process and measurement noises. The goal is achieved by means of an algorithm alternating the two phases of (i) prediction of the new state θ_{k+1} and its covariance matrix \mathbf{P}_{k+1} , and (ii) correction of the estimate with the measurement z_{k+1} , taking into account the system uncertainties (\mathbf{Q} and \mathbf{R}) and structure (\mathbf{F} and \mathbf{H}) by means of the Kalman gain.



In our study, the status was the hand kinematics, inferred from the noisy EEG measures. We therefore defined the status θ :

$$\theta = [p_x \quad v_x \quad a_x \quad p_y \quad v_y \quad a_y]^T \quad (4.7)$$

containing all the kinematic chain from positions to accelerations (model with null jerk).

Let T be the integration step (in our case $T = 1/20$, from the pipeline in Figure 4.4), the \mathbf{F} and \mathbf{Q} matrices are then:

$$\mathbf{F} = \begin{bmatrix} 1 & T & T^2/2 & 0 & 0 & 0 \\ 0 & 1 & T & 0 & 0 & 0 \\ 0 & 0 & 1 & 0 & 0 & 0 \\ 0 & 0 & 0 & 1 & T & T^2/2 \\ 0 & 0 & 0 & 0 & 1 & T \\ 0 & 0 & 0 & 0 & 0 & 1 \end{bmatrix} \quad (4.8)$$

$$\mathbf{Q} = \begin{bmatrix} T^5/20 & T^4/8 & T^3/6 & 0 & 0 & 0 \\ T^4/8 & T^3/3 & T^2/2 & 0 & 0 & 0 \\ T^3/6 & T^2/2 & T & 0 & 0 & 0 \\ 0 & 0 & 0 & T^5/20 & T^4/8 & T^3/6 \\ 0 & 0 & 0 & T^4/8 & T^3/3 & T^2/2 \\ 0 & 0 & 0 & T^3/6 & T^2/2 & T \end{bmatrix} \cdot \frac{1}{10} \cdot \frac{\text{var}(a)}{T} \quad (4.9)$$

The \mathbf{F} matrix models the integration between θ variables, while \mathbf{Q} describes the propagation of the noise on accelerations (the model assumes null jerk) to velocities and positions (Bar-Shalom et al., 2002).

In regard to the measurement equation, the idea was using the EEG measurements to estimate the kinematic variables in θ , i.e. using the decoder model. However, in order to reduce redundancy and increase speed, we considered as measurement vector z the $N_{comp} = 85$ latent components \mathbf{X}_s , instead of the $P = 413$ variables in \mathbf{X} . As a result of Equation 4.3, the Kalman filter matrix \mathbf{H} was:

$$\mathbf{H} = \text{pinv}(Y_L) \quad (4.10)$$

The covariance matrix of the measurement error \mathbf{R} was finally obtained applying its definition, evaluated on calibration data:

$$\mathbf{R} = [\text{cov}(z - \hat{z})]_{\text{calibration}} = [\text{cov}(z - \mathbf{H}\theta)]_{\text{calibration}} \quad (4.11)$$

with z being the latent variables projected from the measured EEG, and \hat{z} being their estimation according to the LeapMotion measures θ and the Kalman model \mathbf{H} .

We used Kalman filter for online decoding of the hand kinematics during feedback runs, starting each *snakerun* trial with zero initial conditions in the state and initial covariance matrix $\mathbf{P} = 10^{-9} \cdot \mathbf{Q}$.

4.2.6 Decoding performance and Kalman filter effect

A commonly used measure of similarity between actual and decoded movements is the Pearson's correlation coefficient, r . We evaluated r between real trajectories and decoder outputs, for each participant, metric (positions, velocities, accelerations), and condition (100%, 66%, 33% and 0% proportion of LeapMotion control). We considered *snakeruns4-5* for the 100%, *snakeruns6-7* for the 66%, *snakeruns8-9* for the 33%, and *snakeruns10-11* for the 0% LeapMotion condition. Both EEG and LeapMotion signals were processed as online, i.e. using causal filters and delaying the LeapMotion signal by 165ms (Figure 4.4, Figure 4.5).

Chance level correlations were evaluated through a shuffling approach. We broke the association between the EEG in \mathbf{X} and the relative kinematics in \mathbf{Y} by randomly shuffling \mathbf{Y} trials and fitting the decoder. We shuffled the data 100 times, evaluated the decoding correlations, and assessed chance level ($\alpha=5\%$) by taking the 95th percentile of the distribution.

To evaluate the effect of Kalman filter, we computed the decoding correlations in two cases: (i) using just the decoder (as in Equation 4.4) and (ii) using the decoder and the kalman gain. We compared the two methods across subjects for each metric and condition, by using Wilcoxon signed-rank tests, and controlled the false discovery rate (FDR) at significance level 0.05 by adjusting the p-values (Benjamini and Hochberg, 1995; Yekutieli and Benjamini, 1999).

To complete the analysis of the decoder output, we evaluated its amplitude and compared it to real movement. We finally explored the dependency across movement parameters, by means of cross-correlation curves in the [-1s, 1s] time range.

4.2.7 Pattern source mapping

We analyzed the decoder activation patterns at cortical level by means of EEG source imaging (Michel and Murray, 2012; Michel et al., 2004).

Activation patterns were computed from the decoder weight matrices according to (Haufe et al., 2014):

$$A = \widehat{\Sigma}_X \cdot W \cdot \widehat{\Sigma}_Y^{-1} \quad (4.12)$$

$\widehat{\Sigma}_X$ and $\widehat{\Sigma}_Y$ are the sample covariance matrices evaluated on calibration \mathbf{X} and \mathbf{Y} data. Analytical shrinkage regularization (Bartz and Müller, 2014) was applied to estimate $\widehat{\Sigma}_X$ and $\widehat{\Sigma}_Y$. In order to express the patterns as voltages (Ofner et al., 2017), we scaled

them by multiplying with the square root of $\widehat{\Sigma}_Y$. The procedure is equivalent to the one in (Kobler et al., 2018), but taking into account the dependency between Y variables.

Before projecting the scaled patterns to source space, we further normalized them to account for the variability in the EEG baseline magnitude across participants. As the scaled patterns reflect the potential on the scalp, we used chance level patterns to estimate the subject- and metrics-dependent baseline level of activity. For each participant and metric, we took the root mean square (across electrodes and lags) of the chance level activation patterns (in channel space). We averaged the values over the 100 chance level repetitions, and used the result for normalization.

The normalized patterns were mapped to source space using the open source software Brainstorm (Tadel et al., 2011), version 22-Aug-2018. We created head models co-registering the ICBM152 boundary element model (BEM)(Fonov et al., 2011) with the recorded electrode positions (ELPOS, Zebris Medical GmbH, Germany) of each subject. The BEM template consisted of three layers (cortex, skull, scalp), whose conductivities were set to (1, 0.008, 1). Electrode positions were registered to the scalp layer using three anatomical landmarks (nasion, left and right preauricular points). As participants slightly deviated from the template anatomy, we completed the registration by projecting the floating electrodes on the BEM scalp layer. The cortex was modelled with 5001 voxels. The forward model, describing the propagation of electrical fields from the cortex to the scalp, was computed with OpenMEEG (Gramfort et al., 2010; Kybic et al., 2005). We finally used sLORETA (Pascual-Marqui, 2002) to evaluate the corresponding inverse model, considering 3 unconstrained source components per voxel. The noise covariance matrix of the EEG, necessary for sLORETA, was estimated for each subject on the eye-corrected data of the *eyeruns*, applying analytical shrinkage regularization (Bartz and Müller, 2014). As a final step we computed, for each voxel, the norm of the three x, y, and z source components.

4.2.8 Source space statistics

For each movement parameter and time lag, we looked for significant activations in source space by computing the paired difference between each decoder pattern and the corresponding chance level activity (in source space). Chance level was computed by averaging the 100 back-projected normalized chance level patterns. As in (Kobler et al., 2018), we evaluated significance at eight region of interests (ROIs) associated with movement processing (Figure 4.6), namely the dorsomedial occipital cortex (DMOC), the superior parietal lobule (SPL), the primary sensorimotor (SM1) and fronto-central areas (FC) of both hemispheres. The activity of each ROI was computed by averaging its voxels. Significance was assessed by two-tailed non-parametric permutation paired t-tests (Maris and Oostenveld, 2007; Nichols and Holmes, 2001)

with 1000 repetitions. False discovery rate (FDR) was controlled by adjusting the p-values at 0.05 significance level (Yekutieli and Benjamini, 1999).

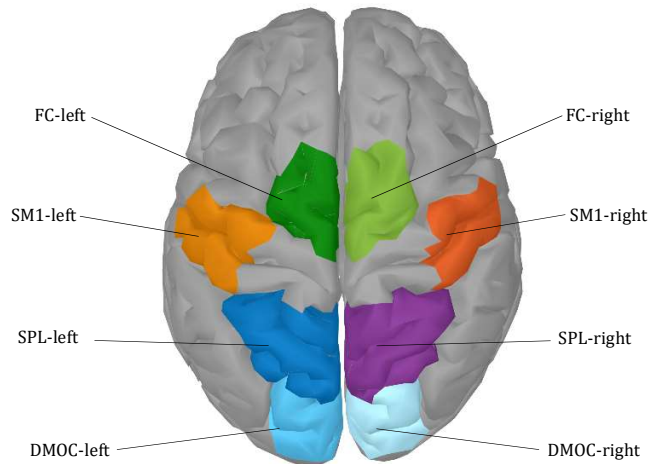


Figure 4.6. Visualization of the regions of interests (ROI)s, covering dorsomedial occipital cortex (DMOC), superior parietal lobule (SPL), primary sensorimotor areas (SM1) and fronto-central areas of both hemispheres.

4.3 Results

4.3.1 Decoder correlations

For each subject, metric, and condition, correlations between decoder output and real movement were always above chance level. The result was verified for both linear decoding alone and with Kalman.

In the case of Kalman filtering, the average correlations for the decoded positions were (0.47 ± 0.019 , 0.32 ± 0.022 , 0.28 ± 0.018 , 0.26 ± 0.031 , mean \pm SEM), respectively for the conditions of 100%, 66%, 33% and 0% LeapMotion control. The corresponding chance level correlations were (0.13 ± 0.0077 , 0.12 ± 0.0083 , 0.11 ± 0.0035 , 0.11 ± 0.0064). Correlations distributions for each metric and condition are detailed in Table 4.1, and summarized in Figure 4.7.

Table 4.1. Pearson's correlation coefficients between Kalman-decoded and real trajectories for each metric and condition (mean \pm SEM), and corresponding chance levels.

condition	output meas.	Metric					
		x pos	x vel	x acc	y pos	y vel	y acc
100% Leap	<i>r</i> dec + kalm	0,46 \pm 0,03	0,51 \pm 0,04	0,42 \pm 0,03	0,49 \pm 0,02	0,53 \pm 0,02	0,43 \pm 0,02
	<i>r</i> chance	0,13 \pm 0,03	0,14 \pm 0,03	0,11 \pm 0,02	0,14 \pm 0,04	0,16 \pm 0,04	0,12 \pm 0,03
66% Leap	<i>r</i> dec + kalm	0,31 \pm 0,03	0,40 \pm 0,04	0,32 \pm 0,03	0,33 \pm 0,03	0,41 \pm 0,03	0,32 \pm 0,02
	<i>r</i> chance	0,12 \pm 0,04	0,14 \pm 0,04	0,11 \pm 0,04	0,14 \pm 0,03	0,15 \pm 0,03	0,12 \pm 0,03
33% Leap	<i>r</i> dec + kalm	0,28 \pm 0,03	0,38 \pm 0,03	0,30 \pm 0,03	0,30 \pm 0,03	0,40 \pm 0,03	0,30 \pm 0,03
	<i>r</i> chance	0,12 \pm 0,01	0,13 \pm 0,03	0,10 \pm 0,03	0,12 \pm 0,02	0,14 \pm 0,02	0,11 \pm 0,03
0% Leap	<i>r</i> dec + kalm	0,24 \pm 0,05	0,33 \pm 0,06	0,27 \pm 0,05	0,29 \pm 0,04	0,39 \pm 0,04	0,30 \pm 0,04
	<i>r</i> chance	0,11 \pm 0,03	0,14 \pm 0,03	0,11 \pm 0,03	0,11 \pm 0,03	0,13 \pm 0,03	0,10 \pm 0,04

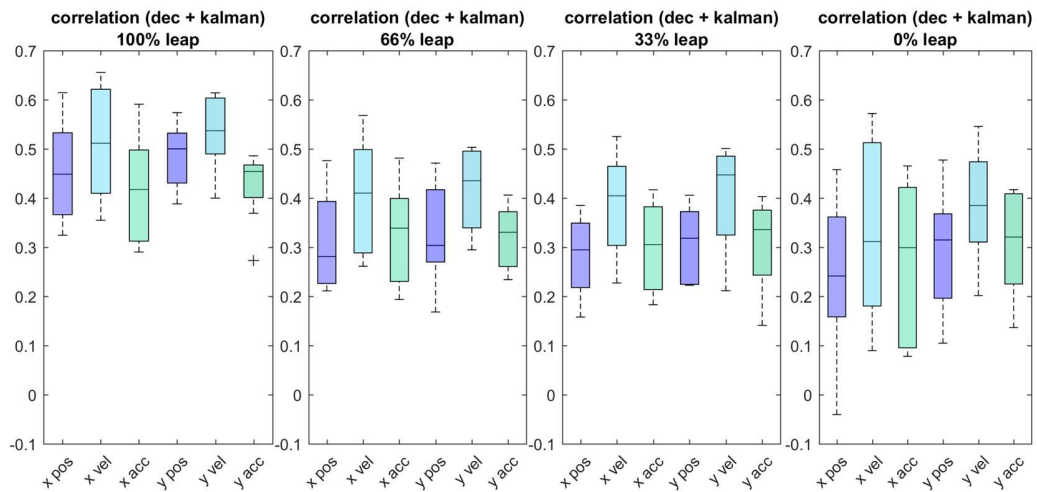


Figure 4.7. Box-plot showing the correlation distributions between Kalman-decoded and real trajectories, for each metric and condition.

4.3.2 Effect of the Kalman filter

To quantify the Kalman filter effect, we compared the correlations of each subject, metric and condition, in the two cases of linear decoder alone or together with Kalman filtering. The average increase in correlation with Kalman was 0.065. The increase was consistent over metrics and conditions (Table 4.2), and always significant ($\alpha = 5\%$) according to our tests (Wilcoxon signed-rank tests + FDR correction).

Table 4.2. Correlations r between real and decoded trajectories (mean \pm SEM). The table reports: i) correlations of linear decoder alone, ii) correlations of decoder + Kalman, iii) average increase between methods and iv) uncorrected p-values from the Wilcoxon signed-rank tests (FDR critical value = 0.0078).

condition	output meas.	Metric					
		x pos	x vel	x acc	y pos	y vel	y acc
100% Leap	r just dec	0,39 \pm 0,02	0,42 \pm 0,04	0,38 \pm 0,03	0,40 \pm 0,02	0,44 \pm 0,03	0,38 \pm 0,02
	r dec + kalm	0,46 \pm 0,03	0,51 \pm 0,04	0,42 \pm 0,03	0,49 \pm 0,02	0,53 \pm 0,02	0,43 \pm 0,02
	Δr kalm-dec	0,070 \pm 0,018	0,086 \pm 0,015	0,042 \pm 0,009	0,089 \pm 0,008	0,096 \pm 0,008	0,043 \pm 0,009
	p-value	0,0078	0,0039	0,0078	0,0039	0,0039	0,0039
66% Leap	r just dec	0,25 \pm 0,03	0,34 \pm 0,05	0,28 \pm 0,03	0,28 \pm 0,03	0,33 \pm 0,02	0,29 \pm 0,02
	r dec + kalm	0,31 \pm 0,03	0,40 \pm 0,04	0,32 \pm 0,03	0,33 \pm 0,03	0,41 \pm 0,03	0,32 \pm 0,02
	Δr kalm-dec	0,067 \pm 0,016	0,063 \pm 0,014	0,046 \pm 0,010	0,044 \pm 0,009	0,080 \pm 0,014	0,037 \pm 0,008
	p-value	0,0117	0,0039	0,0078	0,0039	0,0039	0,0039
33% Leap	r just dec	0,20 \pm 0,02	0,33 \pm 0,04	0,24 \pm 0,02	0,25 \pm 0,03	0,31 \pm 0,03	0,27 \pm 0,03
	r dec + kalm	0,28 \pm 0,03	0,38 \pm 0,03	0,30 \pm 0,03	0,30 \pm 0,03	0,40 \pm 0,03	0,30 \pm 0,03
	Δr kalm-dec	0,077 \pm 0,019	0,052 \pm 0,013	0,054 \pm 0,012	0,054 \pm 0,015	0,093 \pm 0,01	0,034 \pm 0,007
	p-value	0,0117	0,0039	0,0078	0,0117	0,0039	0,0039
0% Leap	r just dec	0,17 \pm 0,04	0,26 \pm 0,06	0,22 \pm 0,04	0,24 \pm 0,04	0,28 \pm 0,04	0,26 \pm 0,03
	r dec + kalm	0,24 \pm 0,05	0,33 \pm 0,06	0,27 \pm 0,05	0,29 \pm 0,04	0,39 \pm 0,04	0,30 \pm 0,04
	Δr kalm-dec	0,070 \pm 0,019	0,066 \pm 0,014	0,048 \pm 0,014	0,051 \pm 0,012	0,112 \pm 0,012	0,043 \pm 0,009
	p-value	0,0117	0,0039	0,0078	0,0078	0,0039	0,0039

Besides the average increase in correlation, Kalman filter also had a smoothing effect on the decoder output. Figure 4.8 displays an example of the real LeapMotion signal,

the linear decoder output, and the Kalman filter output (x and y dimensions). As evident from the figure, Kalman filtering removes the higher-frequency ripples from the decoded signal, maintaining it in approximately the same frequency range of the movement.

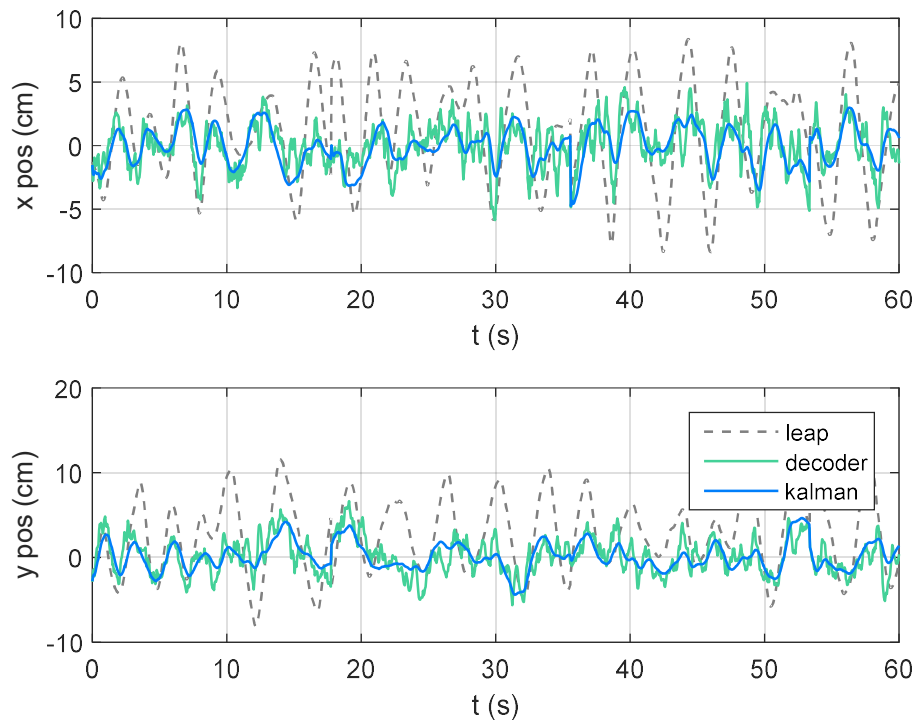


Figure 4.8. Example of real and decoded trajectories (participant p02).

4.3.3 Amplitude of the decoder output

To complete the analysis of the decoder output, we compared the amplitude of real and decoded movements across conditions. To quantify the movement amplitude, we took the difference between the 95th and the 5th percentiles of the position distributions. In Figure 4.9, we show the mean and standard deviations of the real and decoded signals' amplitudes across conditions. As from Figure 4.8, the amplitude of the decoded movement is generally smaller (~5-6cm) with respect to the LeapMotion signal (~15-20cm). In addition, while the participants' movement amplitude tended to increase over conditions, the amplitude of the decoded signals remained unaffected.

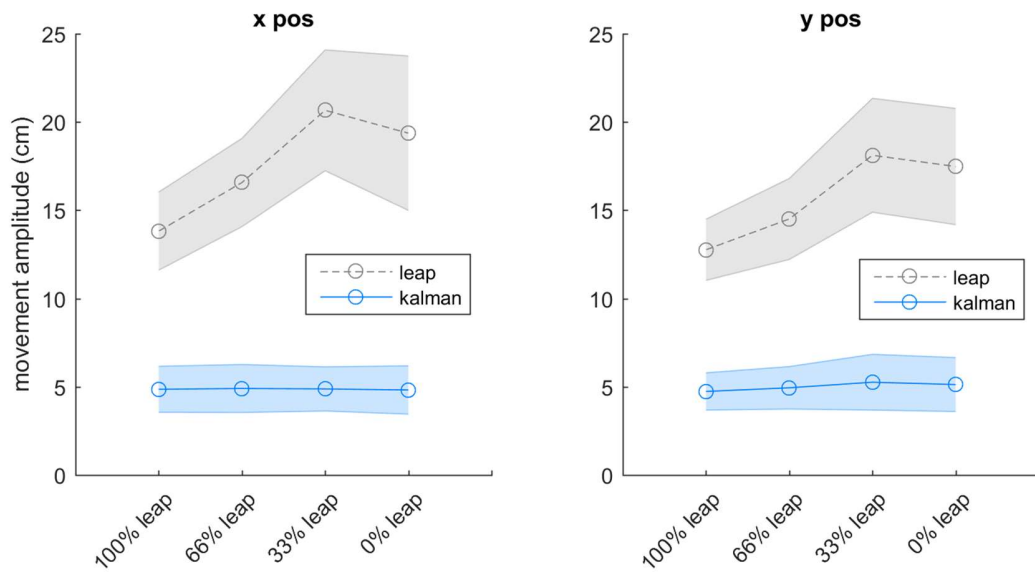


Figure 4.9. Trends of real and decoded trajectory amplitudes (cm) over the four conditions (mean and standard deviation across subjects).

4.3.4 Source space statistics

Source analysis revealed significant activations in the dorsomedial occipital (DMOC) and superior parietal lobule (SPL) areas for both the decoded velocities and accelerations, while no significant activations were found in the fronto-central (FC) and sensorimotor (SM) areas. Table 4.3 details the (uncorrected) p-values from the permutation tests, for each ROI, metric and time-lag. The results need to be interpreted according to the FDR correction critical value, $p_{crit} = 0.007$. Figure 4.10 summarizes the results of Table 4.3 at lag 0, by showing the magnitude of the normalized and scaled decoder activation patterns, averaged over participants.

metric	time lag	ROI							
		DMOC-right	DMOC-left	SPL-right	SPL-left	FC-right	FC-left	SM1-right	SM1-left
xpos	-0.30s	0.093	0.098	0.162	0.565	0.496	0.572	0.100	0.272
	-0.25s	0.246	0.130	0.303	0.712	0.344	0.468	0.095	0.257
	-0.20s	0.677	0.203	0.663	0.837	0.214	0.361	0.114	0.209
	-0.15s	0.946	0.310	0.901	0.877	0.159	0.246	0.112	0.194
	-0.10s	0.878	0.449	0.988	0.922	0.149	0.199	0.101	0.177
	-0.05s	0.782	0.613	0.998	0.960	0.191	0.198	0.089	0.210
	0s	0.783	0.725	0.913	0.951	0.361	0.258	0.079	0.236

x vel	-0.30s	0.099	0.554	0.030	0.107	0.100	0.631	0.151	0.554
	-0.25s	0.066	0.341	0.017	0.028	0.046	0.217	0.032	0.997
	-0.20s	0.037	0.204	0.005	0.007	0.038	0.103	0.019	0.631
	-0.15s	0.026	0.144	0.004	0.004	0.032	0.067	0.021	0.373
	-0.10s	0.006	0.099	0.004	0.004	0.028	0.059	0.030	0.203
	-0.05s	0.005	0.050	0.004	0.004	0.025	0.040	0.049	0.117
	0s	0.004	0.023	0.004	0.004	0.012	0.032	0.046	0.054
x acc	-0.30s	0.010	0.015	0.009	0.009	0.039	0.095	0.519	0.508
	-0.25s	0.004	0.012	0.004	0.009	0.040	0.104	0.804	0.685
	-0.20s	0.004	0.009	0.004	0.009	0.039	0.172	0.811	0.904
	-0.15s	0.004	0.004	0.004	0.009	0.117	0.294	0.543	0.989
	-0.10s	0.004	0.004	0.004	0.007	0.325	0.438	0.367	0.879
	-0.05s	0.004	0.004	0.004	0.010	0.332	0.541	0.398	0.701
	0s	0.006	0.009	0.004	0.053	0.136	0.376	0.681	0.875
y pos	-0.30s	0.6004	0.137	0.565	0.589	0.026	0.098	0.129	0.200
	-0.25s	0.6374	0.142	0.541	0.463	0.052	0.170	0.127	0.187
	-0.20s	0.761	0.182	0.570	0.377	0.136	0.335	0.113	0.258
	-0.15s	0.936	0.256	0.591	0.291	0.259	0.543	0.089	0.356
	-0.10s	0.979	0.313	0.655	0.232	0.391	0.769	0.059	0.512
	-0.05s	0.929	0.374	0.748	0.167	0.557	0.925	0.050	0.628
	0s	0.955	0.405	0.769	0.119	0.691	0.978	0.042	0.717
y vel	-0.30s	0.003	0.030	0.015	0.048	0.725	0.898	0.803	0.086
	-0.25s	0.004	0.022	0.010	0.024	0.968	0.974	0.977	0.177
	-0.20s	0.004	0.016	0.005	0.014	0.869	0.883	0.794	0.363
	-0.15s	0.008	0.012	0.005	0.010	0.748	0.813	0.661	0.591
	-0.10s	0.010	0.008	0.005	0.006	0.650	0.704	0.590	0.868
	-0.05s	0.007	0.008	0.002	0.006	0.550	0.577	0.550	0.831
	0s	0.006	0.006	0.002	0.006	0.420	0.473	0.550	0.568
y acc	-0.30s	0.054	0.007	0.110	0.002	0.342	0.213	0.820	0.725
	-0.25s	0.034	0.020	0.241	0.007	0.166	0.129	0.711	0.825
	-0.20s	0.011	0.041	0.305	0.012	0.121	0.095	0.733	0.670
	-0.15s	0.002	0.061	0.196	0.026	0.097	0.079	0.997	0.505
	-0.10s	0.016	0.078	0.113	0.057	0.081	0.091	0.696	0.479
	-0.05s	0.045	0.063	0.075	0.088	0.077	0.091	0.502	0.576
	0s	0.086	0.057	0.053	0.054	0.138	0.200	0.639	0.973

Table 4.3. Uncorrected p-values from the permutation tests, for each ROI, metric and time-lag (FDR critical value $p_{\text{crit}} = 0.007$). The significant activations are highlighted in light blue.

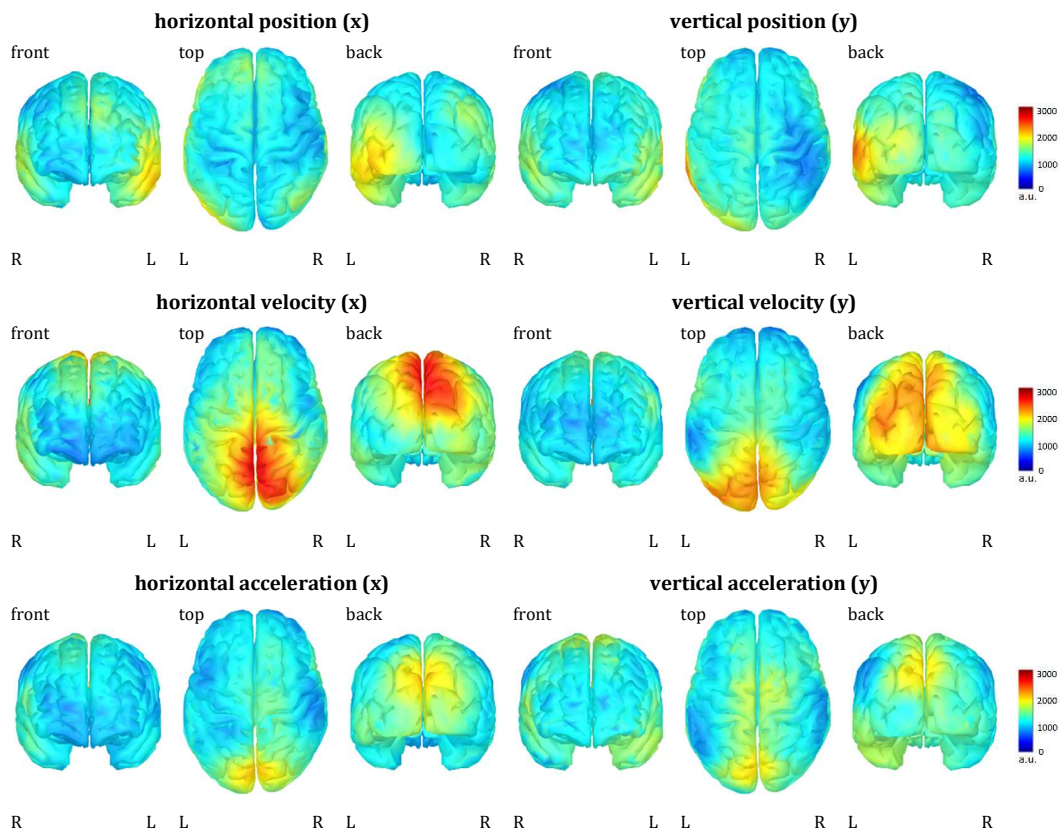


Figure 4.1. Grand average decoder patterns at lag 0 for the horizontal (left) and vertical (right) components, for the positions (upper panels), velocities (middle panels) and acceleration (lower panels). The voxel color indicates strength of activity.

4.3.5 Cross-correlation curves

This final section of results investigates the temporal dependency between the movement parameters employed to reveal the underlying correlations between decoder outputs. Figure 4.11 shows the cross-correlation curves between movement parameters in the $[-1\ 1]$ s time range for the x and y components (first and second row). The dependencies among variables (positions, velocities and accelerations) were very similar for the two components (Figure 4.11). Accelerations were anti-correlated with respect to the positions (left and right panels), and led the velocities by 0.55s (peak cross-correlations velocities-accelerations at -0.55s for both the x for the y component), which in turn led the positions by ~ 0.70 s (peak cross-correlations velocities-positions at +0.70s for the x , +0.75s for the y component). The peak correlations between x and y components were finally always below $r = 0.11$.

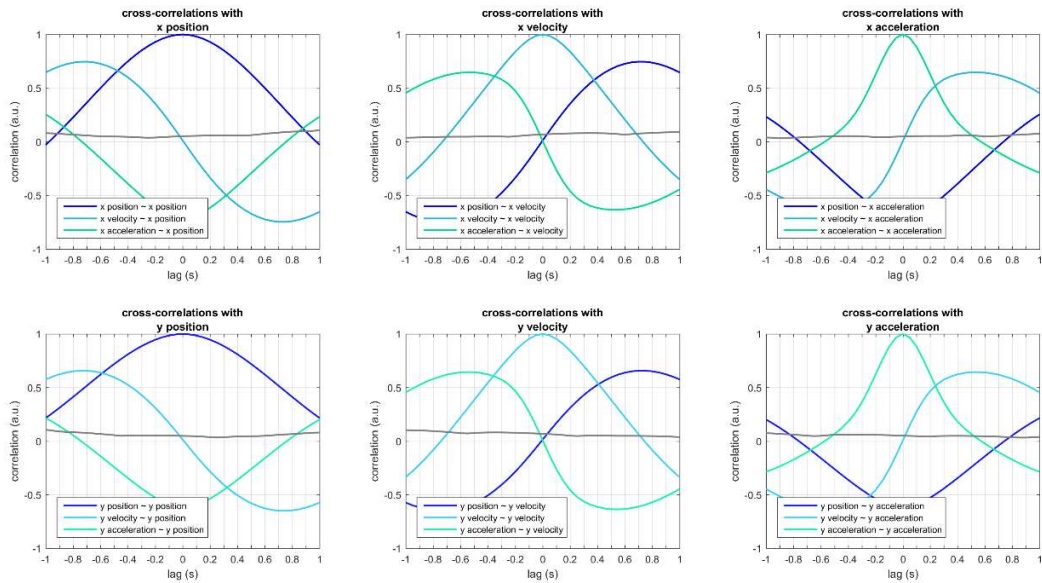


Figure 4.11. Cross-correlation curves between movement parameters (x and y component in the first and second row, respectively). In each row, cross-correlations are shown with respect to the positions (left panels), velocities (middle panels) and accelerations (right panels) of the same component, while the gray line displays the maximum correlation with the metrics of the other component.

4.4 Discussion

In this study, we investigated for the first time the feasibility of controlling an assistive robotic arm in real-time by means of continuously EEG-decoded movements. We developed the experimental tools and a paradigm for the purpose, using a Kinova JACO assistive robotic arm, and building on the results of previous studies. With the idea of introducing a smooth transition from the detection based on hand kinematics to the one relying on EEG signals, we opted for implementing a shared control framework for the control of the robot, progressively increasing the proportion of EEG-decoded movement, up to a final condition of 100% EEG-controlled robotic arm.

4.4.1 Decoding performance and Kalman filter effect

As a first result, the study is a proof-of-concept that continuous EEG decoding is still feasible in an online scenario, despite the differences between offline and online signal processing, and the additional delays introduced when closing the loop with robotic feedback. The correlations between real and EEG-decoded movements were always above chance level (Table 4.1), meaning that kinematic information could always be retrieved from the processed EEG signal. In the 100% kinematic control condition, the

online decoding correlations were also comparable with previous noninvasive offline studies, as (Lv et al., 2010; Úbeda et al., 2015).

One of the design aspects that required more attention when shifting from offline to online decoding was the tuning of the EEG filter parameters. Indeed, we made a trade-off between the desired characteristics (e.g. precise bandwidth and effective stopband attenuation) and the introduced group delay/phase distortion. On one hand, a limited group delay was necessary to provide timely and smooth feedback. On the other hand, a limited phase distortion was important to avoid an excessive spread of the EEG signal over time, keeping altogether the EEG components carrying the same movement information. Considering these design constraints, we needed to modify the filter from the previous offline study in (Kobler et al., 2018), by relaxing the parameters of both the high-pass and the low-pass part of the filter. Regarding the high-pass, we reduced the filter order from eight to one, and changed the cut-off frequency from 0.25Hz to 0.18Hz. For the low-pass, we reduced the filter order from four to two, and increased the cut-off frequency from 0.8Hz to 1.5Hz. The overall effect was an increase of the filtered bandwidth from 0.25-0.8Hz to 0.18-1.5Hz, together with a drastic decrease of stopband attenuation. This resulted in a filtered EEG signal with higher frequency components than the real trajectories, which instead had a frequency content approximately below 0.8Hz.

One element of design with a beneficial effect on the decoder output was the introduction of Kalman filtering. Besides the significant increase in correlation with respect to linear decoding alone (Table 4.2), Kalman filtering had a clear smoothing effect (Figure 4.8). This brought the decoded trajectories back to similar frequency spectrum as the one of the real movement, despite the higher frequency jitters introduced by the blander filtering. The idea of Kalman filtering had already been introduced in previous decoding studies, either based on intracortical recordings (Black et al., 2003; Li et al., 2009; Mulliken et al., 2008) or on electrocorticography (Pistohl et al., 2008). In this work, we proposed a possible application for EEG signal decoding. The solution builds up on PLS linear regression models (Kobler et al., 2018; Ofner and Müller-Putz, 2015) and features dimensionality reduction, beneficial in the cases of highly collinear data, as the multichannel EEG signal over multiple time lags. For these properties, the proposed implementation would be suitable also in the cases of magnetoencephalographic and electrocorticographic recordings, although it might be easily extendible to every case positions, velocities and accelerations are extracted from neural data during movement.

4.4.2 Amplitude of the decoder output

One aspect of the decoder output not encompassed by the Pearson's correlation coefficient is the amplitude of the decoded signal with respect to the real hand trajectories. However, as already observed in the previous study of (Kobler et al.,

2018), while the direction of the hand movement could be inferred from the EEG, the amplitude of the decoder output was generally smaller than the real trajectory. The very same effect was present in this study, and can be observed both in the sample decoded trajectories of Figure 4.8, and in the amplitude trends of real and decoded movements (Figure 4.9). When specifically observing Figure 4.9, we can see that the amplitude of the decoded trajectories did not change over conditions, while the participants tended to enlarge their movements with increasing proportion of EEG control. The effect is probably a form of compensation to the smaller decoded trajectories. The enlarging tendency stopped in the final part of the experiment, possibly as the behavior did not produce an effect on the decoder amplitude (Figure 4.9).

One conclusion that may be drawn from these results is that the amplitude of the movement seems not to be well encoded in the EEG signals. This is in agreement with the previous EEG study of (Kobler et al., 2018), although in disagreement with the intracortical recordings in (Paninski et al., 2004). Specifically in (Paninski et al., 2004), a linear speed scaling was found in the activity of velocity-tuned neurons, together with a linear distance scaling for position-tuned neurons. Shifting from invasive intracortical to noninvasive EEG recordings, it is possible that the scaling information is dampened and lost, or that it cannot be effectively retrieved with a PLS linear decoding model. If the signal information is affected by noise, it is indeed possible that PLS regression limits the amplitude of the decoder output, as a consequence of minimizing the errors due to overshooting. One way to overcome this limitation may be introducing a subject-specific gain after the decoder, so that the final amplitude is in the same range of the hand trajectory.

4.4.3 Source space analysis: tuning of neural activity to the velocities

When projecting the averaged decoder patterns to source space, we found significant activations of the parieto-occipital areas (SPL and DMOC areas of both hemispheres) for the velocities and the accelerations over multiple time lags (Table 4.3, Figure 4.10). The velocity results are in agreement with the previous offline study of (Kobler et al., 2018) (Figure 4.10), while the significant acceleration tuning would be a new result with respect to literature. Even though previous studies (Carmena et al., 2003) highlighted neural tuning to gripping force/muscular activity (EMG), possibly related to acceleration, caution should be taken when interpreting these results. The three kinematic variables (positions, velocities, accelerations) are indeed correlated in time, as inferable when looking at the cross-correlation curves in Figure 4.11. The accelerations lead the velocities by 550ms, and the correlation between the variables in the -300-0s time-range is still high (Figure 4.11, middle panels). As a further indication, the acceleration activation patterns are very similar to the velocity patterns at lag 0 (Figure 4.10) and, even more, this could be observed at previous lags (not

shown). Additionally, the significantly active ROIs are the same for the two variables (Table 4.3), with just slight time shifts.

From these premises, it is likely that the significant effect observed for the accelerations is of the same nature as the velocity effect. The fact that the two variables are highly correlated actually hinders the interpretation of their effects. Nevertheless, a consistent body of literature indicates neural tuning to the velocities (Bradberry et al., 2010; Carmena et al., 2003; Kobler et al., 2018; Mehring et al., 2003; Paninski et al., 2004; Schalk et al., 2007; Waldert et al., 2009) and, in addition, velocities were the ones with overall highest correlations among our six decoded variables (Figure 4.7, Table 4.1). To sum up, although it cannot be excluded that an effect exists also for the accelerations, our results suggest that the velocity is the kinematic variable best encoded in the EEG signals, corroborating the previous findings reported in (Kobler et al., 2018).

One difference between our results and (Kobler et al., 2018; Paninski et al., 2004) is the timing of the velocity tuning curve, leading the movement by 100-150ms in the case of (Kobler et al., 2018; Paninski et al., 2004) and here most prominent at lag 0. However, we believe that the different type of processing, from offline to online, could explain the difference. Although limited, the phase distortion introduced by the first order high-pass filter may have delayed the lowest frequency components more with respect to the average group delay of 250ms used for synchronization (Figure 4.5). This may have led to a spread of information over time and subsequently to a suboptimal alignment, shifting the tuning peak with respect to offline studies.

4.4.4 Activation of the parieto-occipital areas, and efficacy of the eye artifact correction algorithm

One of the questions that may arise when looking at the activation patterns in source space is why the significant ROIs span parieto-occipital areas, while significant activations are not found in the hand area in the motor cortex.

On the one hand, previous monkey and human studies showed that not only the motor areas but also the parietal cortex participates in voluntary upper-limb movements (Bradberry et al., 2010; Carmena et al., 2003; Culham and Valyear, 2006; Filimon et al., 2007, 2009; Kalaska et al., 1983; Kobler et al., 2018; Lebedev et al., 2005; Mulliken et al., 2008). The intracortical recordings of (Kalaska et al., 1983) even found in the superior parietal lobule the same directional tuning as in primary motor cortex neurons (Georgopoulos et al., 1982). Another aspect that should be considered is that we allowed for natural eye movements during tracking. This allows us to classify our task as a general visuomotor task, broadly related to the anterior (proprioception) and posterior (proprioception + visual processing) areas of the parieto-occipital cortex (Filimon et al., 2009).

On the other hand, the absence of significant activations in the primary motor areas may be explained as follows. In their previous offline study, (Kobler et al., 2018) contrasted two conditions of a pursuit-tracking task: i) in the first condition, the participant was asked to follow a target on the screen with both its gaze and controlling a cursor through the hand, while ii) in the second, tracking was requested just with the gaze. When looking at the visuomotor task, significant activations were found in the parieto-occipital cortex, although not in the motor areas. However, when contrasting the activation patterns of the two conditions, a significant activation in SM1 was finally revealed. As already concluded in the previous study (Kobler et al., 2018), the presence of saccadic eye movements may mask the activation in the motor areas, as the combination of proprioception and visual processing is visible more in the parieto-occipital areas. Nevertheless, an activation of the motor areas is probably present as well, similarly to the results in (Kobler et al., 2018) when contrasting between conditions.

Even though masking the activation of the motor areas, the presence of saccadic movements should not be considered as an artifact. The presence of brain activity related to visual processing is indeed different from extra-brain sources, like in this example the EOG-induced artifacts. The efficacy of the implemented EOG artifact removal algorithm (Kobler et al., 2017) is visible in Figure 4.10: if residual EOG activity had been present, this would have been visible in the frontal and temporal areas. The absence of such activity guarantees the efficient data cleaning operated by the algorithm (Kobler et al., 2017), with the additional benefit of permitting our study to be carried out in a more ecologically valid setup.

4.4.5 Feedback effect and adaptation

One final observation that might be driven from our results regards the tendency of decoder correlations over time. Even though the hand trajectories could always be decoded above chance level (Table 4.1), a general decrease of correlation was observed with increasing proportions of EEG control (Figure 4.7).

The fall may be due to the gradual loss of control perceived by the user, when shifting to the brain operation mode. Besides inducing a change in the participant's mental condition, the control strategy of participants may also have changed. To give an example, participants might have paid more attention to the proprioception, to the robot, or to the snake, with respect to the calibration condition. An analogous effect was shown in a previous monkey study (Lebedev et al., 2005), allowing the animals to control a robotic end effector through their invasively recorded brain activity. As the monkeys started to use their brain activity to control the robot, the activity of neuron populations became less representative of the monkey's hand movement, starting to represent more the movement of the actuator (Lebedev et al., 2005). Given the change of internal and external conditions when switching from kinematic to brain control,

we believe an adaptation of the decoder parameters will be required in future studies, taking also into account a possible learning effect when training over multiple days (Carmena et al., 2003; Lebedev et al., 2005).

4.5 Limitations

One of the main limitations of this study is the presence of residual movement artifacts, visible to the left side of the brain in the position activation patterns (Figure 4.10). The reason why this artifact is visible on the opposite side of the moving arm is explained in the following lines.

After calibration, we always checked the decoder activation patterns (in channel space), interpolating the electrodes with suspicious artifactual activity. This is the reason why we often interpolated the most external electrodes to the right, posterior side (see Table 4.S1, Supplementary Material), assuming that movement artifacts would have arisen near the shoulder, on the same side of moving arm. One effect that we did not consider was that participants naturally tended to make subtle head movements, to adjust their balance as a reaction to the shoulder. These subtle adjustments caused very little movement artifacts on both sides. However, as we did not systematically interpolate left side electrodes, subtle residual artifacts are present on this side, in the position decoder patterns (Figure 4.10).

One way to overcome this limitation is conducting the next studies with smaller arm movements, e.g. by setting 1:2 mapping from the hand to robot movement.

4.6 Conclusion

In this study, we developed for the first time the experimental tools and a paradigm to allow for real-time continuous control of a robotic arm by means on noninvasively EEG-decoded movements. The work detailed the methods used for this purpose, depicted some differences and constraints arising when shifting from offline to online decoding, and highlighted some points of design that have been beneficial for the setup, like the eye artifact removal algorithm and the Kalman filter.

The study corroborates previous findings of offline decoding studies, despite the differences introduced by online signal processing and the additional delays when closing the loop with a robotic arm. The kinematics of the hand could be decoded above chance level for all the subjects and conditions, proving that EEG decoding is feasible in a close-loop, online scenario, even in the case of 100% EEG control. Altogether, the study takes a first step in the field of real-time continuous noninvasive EEG decoding for robotic control. Future challenges, such as the minimization of the calibration time needed for the decoder, or the influence of reinforcement learning on the subjects over multiple recordings sessions, can lead to more intuitive control of neuroprosthesis or robotic devices.

4.7 Supplementary Material

Table 1.S1 Interpolated channels for each participant, selected by visual inspection of calibration data.

participant	bad channels
p01	AF7, AF8, FT10, TP9, TP8, TP10, P7, P8, PO9, PO8, PO10, O2
p02	FT10, T7, T8, TP9, TP7, CP5, TP8, TP10, P8, PO10
p03	FT10, T8, TP9, TP7, TP10
p04	AF4, AF8, F8, FT10, C6, T8, TP8, TP10, P8, PO8, PO10
p05	AF7, FT9, FT10, Cz, TP9, TP10, P7, PO9, PO7, PO10
p06	FPz, AF3, F8, FT8, TP9, TP8, TP10, PO9
p07	F8, FT7, FT8, FT10, CP6, TP10
p08	FT10, TP10, P6, PO7
p09	FT9, FT7, FT10, T7, C2, TP9, CP6, TP8, TP10, P8, PO8, PO10, O2
p10	AF4, FT8, FT10, T8, TP10, PO10

Chapter 5. Two simple but effective ways to improve SSVEP recognition based on Canonical Correlation Analysis

5.1 Introduction

Among the possible control signals suitable for EEG-based BCIs, steady-state visually evoked potentials (SSVEPs) are appealing for their high signal-to-noise ratio even without user training (Zhu et al., 2010). The consequent possibility to implement “plug-and-play” yet fast and highly accurate BCI systems, has been attracting over the years increasing attention (Allison et al., 2008; Wang et al., 2006).

SSVEPs are periodic brain signals elicited over the occipital cortex by visual stimulations with frequencies higher than 6Hz (Lin et al., 2007). In case different flickering objects (LEDs, symbols, squares) are simultaneously presented, an analysis of the SSVEP spectral content permits to reconstruct which stimulus the user is focusing on.

Traditionally used methods perform SSVEP recognition based on power spectral density analysis (PSDA) (Lin et al., 2007). In PSDA-based approaches, spectral powers are estimated from the EEG signal at the target stimulation frequencies and used as a feature for classification (Cheng et al., 2002; Müller-Putz et al., 2005; Yijun et al., 2005). However, PSDA-based methods can suffer from noise sensitivity if few channels are recorded, besides requiring relatively long signal portions (e.g. > 3s) to estimate the spectrum with a sufficient frequency resolution (Zhang et al., 2011, 2013, 2015). A promising and increasingly used approach, which has recently been raising the interest of research (Bin et al., 2009; Pan et al., 2011; Zhang et al., 2012), is the one based on Canonical Correlation Analysis (CCA) (Lin et al., 2007).

CCA is a multivariate statistical method able to reveal the underlying correlation between two sets of data (Hotelling, 1936). In the field of SSVEP recognition, CCA is performed several times between the considered EEG segment and a set of sine-cosine reference signals modeling the pure SSVEP responses to each stimulation frequency (Lin et al., 2007). The frequency response showing highest correlation with the analyzed EEG portion is finally recognized as the observed one.

The efficacy of the CCA approach has been widely proved by several studies, and its superiority to PSDA in terms of speed, accuracy and computational load has been shown (Hakvoort et al., 2011; Wei et al., 2011). For this reason, several CCA variations have been proposed over the years (Chen et al., 2015; Islam et al., 2016; Nakanishi et al., 2014; Pan et al., 2011; Wang et al., 2014; Yuan et al., 2015; Zhang et al., 2011, 2013, 2015, 2014). Most approaches, as the ones in (Pan et al., 2011; Wang et al., 2014; Zhang et al., 2011, 2013, 2015, 2014), concentrated on modifying the reference signals of SSVEPs by including subject-specific characteristics taken from the EEG activity of each user. The work in (Yuan et al., 2015) tried to enrich the algorithm with incorporating inter-subject information extracted from the signals of multiple subjects. In (Nakanishi et al., 2014), an effort was made towards compensating the natural decrease in signal-to-noise ratio of SSVEPs at higher stimulation frequencies, by correcting the gains for classification based on the shape of individual background EEG. Finally, in (Chen et al., 2015; Islam et al., 2016), CCA was repeated multiple times for each stimulation frequency, each time after passing the signal through a different IIR band-pass filter, to combine different aspects of the same EEG response.

Even though every introduced variation produced a significant increment of classification accuracy, all of them tended to increase the complexity of the algorithm, either by incorporating information from individual EEG data (as in (Pan et al., 2011; Wang et al., 2014; Zhang et al., 2011, 2013, 2015, 2014)), which requires the introduction of an additional user training, or by increasing computational load, e.g. in (Chen et al., 2015; Islam et al., 2016), where multiple CCAs are performed to assess each stimulation frequency. However, we believe that even taking the simple procedures and keeping low computational costs may be relevant, especially to favor the spread of low-cost and high-portability devices. For these reasons, this work presents two simple variations based on the classical CCA method. The variations regard: i) the number of correlations considered for classification and ii) the pre-processing of the signals. Nevertheless, we show that both modifications can significantly improve classification accuracy, with still leaving the whole procedure training-free and with no (variation i)) or minimal (variation ii)) impact on the number of steps required for each SSVEP identification.

5.2 Methods

5.2.1 The standard CCA method for SSVEP recognition

Canonical correlation analysis (CCA) is a multivariate statistical method (Hotelling, 1936) used to reveal the underlying correlation between two sets of data. Given two sets of random variables $\mathbf{X} \in \mathbb{R}^{I_1 \times J}$ and $\mathbf{Y} \in \mathbb{R}^{I_2 \times J}$, CCA finds the two corresponding

sets $\mathbf{U}=\mathbf{A}\mathbf{X} \in \mathbb{R}^{I_1 \times J}$ and $\mathbf{V}=\mathbf{B}\mathbf{Y} \in \mathbb{R}^{I_2 \times J}$ (linear combination of the original ones through $\mathbf{A} \in \mathbb{R}^{I_1}$ and $\mathbf{B} \in \mathbb{R}^{I_2}$), called *canonical variables*, so that the correlation between each pair or rows (U_i, V_i) is maximized:

$$\rho_i = \max \frac{cov(U_i, V_i)}{\sqrt{var(U_i)var(V_i)}} = \max_{A, B} \frac{cov(AX_i, BY_i)}{\sqrt{var(AX_i)var(BY_i)}} \quad (5.1)$$

with leaving (U_i, V_j) , (U_i, U_j) and (V_i, V_j) uncorrelated if $i \neq j$. Each CCA leads to a number of solutions ρ_i equal to the minimum between the number of rows in \mathbf{A} (I_1) and \mathbf{B} (I_2). The solutions ρ_i , sorted in descending order, are called *canonical correlations* and are a measure of the similarity between the two sets of original data.

The use of CCA in the field of SSVEP recognition was first proposed by Lin et al. in (Lin et al., 2007). Given K stimulation frequencies to be distinguished, CCA is performed K times – one for each stimulation frequency f_k - between the multichannel EEG signal in $\mathbf{X} \in \mathbb{R}^{N_{ch} \times J}$ (N_{ch} acquired channels, J time samples) and a set of sine-cosine reference signals in $\mathbf{Y}_k \in \mathbb{R}^{2N_{harm} \times J}$ modeling the pure SSVEP responses. Each set \mathbf{Y}_k is composed as follows:

$$\mathbf{Y}_k = \begin{pmatrix} \cos(2\pi f_k t) \\ \sin(2\pi f_k t) \\ \cos(2\pi 2f_k t) \\ \sin(2\pi 2f_k t) \\ \vdots \\ \cos(2\pi N_{harm} f_k t) \\ \sin(2\pi N_{harm} f_k t) \end{pmatrix}, \quad t = \frac{1}{F_s}, \frac{2}{F_s}, \dots, \frac{J}{F_s} \quad (5.2)$$

where f_k is the stimulation frequency, F_s is the sampling rate and N_{harm} is the number of harmonics included in the analysis.

Every CCA generates a vector of canonical correlations $(\rho_{k1}, \rho_{k2}, \dots, \rho_{k \min(N_{ch}, 2N_{harm})})$, of which only the first and largest one, ρ_{k1} , is used as a feature for classification. The analyzed EEG segment in \mathbf{X} is indeed assigned to the stimulation frequency leading to the maximum correlation ρ_{k1} :

$$f_{target} = \max_{f_k} \rho_{k1} \quad (5.3)$$

5.2.2 Variation 1: number of considered canonical correlations

Although the efficacy of the CCA method for SSVEP recognition has been widely proved (Bin et al., 2009; Zhang et al., 2012), and many variations have been proposed (Chang and Park, 2013; Chen et al., 2015; Islam et al., 2016; Nakanishi et al., 2014; Pan et al.,

2011; Wang et al., 2014; Yuan et al., 2015; Zhang et al., 2011, 2013, 2015, 2014), the majority of approaches consider only the first canonical correlation as a feature for classification. Nevertheless, as already noted by Lin et al. (Lin et al., 2007), since real EEG signals may be contaminated by noise and show phase transitions, the information might be spread over more than one correlation coefficient.

As a first variation of the algorithm, we evaluated the impact of taking more than one correlation coefficient as a feature for classification. Since the canonical variables in \mathbf{U} and \mathbf{V} are estimated so that each couple (U_i, U_j) and (V_i, V_j) are uncorrelated for $i \neq j$, and the sine-cosine waves in the reference signals \mathbf{Y}_k are orthogonal between each other, the information contained in each set of canonical variables will always be in quadrature with respect to the others. For this reason, we propose to combine the N_{corr} considered correlations with using the Euclidean norm:

$$r_k = \sqrt{\sum_{i=1}^{N_{corr}} \rho_{ki}^2} \quad (5.4)$$

The resulting combination r_k would be used as a feature for classification, in place of the largest canonical correlation ρ_{k1} only. The number N_{corr} can range from 1 to the minimum between N_{ch} and $2N_{harm}$, with N_{ch} number of acquired channels and N_{harm} number of considered harmonics. In this work, we employed $N_{ch}=8$ EEG channels (see section 5.2.4 for details) and $N_{harm}=3$ harmonics, so we explored the impact of taking all the possible numbers of considered correlations between 1 and $2N_{harm}$.

5.2.3 Variation 2: pre-processing with sinc-windowing

Another possible variation with respect to literature may consist in adding a pre-processing step to the EEG segments before performing CCA. If we exclude the works in (Chen et al., 2015; Islam et al., 2016), employing IIR filter banks, CCA is indeed typically applied without any pre-filtering of the EEG signals. Nevertheless, we believe that a narrow-band pre-filtering step around the K employed stimulation frequencies and their N_{harm} harmonics might be useful to increase the signal-to-noise ratio, expectantly enhancing classification accuracy.

As a second variation, we evaluated the influence of such type of pre-filtering with using a sinc-windowing implementation. The technique of sinc-windowing consists in the convolution of the analyzed signal with an adequately modulated sinc function. As it is known, the inverse Fourier transform of an ideal rectangular band-pass filter, centered in f_0 and with M bandwidth is:

$$\text{rect}\left(\frac{f-f_0}{M}\right) + \text{rect}\left(\frac{f+f_0}{M}\right) \xrightarrow{F^{-1}} 2M\text{sinc}(Mt)\cos(2\pi f_0 t) \quad (5.5)$$

where f is the frequency and F^{-1} is the inverse Fourier transform. Thus, the filtering around the f_k stimulation frequencies and N_{harm} harmonics can be accomplished by means of a convolution with the following function:

$$h(t) = 2M\text{sinc}(Mt) \left(\sum_{k=1}^K \sum_{n=1}^{N_{harm}} \cos(2\pi n f_k t) \right) \quad (5.6)$$

where M is the bandwidth (in this work, $M=1\text{Hz}$), N_{harm} is the number of harmonics, and f_k are the K stimulation frequencies.

Data acquisition

The EEG was recorded from 8 electrodes (PO7, PO8, PO3, PO4, O1, O2, POz, Oz), positioned according to the international 10-20 layout. The signals were acquired with a 256Hz sample frequency and a 50Hz notch filter on, by means of Brainbox EEG-1166 amplifier (Braintronix).

SSVEP stimulation was provided through four blue LEDs, arranged around a PC monitor. Each LED flickered at a different stimulation frequency ($f_1=8\text{Hz}$, $f_2=9\text{Hz}$, $f_3=10\text{Hz}$ and $f_4=11\text{Hz}$). The four stimulation frequencies were selected before the beginning of the study and were the same for all subjects. All stimulations were provided with a 50 percent duty-cycle. The behavior of the LEDs was controlled by a LabVIEW-Arduino interface.

5.2.5 Experimental paradigm

Ten healthy volunteers (aged 22 to 26, 4 males and 6 females) participated in the study. All of them had normal, or corrected to, normal vision. During the experiment, the participants sat on a comfortable chair, with their arms relaxed and their head still, approximately 60cm distant from the PC monitor.

The experiment was organized into runs, and the runs into trials. Each participant underwent a total of 4 runs, each comprising 16 trials. Each trial consisted in three subsequent phases: a 1s *preamble*, a 12s *stimulation*, and a 2s *break* period. During the *preamble*, a yellow square appeared on the screen indicating the target LED, then all LEDs started simultaneously flickering during *stimulation*, and the trial ended with a *break* period where the LEDs shut off and the square disappeared. The order of the target LEDs was randomized and counterbalanced in each run, so that each LED was

gazed for the same amount of time. To summarize, each experiment included a total of 4 runs x 16 trials x 12 seconds = 768 seconds of stimulation, i.e. 192 seconds for each class.

5.2.6 Performance evaluation

For each subject, we evaluated the average classification accuracy at the end of each run. To highlight the impact of the two proposed variations (composition of the feature vector and sinc-windowing), all accuracies were recomputed with using all the possible combinations of methods, i.e. a number of considered correlations from one to $N_{corr}=6$, with or without sinc-windowing. To evaluate the influence of considering different lengths of EEG signal for SSVEP recognition, all accuracies were recomputed with considering signal portions ranging from 0.5s to 5s, although the detailed results of statistical tests will be reported only in the case of a 1.5s window length.

5.2.7 Statistical analyses

As first, we compared each accuracy to chance level. The value of chance level was obtained by running the simulations as described in (Mueller-Putz et al., 2008) in the case of a 4-class BCI and taking the upper bound of the confidence interval at $\alpha=1\%$ significance, as an analytical expression of chance level was not available for the multi-class case. As concerns statistical comparison between methods, we had to account for the fact that multiple data came from the same subject, i.e. the samples could not be assumed to be completely independent. For this reason, instead of using paired-samples t-test to compare each method against the others, we ran all evaluations as post-hoc tests of a repeated measures ANOVA. The ANOVA design included both the factors “method” (the within-subject factor) and “subject”, thus taking into consideration all dependencies among data. Post-hoc tests were carried out with using Bonferroni correction. The use of parametric statistical tests was justified by the normality of data distributions, as confirmed by the application of a preliminary Kolmogorov-Smirnov test.

5.3 Results

The classification accuracies of each subject, run and method are detailed in Table 5.1 and summarized in Figure 5.1. The last two rows of Table 5.1 indicate the average and peak increment of each method with respect to standard CCA (first column). All the obtained accuracies were significantly higher than chance, as the upper bound of the confidence interval for chance level (with a significance of $\alpha=1\%$) in this particular setup was 30.27%. In Table 5.2, the results of the post-hoc comparisons (Bonferroni corrected) between each pair of methods are reported. In Figure 5.2, the accuracy

curves of all the considered methods, evaluated with different windows-lengths, are shown.

Table 5.1: Detailed accuracies (for each subject and run) for all combinations of methods, with a window length of 1.5s. The last rows of the table summarize the average and peak accuracy of each combination, together with the average and peak increment with respect to classical CCA.

		CCA (1 corr)	CCA (2 corr)	CCA (3 corr)	CCA (4 corr)	CCA (5 corr)	CCA (6 corr)	CCA (1 corr) + sw	CCA (2 corr) + sw	CCA (3 corr) + sw	CCA (4 corr) + sw	CCA (5 corr) + sw	CCA (6 corr) + sw
S01	<i>run 1</i>	92.2	96.1	96.1	96.9	96.9	96.9	91.4	93.8	95.3	95.3	96.1	96.1
	<i>run 2</i>	92.2	93.8	95.3	95.3	95.3	96.1	89.8	93.8	92.2	93.0	93.0	93.0
	<i>run 3</i>	95.3	96.1	96.1	96.9	96.1	96.1	95.3	97.7	96.1	96.1	96.1	94.5
	<i>run 4</i>	94.5	96.1	95.3	95.3	95.3	95.3	89.8	94.5	93.0	91.4	92.2	92.2
S02	<i>run 1</i>	85.2	87.5	90.6	90.6	90.6	90.6	85.2	91.4	90.6	90.6	91.4	91.4
	<i>run 2</i>	78.9	79.7	79.7	78.9	78.9	78.9	80.5	85.2	87.5	85.2	84.4	84.4
	<i>run 3</i>	82.8	85.2	85.2	87.5	86.7	86.7	87.5	90.6	92.2	93.0	92.2	92.2
	<i>run 4</i>	88.3	89.8	89.8	90.6	90.6	90.6	87.5	90.6	88.3	91.4	92.2	93.0
S03	<i>run 1</i>	80.5	87.5	86.7	88.3	88.3	88.3	80.5	78.1	79.7	78.9	78.9	77.3
	<i>run 2</i>	78.9	82.0	82.0	82.0	82.0	82.0	80.5	77.3	75.8	75.8	75.0	75.0
	<i>run 3</i>	74.2	79.7	82.0	82.8	82.8	82.8	71.9	74.2	78.1	78.9	78.9	78.1
	<i>run 4</i>	82.8	85.9	86.7	87.5	87.5	87.5	83.6	88.3	87.5	85.2	85.2	85.9
S04	<i>run 1</i>	75.8	79.7	82.0	82.8	82.0	82.8	85.9	85.9	85.2	85.9	86.7	85.9
	<i>run 2</i>	64.8	68.8	70.3	70.3	71.9	71.9	79.7	80.5	81.3	82.0	82.8	83.6
	<i>run 3</i>	69.5	73.4	73.4	72.7	74.2	75.8	78.9	83.6	84.4	86.7	84.4	84.4
	<i>run 4</i>	68.0	66.4	71.1	70.3	70.3	71.1	83.6	83.6	84.4	85.2	82.8	82.0
S05	<i>run 1</i>	64.1	68.0	72.7	74.2	74.2	74.2	73.4	79.7	82.0	82.8	84.4	83.6
	<i>run 2</i>	76.6	78.9	79.7	79.7	79.7	79.7	74.2	81.3	82.8	87.5	86.7	87.5
	<i>run 3</i>	61.7	66.4	66.4	67.2	68.0	68.0	63.3	66.4	71.9	72.7	75.0	75.8
	<i>run 4</i>	69.5	75.8	78.1	78.9	78.9	78.9	81.3	77.3	80.5	82.8	82.8	82.0
S06	<i>run 1</i>	60.9	66.4	66.4	67.2	67.2	68.0	64.1	63.3	64.8	69.5	71.1	72.7
	<i>run 2</i>	64.1	60.9	61.7	61.7	63.3	63.3	63.3	64.1	70.3	71.1	68.8	68.8
	<i>run 3</i>	54.7	59.4	60.9	61.7	60.9	60.9	63.3	63.3	63.3	64.1	64.1	64.1
	<i>run 4</i>	59.4	58.6	61.7	62.5	64.1	65.6	55.5	60.9	64.1	68.0	69.5	71.1
S07	<i>run 1</i>	52.3	57.8	57.8	57.8	57.0	57.0	51.6	56.3	53.1	54.7	51.6	50.8
	<i>run 2</i>	39.8	42.2	44.5	44.5	43.0	43.8	45.3	51.6	50.8	54.7	57.0	56.3
	<i>run 3</i>	38.3	41.4	40.6	40.6	40.6	40.6	40.6	36.7	41.4	42.2	43.0	43.8
	<i>run 4</i>	43.0	43.8	43.8	45.3	45.3	45.3	48.4	53.9	53.9	57.8	59.4	58.6
S08	<i>run 1</i>	46.9	50.0	53.1	53.9	53.9	53.9	52.3	57.8	61.7	60.9	61.7	60.2
	<i>run 2</i>	40.6	44.5	47.7	50.8	51.6	51.6	59.4	64.1	67.2	71.9	68.8	68.8
	<i>run 3</i>	46.1	49.2	53.9	53.1	53.9	53.9	50.0	55.5	59.4	60.9	63.3	63.3
	<i>run 4</i>	42.2	43.0	47.7	48.4	48.4	48.4	46.1	53.1	58.6	60.2	57.0	58.6
S09	<i>run 1</i>	39.1	39.8	42.9	41.4	43.7	43.8	34.4	39.1	39.1	40.6	40.6	39.8
	<i>run 2</i>	35.9	32.0	34.4	35.9	37.5	37.5	40.6	38.3	35.9	39.1	39.8	39.1
	<i>run 3</i>	39.1	38.3	38.3	37.5	35.9	35.9	35.9	38.3	36.7	38.3	40.6	39.8
	<i>run 4</i>	34.4	33.6	34.4	34.4	37.5	36.7	33.6	32.8	36.7	34.4	36.7	37.5

S10	<i>run 1</i>	30.5	32.8	34.4	35.2	35.2	35.2	39.1	39.8	39.8	39.1	41.4	41.4
	<i>run 2</i>	42.2	46.9	47.7	47.7	47.7	47.7	45.3	50.8	48.4	46.9	47.7	48.4
	<i>run 3</i>	32.0	35.2	35.9	35.9	35.9	35.9	35.9	40.6	41.4	42.2	43.0	43.0
	<i>run 4</i>	35.9	39.8	43.0	43.8	44.5	44.5	39.9	40.6	43.8	44.5	46.9	46.1
	Average	61.3	63.8	65.3	65.7	65.9	66.1	64.7	67.4	68.5	69.5	69.8	69.8
	Peak	95.3	96.1	96.1	96.9	96.9	96.9	95.3	97.7	96.1	96.1	96.1	96.1
	Average Δ	-	2.48	3.92	4.37	4.60	4.76	3.38	6.03	7.14	8.20	8.49	8.4
	Peak Δ	-	7.03	8.59	10.2	10.9	10.9	18.8	23.4	26.6	31.3	28.1	28.1

Table 5.2: p-values from the post-hoc comparisons between each pair of methods. The asterisks mark statistical significance: p<0.05 (*), p<0.01 (**), p<0.001 (***)

	CCA (1 corr)	CCA (2 corr)	CCA (3 corr)	CCA (4 corr)	CCA (5 corr)	CCA (6 corr)
CCA (1 corr)	-	p<10 ⁻⁵ ***	p<10 ⁻⁹ ***	p<10 ⁻⁹ ***	p<10 ⁻¹⁰ ***	p<10 ⁻¹⁰ ***
CCA (2 corr)	-	-	p<10 ⁻⁴ ***	p<10 ⁻⁵ ***	p<10 ⁻⁵ ***	p<10 ⁻⁵ ***
CCA (3 corr)	-	-	-	p=0.32	p=0.13	p=0.017 *
CCA (4 corr)	-	-	-	-	p=1	p=0.017 *
CCA (5 corr)	-	-	-	-	-	p=0.90
CCA (6 corr)	-	-	-	-	-	-
	CCA (1 corr) + sw	CCA (2 corr) + sw	CCA (3 corr) + sw	CCA (4 corr) + sw	CCA (5 corr) + sw	CCA (6 corr) + sw
CCA (1 corr) + sw	-	p<10 ⁻³ ***	p<10 ⁻⁵ ***	p<10 ⁻⁶ ***	p<10 ⁻⁶ ***	p<10 ⁻⁶ ***
CCA (2 corr) + sw	-	-	p=0.21	p<10 ⁻³ ***	p<10 ⁻³ ***	p=0.0022 **
CCA (3 corr) + sw	-	-	-	p=0.041 *	p=0.053	p=0.19
CCA (4 corr) + sw	-	-	-	-	p=1	p=1
CCA (5 corr) + sw	-	-	-	-	-	p=1
CCA (6 corr) + sw	-	-	-	-	-	-

	CCA (1 corr)	CCA (2 corr)	CCA (3 corr)	CCA (4 corr)	CCA (5 corr)	CCA (6 corr)
CCA (1 corr) + sw	p=0.0014 **	p=1	p=1	p=1	p=1	p=1
CCA (2 corr) + sw	p<10 ⁻⁸ ***	p=0.0015 **	p=0.22	p=0.77	p=1	p=1
CCA (3 corr) + sw	p<10 ⁻¹⁰ ***	p<10 ⁻⁴ ***	p=0.0025 **	p=0.0082 **	p=0.018 *	p=0.042 *
CCA (4 corr) + sw	p<10 ⁻¹⁰ ***	p<10 ⁻⁴ ***	p<10 ⁻⁴ ***	p<10 ⁻³ ***	p<10 ⁻³ ***	p<10 ⁻³ ***
CCA (5 corr) + sw	p<10 ⁻¹⁰ ***	p<10 ⁻⁶ ***	p<10 ⁻⁴ ***	p<10 ⁻⁴ ***	p<10 ⁻³ ***	p<10 ⁻³ ***
CCA (6 corr) + sw	p<10 ⁻¹⁰ ***	p<10 ⁻⁶ ***	p<10 ⁻⁴ ***	p<10 ⁻⁴ ***	p<10 ⁻³ ***	p<10 ⁻³ ***

Both the proposed variations were able to significantly improve classification accuracy. As regards variation 1, the results in Table 5.1, Table 5.2 and Figure 5.1 clearly show how the consideration of more than one canonical correlation significantly increases classification accuracy, both in the sinc-windowing and no-sinc-windowing conditions. Nevertheless, while accuracy significantly increases ($p < 0.001$, both with or without sinc-windowing) when switching from one to two canonical correlations, or from two to three ($p < 0.001$, in the no-sinc-windowing condition), the increment generally becomes insignificant when taking four, five or six canonical correlations, with respect e.g. to three. As concerns variation 2, i.e. the inclusion of a pre-filtering step around the K stimulation frequencies and N_{harm} harmonics by means of sinc-windowing, the results show how this kind of pre-processing always outperformed (with statistical significances ranging from $p < 0.001$ to $p < 0.01$) the corresponding version without processing. Accordingly, when variation 1 and variation 2 were combined, classification accuracy was a fortiori significantly ($p < 0.01$ or $p < 0.001$) increased with respect to the standard CCA method. To give an example, the accuracies obtained with using four canonical correlations and sinc-windowing were averagely increased by 8.20% with respect to the standard CCA method, with a peak increment of even 31.25% (in S08, run 2).

When varying the length of the EEG portions used to recognize the SSVEPs, the behavior of the proposed variations on classification accuracy tended to be confirmed, with the only exception of the 0.5s window length (Figure 5.2). While the consideration of more than one canonical correlations always outperformed the use of the largest one only, the positive impact of sinc-windowing emerged only for window lengths greater than 0.5-1s.

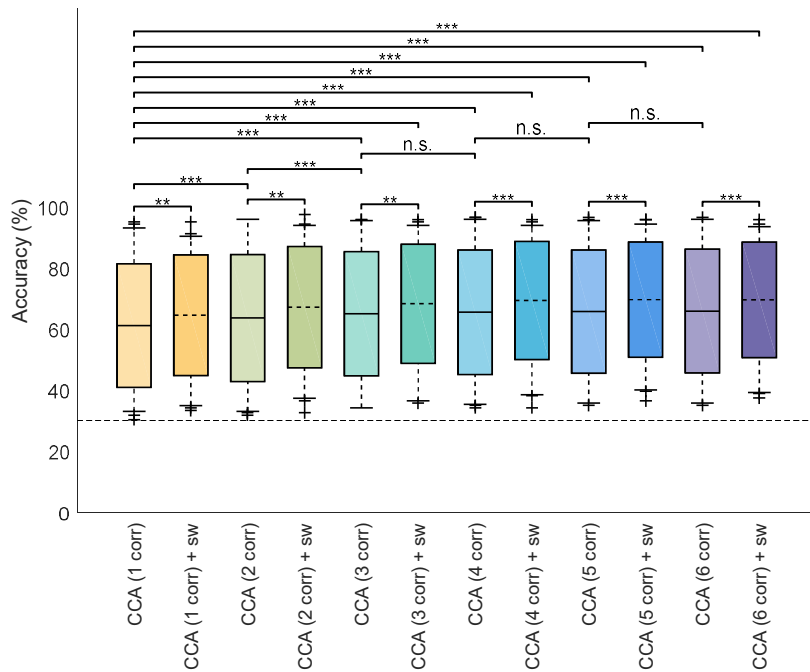


Figure 5.1. A box-plot showing the classification accuracy distributions for all the considered combinations of methods. The asterisks mark statistical significance - $p < 0.01$ (**), $p < 0.001$ (***) - while “n.s.” indicates the absence of significance. The horizontal, dashed line marks the upper confidence interval for chance level ($\alpha=1\%$).

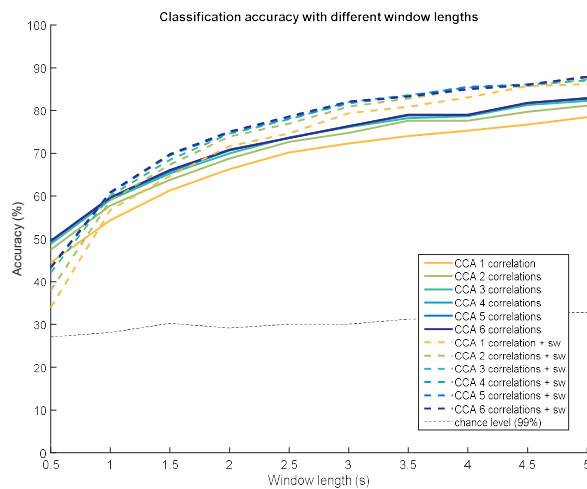


Figure 5.2: Grand average across subjects and runs of the classification accuracies for all the considered methods. The black dashed line indicates the upper confidence interval of the chance level ($\alpha=1\%$). Note that chance level is slightly different for the different time-windows, as the consideration of a larger time window implies a reduction in the number of trials per class.

5.4 Discussion

Our results show how the simple consideration of more than one canonical correlations can significantly improve the achievable accuracy without increasing computational load. As already suggested by Lin et al. (Lin et al., 2007), since real EEG signals are affected by noise and can show phase transitions, the information might be spread over more than one correlation coefficient.

From a theoretical point of view, if the EEG signals were almost unaffected by noise and shared the same phase across electrodes, then the consideration of only one canonical correlation would be sufficient to capture the majority of information. Being indeed the sine-cosine waves in each \mathbf{Y}_k an orthogonal basis, CCA would be able to find that particular linear combination of \mathbf{Y}_k elements able to explain the behavior of SSVEP response, through maximizing the correlation between linear combinations of \mathbf{X} (the EEG signals) and \mathbf{Y}_k , without leaving information behind. However, provided that \mathbf{X} is a multichannel set of data, if we suppose that the SSVEP response might show a different phase across electrodes, then at least a second set of canonical variables will be needed to explain the data, with the second set (U_2, V_2) containing a complementary information with respect to (U_1, V_1) . If we further suppose that, at the same EEG location, the different harmonics of the same SSVEP response might show different delays between each other, then at least another set of canonical variables (U_3, V_3) would be needed to capture the information of the SSVEP response not included in the first two sets. We suggest that both the above introduced suppositions are likely to be true in real EEG signals. Supposing indeed that the SSVEP response is generated in a limited area of the occipital cortex, then it will undergo different delays to reach the different locations from which the electrodes are acquired, due to a delay in spatial transmission. We suggest that the second supposition is also likely to be true in real EEG signals. Given indeed the origin of SSVEP in the occipital cortex, the signal has to pass multiple tissue layers (fluids, bone, skin) before reaching each EEG location. This is likely to produce phase distortion between different frequency components, besides the well-known spatial blurring effect. The above described interpretation fits the experimental data well, as the accuracy significantly increased when passing from one to three canonical correlation. We suggest that the consideration of more than one canonical correlation permits to include a more complete information on the investigated frequency f_k , which finally translates in an increased accuracy, revealed in almost every subject and run. From the third set of canonical variables on, the amount of information included probably depends on each user's individual characteristics, e.g. the amount of delay across different harmonics and electrodes, as well as the magnitude of SSVEP between different harmonics of the same stimulation frequency. Given their dependency on each subject's individual characteristics, from

the fourth canonical correlation on there was not a group effect anymore, and the increments in accuracy were not anymore significant.

Besides suggesting the consideration of more than one canonical correlation, our results also highlight the positive impact of including a pre-filtering step before performing CCA. The presence of a filtering stage around the K stimulation frequencies and related N_{harm} harmonics may have permitted to enhance the SSVEP response from the background EEG, which finally translated in a significantly increased accuracy in every considered comparison between corresponding versions of the method, with or without pre-filtering. The idea of adding a filtering stage to enhance different SSVEP components had been already introduced in the works of Chen et al (Chen et al., 2015) and Islam et al (Islam et al., 2016), suggesting the use of IIR filter banks. However, both algorithm implementations in (Chen et al., 2015; Islam et al., 2016) proposed to perform multiple CCAs, each time after a different pre-filtering of the same EEG portion, to assess each single stimulation frequency. Although able to produce a significant increase in classification accuracy, this implies a multiplication of the total number of steps required in each SSVEP recognition, with a related sensible increment of computational load. Besides being a novelty with respect to literature, the implementation of the pre-filtering by means of sinc-windowing has the advantage of being able to filter multiple frequency components in one single step, by simply modulating the composition of the convolved function. This implies that one more single step is added to each SSVEP recognition, independently from the number K of stimulation frequency or N_{harm} considered harmonics, thus overall remaining computationally light. A potential limitation of the sinc-windowing technique might be related to the length of the considered signal portions, due to the Gibbs truncation effect (Carslaw, 1930). As indeed shown in Figure 5.2, while for segment lengths longer than 1s sinc-windowing increases the achievable accuracy, it turned to have even a negative impact when considering a short signal portion, of 0.5s. As a final comment on the sinc-windowing technique, it might be noted that its efficacy was generally confirmed despite the closeness of the chosen the stimulation frequencies (8, 9 10 and 11Hz).

As regards the obtained accuracies in absolute terms, we can comment that our results are in line with literature regarding multi-class SSVEP-based BCIs relying on the standard CCA technique (Bin et al., 2009; Chen et al., 2015; Dongxue et al., 2015; Hakvoort et al., 2011; Lin et al., 2007). Nevertheless, it could be noted that set of stimulation frequencies and/or of the duty-cycles (Shyu et al., 2013) of stimulations were chosen beforehand and they were same for all subject, therefore a subject-specific calibration would theoretically produce a further increment of all accuracies.

5.5 Conclusion

In the present work, we performed a 4-class SSVEP recognition based on CCA analysis. However, we evaluated the impact of two slight variations with respect to the standard algorithm, involving i) the number of considered canonical correlations and ii) the inclusion of a narrow-band pre-filtering step around the employed stimulation frequencies and related harmonics, by means of sinc-windowing technique. Our results indicate that even simple consideration of more than one canonical correlation can significantly improve accuracy, without any increment of computational load. Notably, there were significant increases in accuracy when switching from one to three canonical correlations, while the increments were not significant from the fourth canonical correlation on. An additional narrow-band pre-filtering permitted to gain up to 7-8% of accuracy on average, with peaks of 25-30%, with respect to classical CCA. A further advantage of sinc-windowing implementation is that it permits the enhancement of multiple frequency components in one single step, by simply modulating the composition of the sinc-function. Given the significant increases in accuracy produced by both the proposed variations, either they were used separately or - even more - in combination, together with the minimal computational costs, we believe they could easily represent valid integrations to be included in future CCA designs.

General conclusions

This thesis presented several research activities in the field of EEG-based Brain-Computer Interfaces for both neurorehabilitation and control purposes.

In **chapter 2**, we tested whether contralateral tDCS could be used to enhance BCI-guided MI training, by producing a remote facilitation of ERD through the modification of interhemispheric balance. Our initial hypothesis was that tDCS could exploit interhemispheric inhibition, i.e. that contralateral cathodal stimulation could result in facilitation of ERD on the unstimulated hemisphere, while contralateral anodal stimulation could result in inhibition.

From the analysis of spectral power and ERD, two main findings emerged: i) contralateral alpha-ERD was reduced after anodal, but not enhanced after cathodal tDCS, ii) both stimulations had remote effects on the EEG rhythms of the contralateral hemisphere. The absence of contralateral cathodal ERD enhancement suggests that the protocol is not applicable in the context of BCI-guided MI training. Nevertheless, ERD results of anodal and spectral power results of both stimulations support the hypothesis of an interhemispheric effect, complementing recent findings on the distant tDCS effect between functionally related areas.

Chapter 3 presented a co-adaptive BCI system based on motor imagery. The system was tested on ten subjects, of whom seven reached the criterion level of 70% accuracy in three days. In regard to the accuracies, the results are in line with the ones of other co-adaptive studies. However, beyond the proposed adaptive strategy, we believe the main novelties in this chapter regard the way the machine interacts with the user during training. Some ideas introduced in this work may be included into setups even different from ours, like the flexibility in the training paradigm, adapting to the performance of the user, or the imbalance in the presentation of conditions in favour of the most misclassified one, permitting both the user and the machine to train more on the most critical class. Even though this was an early work, and research directions in recent years have started shifting towards different frontiers, we believe the proposed ideas and elements of design could be useful, in synergy with more sophisticated algorithms and adaptive schemes, to the goal of making learning voluntary control of SMR more efficient and comfortable for the user.

On a more recent research direction there is the activity of **chapter 4**, carried out during my internship at the Institute of Neural Engineering, Graz University of Technology, Austria. In this study, we developed for the first time the experimental tools and a paradigm to allow for real-time continuous control of a robotic arm by means of noninvasively EEG-decoded movements. The main challenges of the project arose from the online processing delays, forcing us to relax the constraints over the characteristics of the EEG filter. The overall effect was an enlargement of the filtered bandwidth, which would have resulted in decoded trajectories with higher frequency jitters with respect to the movement. One beneficial element of design in this sense was the introduction of the Kalman filter. Besides increasing the correlation of the decoder output with the real movement, Kalman filter had indeed a smoothing effect. This brought back the decoded trajectories to a similar frequency spectrum as the real movement, thus overall increasing the quality of the feedback. Despite the differences introduced by online decoding, and the additional delays when closing the loop with a robotic arm, the results are consistent with previous findings from offline decoding studies, as also confirmed by the analysis of EEG sources. Finally, the movement could be decoded from all participants above chance level, even in the case of 100% EEG control. Altogether, the study in this chapter takes a first step towards online continuous control based on noninvasive movement decoding. Next challenges may regard the minimization of the calibration time needed for the decoder, or the investigation of reinforcement learning over multiple days.

In **chapter 5** of this thesis we finally addressed SSVEP recognition based on the Canonical Correlation Analysis (CCA) approach. We proposed two simple improvements in i) the pre-processing of the signal and ii) the number of considered canonical correlations, which were able to consistently and significantly improve classification accuracy with no or minimal impact on computational load. While the reasons underlying the beneficial effect of taking more correlations were discussed in the chapter, the sinc-windowing approach represents a simple but ecological way to enhance all the frequency components of interest for classification, but in just one additional processing step. Given their modular structure and their minimal computational cost, we believe the proposed variations may easily be included in future CCA-based designs, especially in view of low-cost and high-portability devices.

Although drawing a general conclusion is difficult, for the variety of the research questions addressed in each chapter, we believe this work has overall managed to introduce some novelty to the field, either by proposing new elements, refining the methods, or complementing the most recent findings in literature. On a more general note, some hints on next steps that might be taken in BCI research, both for neurorehabilitation and control, are suggested in the following.

In regard to neurorehabilitation, the efficacy of BCIs to trigger neurological recovery is being progressively confirmed. A number of recent clinical studies has shown the efficacy of BCI training with respect to control groups, not only in terms of neurological but also functional recovery. Next steps in this field might be taken towards improving the simplicity and reliability of hardware and software, especially in view of home-based training in the chronic phase, or the customizability of the systems to meet the specific needs and objectives of end-users. On a slightly different note, but always arising from the topics addressed in this thesis, some hints might be given towards improving reliability and usability of tDCS as well. Although there is evidence of the efficacy of stimulation to enhance recovery, even in the chronically damaged brain, the exact mechanisms underlying neuromodulation are still poorly understood. The development and use of computational models, ideally able to span across levels of description and ultimately link dose of stimulation to neurophysiology and behavior (e.g. from the new branch of research known as “computational neurostimulation”), might be useful to further improve the understanding and, therefore, reliability, of this second technique.

Finally, in regard to BCIs for control purposes, next steps might be taken towards improving the intuitiveness of control, in order to increase usability of the systems. On one side, a better understanding of the factors and mechanisms influencing the learning of BCI control might help to design more efficient and optimized paradigms. On the other side, the exploratory effort towards novel and more intuitive control frameworks, like the recently envisioned continuous decoding of movement intention, may provide in the next years the BCI community with new theoretical knowledge and technical tools, allowing for the envisioning of new possible solutions.

Acknowledgments

Getting to the conclusion of this beautiful journey, I feel very grateful to many people who were (unluckily for them) part of it, and whom I would like to take here the chance to thank.

I would first like to thank my supervisor, Prof. Angelo Cappello, for giving me the opportunity to start and complete this journey, for trusting me, and guiding me in the development of a research attitude that I admired in him at the beginning, and I hope to have more or less integrated along the way.

A huge thank you goes to Dr. Anna Lisa Mangia, for her endless support and patience, the long talks, the friendship, and for leading by example of humility, hard work and true passion for research.

I also could not be more grateful to Prof. Gernot Müller-Putz. Having had the possibility to join his lab for a while has been for me one of the most incredible opportunities. The experience has been inspiring me at so many levels, in terms of stimulating and extremely positive environment, beautiful group dynamics and, of course, quality of research.

A very huge thank you goes of course to the members of the BCI lab! for welcoming me from the beginning, for the inspiring and fruitful discussions... and for making my stay in Graz truly the best possible. Thanks to Catarina, Andreea, Lea, Joana, Patrick, Andreas, Karina, Maria... although I really need to give my special thanks to Reinmar: for sharing with me part of his Ph.D. project, for the tireless effort and enthusiasm, a true driving force and source of inspiration.

Thanks to my colleagues at the University of Bologna, for supporting and inspiring me and for making these years much more pleasant... among these Giulia, Chiara, Chiara, Joseph, Enrico...

... although the final dedication of this work is to my family. To my grandma, mum and dad... grazie.

References

- Allison, B.Z., McFarland, D.J., Schalk, G., Zheng, S.D., Jackson, M.M., and Wolpaw, J.R. (2008). Towards an independent brain–computer interface using steady state visual evoked potentials. *Clinical Neurophysiology* 119, 399–408.
- Anderer, P., Roberts, S., Schlögl, A., Gruber, G., Klösch, G., Herrmann, W., Rappelsberger, P., Filz, O., Barbanj, M.J., Dorffner, G., et al. (1999). Artifact Processing in Computerized Analysis of Sleep EEG – A Review. *NPS* 40, 150–157.
- Ang, K.K., Guan, C., Chua, K.S.G., Ang, B.T., Kuah, C., Wang, C., Phua, K.S., Chin, Z.Y., and Zhang, H. (2010). Clinical study of neurorehabilitation in stroke using EEG-based motor imagery brain-computer interface with robotic feedback. *Conf Proc IEEE Eng Med Biol Soc 2010*, 5549–5552.
- Ang, K.K., Guan, C., Phua, K.S., Wang, C., Zhao, L., Teo, W.P., Chen, C., Ng, Y.S., and Chew, E. (2015). Facilitating effects of transcranial direct current stimulation on motor imagery brain-computer interface with robotic feedback for stroke rehabilitation. *Arch Phys Med Rehabil* 96, S79-87.
- B. Blankertz, F. Losch, M. Krauledat, and G. Dornhege (2008). The Berlin Brain-Computer Interface: Accurate Performance From First-Session in BCI-Naive Subjects.
- Baillet, S., Mosher, J.C., and Leahy, R.M. (2001). Electromagnetic brain mapping. *Signal Processing Magazine, IEEE* 18, 14–30.
- Barbero, Á., and Grosse-Wentrup, M. (2010). Biased feedback in brain-computer interfaces. *Journal of Neuroengineering and Rehabilitation* 7, 34.
- Bar-Shalom, Y., Rong Li, X., and Kirubarajan, T. (2002). *Estimation with Applications to Tracking and Navigation: Theory, Algorithms and Software* (Wiley).
- Bartz, D., and Müller, K.R. (2014). Covariance shrinkage for autocorrelated data. *Advances in Neural Information Processing Systems* 1592–1600.
- Batsikadze, G., Moliadze, V., Paulus, W., Kuo, M.-F., and Nitsche, M.A. (2013). Partially non-linear stimulation intensity-dependent effects of direct current stimulation on motor cortex excitability in humans. *J. Physiol. (Lond.)* 591, 1987–2000.
- Bäumer, T., Dammann, E.M., Bock, F., Klöppel, S., Siebner, H.R., and Münchau, A. (2007). Laterality of interhemispheric inhibition depends on handedness. *Exp Brain Res* 180, 195–203.
- Baxter, B.S., Edelman, B., Zhang, X., Roy, A., and He, B. (2014). Simultaneous high-definition transcranial direct current stimulation of the motor cortex and motor imagery. *Conf Proc IEEE Eng Med Biol Soc 2014*, 454–456.

- Baxter, B.S., Edelman, B.J., Nesbitt, N., and He, B. (2016). Sensorimotor Rhythm BCI with Simultaneous High Definition-Transcranial Direct Current Stimulation Alters Task Performance. *Brain Stimulation* 9, 834–841.
- Bazhenov, M., Timofeev, I., Steriade, M., and Sejnowski, T.J. (2002). Model of thalamocortical slow-wave sleep oscillations and transitions to activated states. *Journal of Neuroscience* 22, 8691–8704.
- Benjamini, Y., and Hochberg, Y. (1995). Controlling the False Discovery Rate: A Practical and Powerful Approach to Multiple Testing. *Journal of the Royal Statistical Society. Series B (Methodological)* 57, 289–300.
- Berger, H. (1929). Über das Elektrenkephalogramm des Menschen. *European Archives of Psychiatry and Clinical Neuroscience* 87, 527–570.
- Billinger, M., Daly, I., Kaiser, V., Jin, J., Allison, B.Z., Müller-Putz, G.R., and Brunner, C. (2013). Is it significant? Guidelines for reporting BCI performance. In *Towards Practical Brain-Computer Interfaces*, (Springer), pp. 333–354.
- Bin, G., Gao, X., Yan, Z., Hong, B., and Gao, S. (2009). An online multi-channel SSVEP-based brain-computer interface using a canonical correlation analysis method. *J. Neural Eng.* 6, 046002.
- Birbaumer, N., and Cohen, L.G. (2007). Brain-computer interfaces: communication and restoration of movement in paralysis. *The Journal of Physiology* 579, 621–636.
- Birbaumer, N., Kübler, A., Ghanayim, N., Hinterberger, T., Perelmouter, J., Kaiser, J., Iversen, I., Kotchoubey, B., Neumann, N., and Flor, H. (2000). The thought translation device (TTD) for completely paralyzed patients. *IEEE Trans Rehabil Eng* 8, 190–193.
- Black, M.J., Bienenstock, E., Donoghue, J.P., Serruya, M., Wu, W., and Gao, Y. (2003). Connecting brains with machines: the neural control of 2D cursor movement. In *Proc. 1st International IEEE/EMBS Conference on Neural Engineering*, (Citeseer), pp. 580–583.
- Boto, E., Holmes, N., Leggett, J., Roberts, G., Shah, V., Meyer, S.S., Muñoz, L.D., Mullinger, K.J., Tierney, T.M., Bestmann, S., et al. (2018). Moving magnetoencephalography towards real-world applications with a wearable system. *Nature* 555, 657–661.
- Box, G.E.P., and Cox, D.R. (1964). An Analysis of Transformations. *Journal of the Royal Statistical Society. Series B (Methodological)* 26, 211–252.
- Bradberry, T.J., Rong, F., and Contreras-Vidal, J.L. (2009). Decoding center-out hand velocity from MEG signals during visuomotor adaptation. *NeuroImage* 47, 1691–1700.

- Bradberry, T.J., Gentili, R.J., and Contreras-Vidal, J.L. (2010). Reconstructing Three-Dimensional Hand Movements from Noninvasive Electroencephalographic Signals. *J. Neurosci.* *30*, 3432–3437.
- Brainard, D.. The Psychophysics Toolbox. *Spatial Vision* *10*, 433–435.
- Burges, C.J.C. (1998). A Tutorial on Support Vector Machines for Pattern Recognition. *Data Mining and Knowledge Discovery* *2*, 121–167.
- Caminiti, R., Johnson, P.B., and Urbano, A. (1990). Making arm movements within different parts of space: dynamic aspects in the primate motor cortex. *J. Neurosci.* *10*, 2039–2058.
- Caplan, J.B., Madsen, J.R., Raghavachari, S., and Kahana, M.J. (2001). Distinct Patterns of Brain Oscillations Underlie Two Basic Parameters of Human Maze Learning. *Journal of Neurophysiology* *86*, 368–380.
- Carmena, J.M., Lebedev, M.A., Crist, R.E., O’doherly, J.E., Santucci, D.M., Dimitrov, D.F., Patil, P.G., Henriquez, C.S., and Nicolelis, M.A.L. (2003). Learning to control a brain-machine interface for reaching and grasping by primates. *PLoS Biology* *1*, E42.
- Carmichael, S.T. (2003). Plasticity of Cortical Projections after Stroke. *Neuroscientist* *9*, 64–75.
- Carlsaw, H.S. (1930). Introduction to the theory of Fourier’s series and integrals. New York: Dover, 1930, 3rd Ed.
- Chang, M.H., and Park, K.S. (2013). Frequency recognition methods for dual-frequency SSVEP based brain-computer interface. In *Engineering in Medicine and Biology Society (EMBC), 2013 35th Annual International Conference of the IEEE, (IEEE)*, pp. 2220–2223.
- Chaudhary, U., Birbaumer, N., and Ramos-Murguialday, A. (2016). Brain-computer interfaces for communication and rehabilitation. *Nat Rev Neurol* *12*, 513–525.
- Chen, X., Wang, Y., Gao, S., Jung, T.-P., and Gao, X. (2015). Filter bank canonical correlation analysis for implementing a high-speed SSVEP-based brain-computer interface. *Journal of Neural Engineering* *12*, 046008.
- Cheng, M., Gao, X., Gao, S., and Xu, D. (2002). Design and implementation of a brain-computer interface with high transfer rates. *IEEE Transactions on Biomedical Engineering* *49*, 1181–1186.
- Cincotti, F., Mattia, D., Aloise, F., Bufalari, S., Astolfi, L., Fallani, F.D.V., Tocci, A., Bianchi, L., Marciani, M.G., Gao, S., et al. (2008). High-resolution EEG techniques for brain-computer interface applications. *Journal of Neuroscience Methods* *167*, 31–42.

- Cortes, C., and Vapnik, V. (1995). Support-vector networks. *Machine Learning* 20, 273–297.
- Cramer, S.C. (2008). Repairing the human brain after stroke: I. Mechanisms of spontaneous recovery. *Annals of Neurology* 63, 272–287.
- Cramer, S.C., Nelles, G., Benson, R.R., Kaplan, J.D., Parker, R.A., Kwong, K.K., Kennedy, D.N., Finklestein, S.P., and Rosen, B.R. (1997). A functional MRI study of subjects recovered from hemiparetic stroke. *Stroke* 28, 2518–2527.
- Culham, J.C., and Valyear, K.F. (2006). Human parietal cortex in action. *Current Opinion in Neurobiology* 16, 205–212.
- Da Silva, F.L. (2009). EEG: Origin and measurement. In *EEG-FMRI*, (Springer), pp. 19–38.
- Daly, J.J., and Wolpaw, J.R. (2008). Brain-computer interfaces in neurological rehabilitation. *Lancet Neurol* 7, 1032–1043.
- deCharms, R.C., Christoff, K., Glover, G.H., Pauly, J.M., Whitfield, S., and Gabrieli, J.D.E. (2004). Learned regulation of spatially localized brain activation using real-time fMRI. *NeuroImage* 21, 436–443.
- Delorme, A., and Makeig, S. (2004). EEGLAB: an open source toolbox for analysis of single-trial EEG dynamics including independent component analysis. *Journal of Neuroscience Methods* 134, 9–21.
- Di Lazzaro, V., Oliviero, A., Profice, P., Insola, A., Mazzone, P., Tonali, P., and Rothwell, J.C. (1999). Direct demonstration of interhemispheric inhibition of the human motor cortex produced by transcranial magnetic stimulation. *Experimental Brain Research* 124, 520–524.
- Di Lazzaro, V., Manganelli, F., Dileone, M., Notturmo, F., Esposito, M., Capasso, M., Dubbioso, R., Pace, M., Ranieri, F., Minicuci, G., et al. (2012). The effects of prolonged cathodal direct current stimulation on the excitatory and inhibitory circuits of the ipsilateral and contralateral motor cortex. *J Neural Transm (Vienna)* 119, 1499–1506.
- Dickhaus, T., Sannelli, C., Müller, K.-R., Curio, G., and Blankertz, B. (2009). Predicting BCI performance to study BCI illiteracy. *BMC Neuroscience* 10, P84.
- van Dokkum, L., Ward, T.E., and Laffont, I. (2015). Brain computer interfaces for neurorehabilitation – its current status as a rehabilitation strategy post-stroke. *Ann Phys Rehabil Med* 58, 3–8.
- Dongxue, L., Chuan, T.J.T., Chi, Z., and Feng, D. (2015). Design of an online BCI system based on CCA detection method. In *2015 34th Chinese Control Conference (CCC)*, pp. 4728–4733.

- Faller, J., Vidaurre, C., Solis-Escalante, T., Neuper, C., and Scherer, R. (2012). Autocalibration and recurrent adaptation: towards a plug and play online ERD-BCI. *Neural Systems and Rehabilitation Engineering, IEEE Transactions On* 20, 313–319.
- Faller, J., Solis-Escalante, T., Costa, U., Opisso, E., Medina, J., Scherer, R., and Müller-Putz, G.R. (2013). Online co-adaptive brain-computer interfacing: Preliminary results in individuals with spinal cord injury. In *Neural Engineering (NER), 2013 6th International IEEE/EMBS Conference On, (IEEE)*, pp. 977–980.
- Faller, J., Scherer, R., Costa, U., Opisso, E., Medina, J., and Müller-Putz, G.R. (2014). A co-adaptive brain-computer interface for end users with severe motor impairment. *PLoS ONE* 9, e101168.
- Farwell, L.A., and Donchin, E. (1988). Talking off the top of your head: toward a mental prosthesis utilizing event-related brain potentials. *Electroencephalography and Clinical Neurophysiology* 70, 510–523.
- Ferbert, A., Priori, A., Rothwell, J.C., Day, B.L., Colebatch, J.G., and Marsden, C.D. (1992). Interhemispheric inhibition of the human motor cortex. *J Physiol* 453, 525–546.
- Fernández, T., Harmony, T., Rodríguez, M., Bernal, J., Silva, J., Reyes, A., and Marosi, E. (1995). EEG activation patterns during the performance of tasks involving different components of mental calculation. *Electroencephalography and Clinical Neurophysiology* 94, 175–182.
- Filimon, F., Nelson, J.D., Hagler, D.J., and Sereno, M.I. (2007). Human cortical representations for reaching: Mirror neurons for execution, observation, and imagery. *NeuroImage* 37, 1315–1328.
- Filimon, F., Nelson, J.D., Huang, R.-S., and Sereno, M.I. (2009). Multiple Parietal Reach Regions in Humans: Cortical Representations for Visual and Proprioceptive Feedback during On-Line Reaching. *J. Neurosci.* 29, 2961–2971.
- Fonov, V., Evans, A.C., Botteron, K., Almli, C.R., McKinstry, R.C., and Collins, D.L. (2011). Unbiased average age-appropriate atlases for pediatric studies. *NeuroImage* 54, 313–327.
- Furdea, A., Halder, S., Krusienski, D.J., Bross, D., Nijboer, F., Birbaumer, N., and Kübler, A. (2009). An auditory oddball (P300) spelling system for brain-computer interfaces. *Psychophysiology* 46, 617–625.
- G. Pfurtscheller, C. Guger, G. Müller, G. Krausz, and C. Neuper (2000). Brain oscillations control hand orthosis in a tetraplegic.
- G. Pfurtscheller, C. Neuper, G.R. Müller, B. Obermaier, G. Krausz, A. Schlogl, and R. Scherer (2003). Graz-BCI: state of the art and clinical applications.

- Ganguly, K., Byl, N.N., and Abrams, G.M. (2013). Neurorehabilitation: Motor recovery after stroke as an example. *Annals of Neurology* 74, 373–381.
- Georgopoulos, A.P., Kalaska, J.F., Caminiti, R., and Massey, J.T. (1982). On the relations between the direction of two-dimensional arm movements and cell discharge in primate motor cortex. *J. Neurosci.* 2, 1527–1537.
- Georgopoulos, A.P., Langheim, F.J.P., Leuthold, A.C., and Merkle, A.N. (2005). Magnetoencephalographic signals predict movement trajectory in space. *Exp Brain Res* 167, 132–135.
- Gilio, F., Rizzo, V., Siebner, H.R., and Rothwell, J.C. (2003). Effects on the right motor hand-area excitability produced by low-frequency rTMS over human contralateral homologous cortex. *The Journal of Physiology* 551, 563–573.
- Gramfort, A., Papadopoulos, T., Olivi, E., and Clerc, M. (2010). OpenMEEG: opensource software for quasistatic bioelectromagnetics. *BioMedical Engineering OnLine* 9.
- Guger, C., Ramoser, H., and Pfurtscheller, G. (2000). Real-time EEG analysis with subject-specific spatial patterns for a brain-computer interface (BCI). *IEEE Transactions on Rehabilitation Engineering* 8, 447–456.
- Gwin, J.T., Gramann, K., Makeig, S., and Ferris, D.P. (2010). Removal of Movement Artifact From High-Density EEG Recorded During Walking and Running. *Journal of Neurophysiology* 103, 3526–3534.
- Hakvoort, G., Reuderink, B., and Obbink, M. (2011). Comparison of PSDA and CCA detection methods in a SSVEP-based BCI-system.
- Hatem, S.M., Saussez, G., della Faille, M., Prist, V., Zhang, X., Dispa, D., and Bleyenheuft, Y. (2016). Rehabilitation of Motor Function after Stroke: A Multiple Systematic Review Focused on Techniques to Stimulate Upper Extremity Recovery. *Front Hum Neurosci* 10.
- Haufe, S., Meinecke, F., Görgen, K., Dähne, S., Haynes, J.-D., Blankertz, B., and Bießmann, F. (2014). On the interpretation of weight vectors of linear models in multivariate neuroimaging. *NeuroImage* 87, 96–110.
- He, B. (2007). *Neural Engineering* (Springer Science & Business Media).
- Hill, N.J., Lal, T.N., Schröder, M., Hinterberger, T., Widman, G., Elger, C.E., Schölkopf, B., and Birbaumer, N. (2006). Classifying event-related desynchronization in EEG, ECoG and MEG signals. In *Pattern Recognition*, (Springer), pp. 404–413.
- Hochberg, Y., and Tamhane, A.C. (1987). Frontmatter. In *Multiple Comparison Procedures*, (John Wiley & Sons, Inc.), pp. i–xxii.

- Hochberg, L.R., Bacher, D., Jarosiewicz, B., Masse, N.Y., Simeral, J.D., Vogel, J., Haddadin, S., Liu, J., Cash, S.S., van der Smagt, P., et al. (2012). Reach and grasp by people with tetraplegia using a neurally controlled robotic arm. *Nature* 485, 372–375.
- Homan, R.W., Herman, J., and Purdy, P. (1987). Cerebral location of international 10-20 system electrode placement. *Electroencephalogr Clin Neurophysiol* 66, 376–382.
- Hong, K.-S., Khan, M.J., and Hong, M.J. (2018). Feature Extraction and Classification Methods for Hybrid fNIRS-EEG Brain-Computer Interfaces. *Front Hum Neurosci* 12, 246.
- Hotelling, H. (1936). Relations between two sets of variates. *Biometrika* 28, 321–377.
- Hummel, F.C., and Cohen, L.G. (2006). Non-invasive brain stimulation: a new strategy to improve neurorehabilitation after stroke? *Lancet Neurol* 5, 708–712.
- Islam, M.R., Tanaka, T., Nakanishi, M., and Molla, M.K.I. (2016). Frequency recognition of steady-state visually evoked potentials using binary subband canonical correlation analysis with reduced dimension of reference signals. In *Acoustics, Speech and Signal Processing (ICASSP), 2016 IEEE International Conference On, (IEEE)*, pp. 769–773.
- Iturrate, I., Antelis, J.M., Kubler, A., and Minguez, J. (2009). A Noninvasive Brain-Actuated Wheelchair Based on a P300 Neurophysiological Protocol and Automated Navigation. *IEEE Transactions on Robotics* 25, 614–627.
- Jatzev, S., Zander, T.O., De Filippis, M., Kothe, C., Welke, S., and Rötting, M. (2008). Examining causes for non-stationarities: The loss of controllability is a factor which induces non-stationarities. *Proceedings of the 4th International Brain-Computer Interface Workshop and Training Course* 138–143.
- Jeannerod, M. (1995). Mental imagery in the motor context. *Neuropsychologia* 33, 1419–1432.
- de Jong, S. (1993). SIMPLS: An alternative approach to partial least squares regression. *Chemometrics and Intelligent Laboratory Systems* 18, 251–263.
- Jung, T.-P., Makeig, S., Bell, A.J., and Sejnowski, T.J. (1998). Independent Component Analysis of Electroencephalographic and Event-Related Potential Data. In *Central Auditory Processing and Neural Modeling*, P.W.F. Poon, and J.F. Brugge, eds. (Boston, MA: Springer US), pp. 189–197.
- Jung, T.-P., Makeig, S., Humphries, C., Lee, T.-W., McKEOWN, M.J., Iragui, V., and Sejnowski, T.J. (2000). Removing electroencephalographic artifacts by blind source separation. *Psychophysiology* 37, 163–178.

- Kalaska, J.F., Caminiti, R., and Georgopoulos, A.P. (1983). Cortical mechanisms related to the direction of two-dimensional arm movements: relations in parietal area 5 and comparison with motor cortex. *Exp Brain Res* 51, 247–260.
- Kalman, R.E. (1960). A New Approach to Linear Filtering and Prediction Problems. *J. Basic Eng* 82, 35–45.
- Kasashima, Y., Fujiwara, T., Matsushika, Y., Tsuji, T., Hase, K., Ushiyama, J., Ushiba, J., and Liu, M. (2012). Modulation of event-related desynchronization during motor imagery with transcranial direct current stimulation (tDCS) in patients with chronic hemiparetic stroke. *Exp Brain Res* 221, 263–268.
- Kasashima-Shindo, Y., Fujiwara, T., Ushiba, J., Matsushika, Y., Kamatani, D., Oto, M., Ono, T., Nishimoto, A., Shindo, K., Kawakami, M., et al. (2015). Brain-computer interface training combined with transcranial direct current stimulation in patients with chronic severe hemiparesis: Proof of concept study. *J Rehabil Med* 47, 318–324.
- Kasuga, S., Matsushika, Y., Kasashima-Shindo, Y., Kamatani, D., Fujiwara, T., Liu, M., and Ushiba, J. (2015). Transcranial direct current stimulation enhances mu rhythm desynchronization during motor imagery that depends on handedness. *Laterality: Asymmetries of Body, Brain and Cognition* 20, 453–468.
- Kim, B.H., Chun, J., and Jo, S. (2015). Dynamic motion artifact removal using inertial sensors for mobile BCI. In 2015 7th International IEEE/EMBS Conference on Neural Engineering (NER), pp. 37–40.
- Kiran, S. (2012). What Is the Nature of Poststroke Language Recovery and Reorganization?
- Kleim, J.A. (2011). Neural plasticity and neurorehabilitation: Teaching the new brain old tricks. *Journal of Communication Disorders* 44, 521–528.
- Kleiner, M., Brainard, D., and Pelli, D. (2007). What's new in Psychtoolbox-3? *Perception* 36, 1–16.
- Klem, G.H., Lüders, H.O., Jasper, H.H., and Elger, C. (1999). The ten-twenty electrode system of the International Federation. *Electroencephalogr Clin Neurophysiol* 52, 3.
- Klimesch, W. (1999). EEG alpha and theta oscillations reflect cognitive and memory performance: a review and analysis. *Brain Research Reviews* 29, 169–195.
- Klimesch, W., Doppelmayr, M., Yonelinas, A., Kroll, N.E.A., Lazzara, M., Röhme, D., and Gruber, W. (2001). Theta synchronization during episodic retrieval: neural correlates of conscious awareness. *Cognitive Brain Research* 12, 33–38.
- Klimesch, W., Sauseng, P., and Hanslmayr, S. (2007). EEG alpha oscillations: The inhibition–timing hypothesis. *Brain Research Reviews* 53, 63–88.

- Kobler, R.J., and Scherer, R. (2016). Restricted Boltzmann Machines in Sensory Motor Rhythm Brain-Computer Interfacing: A study on inter-subject transfer and co-adaptation. In 2016 IEEE International Conference on Systems, Man, and Cybernetics (SMC), pp. 000469–000474.
- Kobler, R.J., Sburlea, A.I., and Müller-Putz, G.R. (2017). A Comparison of Ocular Artifact Removal Methods for Block Design Based Electroencephalography Experiments. Proceedings of the 7th Graz Brain-Computer Interface Conference 236–241.
- Kobler, R.J., Sburlea, A.I., and Müller-Putz, G.R. (2018). Tuning characteristics of low-frequency EEG to positions and velocities in visuomotor and oculomotor tracking tasks. *Scientific Reports* 8, 17713.
- Koles, Z.J., Lazar, M.S., and Zhou, S.Z. (1990). Spatial patterns underlying population differences in the background EEG. *Brain Topography* 2, 275–284.
- Korik, A., Siddique, N.H., Sosnik, R., and Coyle, D. (2014). Correlation of EEG Band Power and Hand Motion Trajectory. Proceedings of the 6th International Brain-Computer Interface Conference Article ID 095-4.
- Krucoff, M.O., Rahimpour, S., Slutzky, M.W., Edgerton, V.R., and Turner, D.A. (2016). Enhancing Nervous System Recovery through Neurobiologics, Neural Interface Training, and Neurorehabilitation. *Front. Neurosci.* 10.
- Kwakkel, G., Kollen, B., and Lindeman, E. (2004). Understanding the pattern of functional recovery after stroke: facts and theories. *Restor. Neurol. Neurosci.* 22, 281–299.
- Kwakkel, G., Kollen, B., and Twisk, J. (2006). Impact of time on improvement of outcome after stroke. *Stroke* 37, 2348–2353.
- Kybic, J., Clerc, M., Abboud, T., Faugeras, O., Keriven, R., and Papadopoulos, T. (2005). A common formalism for the Integral formulations of the forward EEG problem - IEEE Journals & Magazine. *IEEE Transactions on Medical Imaging* 24, 12–28.
- Lang, N., Nitsche, M.A., Paulus, W., Rothwell, J.C., and Lemon, R.N. (2004). Effects of transcranial direct current stimulation over the human motor cortex on corticospinal and transcallosal excitability. *Exp Brain Res* 156, 439–443.
- Lapenta, O.M., Minati, L., Fregni, F., and Boggio, P.S. (2013). Je pense donc je fais: transcranial direct current stimulation modulates brain oscillations associated with motor imagery and movement observation. *Front Hum Neurosci* 7, 256.
- Laureys, S., Boly, M., and Tononi, G. (2009). *Functional neuroimaging* (New York, Elsevier).

- Lebedev, M.A., Carmena, J.M., O'Doherty, J.E., Zacksenhouse, M., Henriquez, C.S., Principe, J.C., and Nicolelis, M.A.L. (2005). Cortical Ensemble Adaptation to Represent Velocity of an Artificial Actuator Controlled by a Brain-Machine Interface. *J. Neurosci.* *25*, 4681–4693.
- Li, Z., O'Doherty, J.E., Hanson, T.L., Lebedev, M.A., Henriquez, C.S., and Nicolelis, M.A.L. (2009). Unscented Kalman Filter for Brain-Machine Interfaces. *PLOS ONE* *4*, e6243.
- Lin, Z., Zhang, C., Wu, W., and Gao, X. (2007). Frequency recognition based on canonical correlation analysis for SSVEP-based BCIs. *IEEE Transactions on Biomedical Engineering* *54*, 1172–1176.
- Lüdemann-Podubecká, J., Bösl, K., Rothhardt, S., Verheyden, G., and Nowak, D.A. (2014). Transcranial direct current stimulation for motor recovery of upper limb function after stroke. *Neurosci Biobehav Rev* *47*, 245–259.
- Lv, J., Li, Y., and Gu, Z. (2010). Decoding hand movement velocity from electroencephalogram signals during a drawing task. *BioMedical Engineering OnLine* *9*, 64.
- Mancini, M., Pellicciari, M.C., Brignani, D., Mauri, P., Marchis, C.D., Miniussi, C., and Conforto, S. (2015). Automatic artifact suppression in simultaneous tDCS-EEG using adaptive filtering. In *2015 37th Annual International Conference of the IEEE Engineering in Medicine and Biology Society (EMBC)*, pp. 2729–2732.
- Mancini, M., Brignani, D., Conforto, S., Mauri, P., Miniussi, C., and Pellicciari, M.C. (2016). Assessing cortical synchronization during transcranial direct current stimulation: A graph-theoretical analysis. *NeuroImage* *140*, 57–65.
- Mangia, A.L., Pirini, M., and Cappello, A. (2014). Transcranial Direct Current Stimulation and Power Spectral Parameters: a tDCS/EEG co-registration study. *Front. Hum. Neurosci.* *8*, 601.
- Mangia, A.L., Ursino, M., Lannocca, M., and Cappello, A. (2017). Transcallosal Inhibition during Motor Imagery: Analysis of a Neural Mass Model. *Front. Comput. Neurosci.* *11*.
- Maris, E., and Oostenveld, R. (2007). Nonparametric statistical testing of EEG- and MEG-data. *Journal of Neuroscience Methods* *164*, 177–190.
- Massey, F.J. (1951). The Kolmogorov-Smirnov Test for Goodness of Fit. *Journal of the American Statistical Association* *46*, 68–78.
- Matsumoto, J., Fujiwara, T., Takahashi, O., Liu, M., Kimura, A., and Ushiba, J. (2010). Modulation of mu rhythm desynchronization during motor imagery by transcranial direct current stimulation. *J Neuroeng Rehabil* *7*, 27.

- McFarland, D.J., McCane, L.M., David, S.V., and Wolpaw, J.R. (1997a). Spatial filter selection for EEG-based communication. *Electroencephalography and Clinical Neurophysiology* *103*, 386–394.
- McFarland, D.J., McCane, L.M., David, S.V., and Wolpaw, J.R. (1997b). Spatial filter selection for EEG-based communication. *Electroencephalography and Clinical Neurophysiology* *103*, 386–394.
- McFarland, D.J., Miner, L.A., Vaughan, T.M., and Wolpaw, J.R. (2000). Mu and Beta Rhythm Topographies During Motor Imagery and Actual Movements. *Brain Topogr* *12*, 177–186.
- Mehring, C., Rickert, J., Vaadia, E., Cardoso de Oliveira, S., Aertsen, A., and Rotter, S. (2003). Inference of hand movements from local field potentials in monkey motor cortex. *Nat. Neurosci.* *6*, 1253–1254.
- Meyer, B.U., Roricht, S., Graf von Einsiedel, H., Kruggel, F., and Weindl, A. (1995). Inhibitory and excitatory interhemispheric transfers between motor cortical areas in normal humans and patients with abnormalities of the corpus callosum. *Brain* *118*, 429–440.
- Michel, C.M., and Murray, M.M. (2012). Towards the utilization of EEG as a brain imaging tool. *NeuroImage* *61*, 371–385.
- Michel, C.M., Murray, M.M., Lantz, G., Gonzalez, S., Spinelli, L., and Grave de Peralta, R. (2004). EEG source imaging. *Clinical Neurophysiology* *115*, 2195–2222.
- Middendorf, M., McMillan, G., Calhoun, G., Jones, K.S., and others (2000). Brain-computer interfaces based on the steady-state visual-evoked response. *IEEE Transactions on Rehabilitation Engineering* *8*, 211–214.
- Min, B.-K., Marzelli, M.J., and Yoo, S.-S. (2010). Neuroimaging-based approaches in the brain-computer interface. *Trends in Biotechnology* *28*, 552–560.
- Moliadze, V., Antal, A., and Paulus, W. (2010). Electrode-distance dependent after-effects of transcranial direct and random noise stimulation with extracephalic reference electrodes. *Clin Neurophysiol* *121*, 2165–2171.
- Mondini, V., Mangia, A.L., and Cappello, A. (2016). EEG-Based BCI System Using Adaptive Features Extraction and Classification Procedures. *Computational Intelligence and Neuroscience* *2016*, e4562601.
- Mondini, V., Mangia, A.L., and Cappello, A. (2018a). Single-session tDCS over the dominant hemisphere affects contralateral spectral EEG power, but does not enhance neurofeedback-guided event-related desynchronization of the non-dominant hemisphere's sensorimotor rhythm. *PLOS ONE* *13*, e0193004.

- Mondini, V., Mangia, A.L., Talevi, L., and Cappello, A. (2018b). Sinc-Windowing and Multiple Correlation Coefficients Improve SSVEP Recognition Based on Canonical Correlation Analysis. *Computational Intelligence and Neuroscience* 2018.
- Morone, G., Pisotta, I., Pichiorri, F., Kleih, S., Paolucci, S., Molinari, M., Cincotti, F., Kübler, A., and Mattia, D. (2015). Proof of principle of a brain-computer interface approach to support poststroke arm rehabilitation in hospitalized patients: design, acceptability, and usability. *Arch Phys Med Rehabil* 96, S71-78.
- Mueller-Putz, G., Scherer, R., Brunner, C., Leeb, R., and Pfurtscheller, G. (2008). Better than random: A closer look on BCI results. *International Journal of Bioelectromagnetism* 10, 52-55.
- Müller-Gerking, J., Pfurtscheller, G., and Flyvbjerg, H. (1999). Designing optimal spatial filters for single-trial EEG classification in a movement task. *Clinical Neurophysiology* 110, 787-798.
- Müller-Putz, G.R., Scherer, R., Brauneis, C., and Pfurtscheller, G. (2005). Steady-state visual evoked potential (SSVEP)-based communication: impact of harmonic frequency components. *Journal of Neural Engineering* 2, 123-130.
- Müller-Putz, G.R., Schwarz, A., Pereira, J., and Ofner, P. (2016). From classic motor imagery to complex movement intention decoding: The noninvasive Graz-BCI approach. In *Progress in Brain Research*, D. Coyle, ed. (Elsevier), pp. 39-70.
- Mulliken, G.H., Musallam, S., and Andersen, R.A. (2008). Decoding Trajectories from Posterior Parietal Cortex Ensembles. *J. Neurosci.* 28, 12913-12926.
- Nakanishi, M., Wang, Y., Wang, Y.-T., Mitsukura, Y., and Jung, T.-P. (2014). Enhancing unsupervised canonical correlation analysis-based frequency detection of SSVEPs by incorporating background EEG. In *Engineering in Medicine and Biology Society (EMBC), 2014 36th Annual International Conference of the IEEE, (IEEE)*, pp. 3053-3056.
- Nichols, T.E., and Holmes, A. (2001). Nonparametric permutation tests for functional neuroimaging: A primer with examples. *Human Brain Mapping* 15, 1-25.
- Nicolas-Alonso, L.F., and Gomez-Gil, J. (2012). *Brain Computer Interfaces, a Review. Sensors (Basel)* 12, 1211-1279.
- Niedermeyer, E., and Silva, F.H.L. da (2005). *Electroencephalography: Basic Principles, Clinical Applications, and Related Fields (Lippincott Williams & Wilkins)*.
- Nitsche, M.A., and Paulus, W. (2000). Excitability changes induced in the human motor cortex by weak transcranial direct current stimulation. *J. Physiol. (Lond.)* 527 Pt 3, 633-639.

- Nitsche, M.A., and Paulus, W. (2001). Sustained excitability elevations induced by transcranial DC motor cortex stimulation in humans. *Neurology* 57, 1899–1901.
- Nitsche, M.A., Nitsche, M.S., Klein, C.C., Tergau, F., Rothwell, J.C., and Paulus, W. (2003). Level of action of cathodal DC polarisation induced inhibition of the human motor cortex. *Clinical Neurophysiology* 114, 600–604.
- Nolan, H., Whelan, R., and Reilly, R.B. (2010). FASTER: Fully Automated Statistical Thresholding for EEG artifact Rejection. *Journal of Neuroscience Methods* 192, 152–162.
- Notturmo, F., Marzetti, L., Pizzella, V., Uncini, A., and Zappasodi, F. (2014). Local and remote effects of transcranial direct current stimulation on the electrical activity of the motor cortical network. *Hum. Brain Mapp.* 35, 2220–2232.
- Nuwer, M.R., Comi, G., Emerson, R., Fuglsang-Frederiksen, A., Guérit, J.-M., Hinrichs, H., Ikeda, A., Jose C Luccas, F., and Rappelsburger, P. (1998). IFCN standards for digital recording of clinical EEG. *Electroencephalography and Clinical Neurophysiology* 106, 259–261.
- Odom, J.V., Bach, M., Barber, C., Brigell, M., Marmor, M.F., Tormene, A.P., and Holder, G.E. (2004). Visual evoked potentials standard (2004). *Documenta Ophthalmologica* 108, 115–123.
- Ofner, P., and Müller-Putz, G.R. (2012). Decoding of velocities and positions of 3D arm movement from EEG. *Conf Proc IEEE Eng Med Biol Soc* 2012, 6406–6409.
- Ofner, P., and Müller-Putz, G.R. (2015). Using a noninvasive decoding method to classify rhythmic movement imaginations of the arm in two planes. *IEEE Trans Biomed Eng* 62, 972–981.
- Ofner, P., Schwarz, A., Pereira, J., and Müller-Putz, G.R. (2017). Upper limb movements can be decoded from the time-domain of low-frequency EEG. *PLOS ONE* 12, e0182578.
- Okamoto, M., Dan, H., Sakamoto, K., Takeo, K., Shimizu, K., Kohno, S., Oda, I., Isobe, S., Suzuki, T., Kohyama, K., et al. (2004). Three-dimensional probabilistic anatomical cranio-cerebral correlation via the international 10–20 system oriented for transcranial functional brain mapping. *NeuroImage* 21, 99–111.
- Oldfield, R.C. (1971). The assessment and analysis of handedness: the Edinburgh inventory. *Neuropsychologia* 9, 97–113.
- Oostenveld, R., and Praamstra, P. (2001). The five percent electrode system for high-resolution EEG and ERP measurements. *Clinical Neurophysiology* 112, 713–719.

- Pan, J., Gao, X., Duan, F., Yan, Z., and Gao, S. (2011). Enhancing the classification accuracy of steady-state visual evoked potential-based brain-computer interfaces using phase constrained canonical correlation analysis. *J. Neural Eng.* *8*, 036027.
- Paninski, L., Fellows, M.R., Hatsopoulos, N.G., and Donoghue, J.P. (2004). Spatiotemporal Tuning of Motor Cortical Neurons for Hand Position and Velocity. *Journal of Neurophysiology* *91*, 515–532.
- Pascual-Marqui, R.D. (2002). Standardized low-resolution brain electromagnetic tomography (sLORETA): technical details. *Methods & Findings in Experimental & Clinical Pharmacology* *24*, 5–12.
- Pelli, D.G. The VideoToolbox software for visual psychophysics: Transforming numbers into movies. *Spatial Vision* *10*, 437–442.
- Pellicciari, M.C., Brignani, D., and Miniussi, C. (2013). Excitability modulation of the motor system induced by transcranial direct current stimulation: A multimodal approach. *NeuroImage* *83*, 569–580.
- Pfurtscheller, G., and Neuper, C. (1997). Motor imagery activates primary sensorimotor area in humans. *Neuroscience Letters* *239*, 65–68.
- Pfurtscheller, G., and Neuper, C. (2001). Motor imagery and direct brain-computer communication. *Proceedings of the IEEE* *89*, 1123–1134.
- Pfurtscheller, G., and Silva, F.H.L. da (1999). *Event-related Desynchronization* (Elsevier).
- Pfurtscheller, G., Neuper, C., Andrew, C., and Edlinger, G. (1997). Foot and hand area mu rhythms. *International Journal of Psychophysiology* *26*, 121–135.
- Pfurtscheller, G., Müller, G.R., Pfurtscheller, J., Gerner, H.J., and Rupp, R. (2003). 'Thought'-control of functional electrical stimulation to restore hand grasp in a patient with tetraplegia. *Neurosci. Lett.* *351*, 33–36.
- Pfurtscheller, G., Brunner, C., Schlögl, A., and Lopes da Silva, F.H. (2006). Mu rhythm (de)synchronization and EEG single-trial classification of different motor imagery tasks. *NeuroImage* *31*, 153–159.
- Pichiorri, F., Morone, G., Petti, M., Toppi, J., Pisotta, I., Molinari, M., Paolucci, S., Inghilleri, M., Astolfi, L., Cincotti, F., et al. (2015). Brain-computer interface boosts motor imagery practice during stroke recovery. *Ann. Neurol.* *77*, 851–865.
- Pistohl, T., Ball, T., Schulze-Bonhage, A., Aertsen, A., and Mehring, C. (2008). Prediction of arm movement trajectories from ECoG-recordings in humans. *Journal of Neuroscience Methods* *167*, 105–114.

- Polanía, R., Paulus, W., and Nitsche, M.A. (2012). Modulating cortico-striatal and thalamo-cortical functional connectivity with transcranial direct current stimulation. *Human Brain Mapping* 33, 2499–2508.
- Polich, J., Ellerson, P.C., and Cohen, J. (1996). P300, stimulus intensity, modality, and probability. *International Journal of Psychophysiology* 23, 55–62.
- Polikov, V.S., Tresco, P.A., and Reichert, W.M. (2005). Response of brain tissue to chronically implanted neural electrodes. *J. Neurosci. Methods* 148, 1–18.
- Qin, J., Li, Y., and Sun, W. (2007). A Semisupervised Support Vector Machines Algorithm for BCI Systems. *Computational Intelligence and Neuroscience* 2007, e94397.
- Ramoser, H., Muller-Gerking, J., and Pfurtscheller, G. (2000). Optimal spatial filtering of single trial EEG during imagined hand movement. *IEEE Transactions on Rehabilitation Engineering* 8, 441–446.
- Ravden, D., and Polich, J. (1999). On P300 measurement stability: habituation, intra-trial block variation, and ultradian rhythms. *Biological Psychology* 51, 59–76.
- Rivet, B., Souloumiac, A., Attina, V., and Gibert, G. (2009). xDAWN algorithm to enhance evoked potentials: application to brain-computer interface. *Biomedical Engineering, IEEE Transactions On* 56, 2035–2043.
- Robinson, N., and Vinod, A.P. (2016). Noninvasive Brain-Computer Interface: Decoding Arm Movement Kinematics and Motor Control. *IEEE Systems, Man, and Cybernetics Magazine* 2, 4–16.
- Roy, A., Baxter, B., and He, B. (2014). High-definition transcranial direct current stimulation induces both acute and persistent changes in broadband cortical synchronization: a simultaneous tDCS-EEG study. *IEEE Trans Biomed Eng* 61, 1967–1978.
- Salmelin, R., Hämäläinen, M., Kajola, M., and Hari, R. (1995). Functional segregation of movement-related rhythmic activity in the human brain. *Neuroimage* 2, 237–243.
- Schalk, G., Kubánek, J., Miller, K.J., Anderson, N.R., Leuthardt, E.C., Ojemann, J.G., Limbrick, D., Moran, D., Gerhardt, L.A., and Wolpaw, J.R. (2007). Decoding two-dimensional movement trajectories using electrocorticographic signals in humans. *J. Neural Eng.* 4, 264.
- Scherer, R., Müller, G.R., Neuper, C., Graimann, B., and Pfurtscheller, G. (2004). An asynchronously controlled EEG-based virtual keyboard: improvement of the spelling rate. *IEEE Trans Biomed Eng* 51, 979–984.
- Schlaug, G., Renga, V., and Nair, D. (2008). Transcranial direct current stimulation in stroke recovery. *Arch. Neurol.* 65, 1571–1576.

- Schlögl, A., Vidaurre, C., and Müller, K.-R. (2010). Adaptive methods in bci research-an introductory tutorial. In *Brain-Computer Interfaces*, (Springer), pp. 331–355.
- Schwarz, A., Scherer, R., Steyrl, D., Faller, J., and Müller-Putz, G.R. (2015). A co-adaptive sensory motor rhythms Brain-Computer Interface based on common spatial patterns and Random Forest. In *2015 37th Annual International Conference of the IEEE Engineering in Medicine and Biology Society (EMBC)*, pp. 1049–1052.
- Sharbrough, F.W., Chatrian, G.E., Lesser, R.P., Luders, H., Nuwer, M., and Picton, T.W. (1991). Guideline thirteen: Guidelines for standard electrode position nomenclature American Electroencephalographic Society *J Clin Neurophysiol* 1994 11 111 113 8195414. ResearchGate 8, 200--202.
- Shyu, K.-K., Chiu, Y.-J., Lee, P.-L., Liang, J.-M., and Peng, S.-H. (2013). Adaptive SSVEP-based BCI system with frequency and pulse duty-cycle stimuli tuning design. *IEEE Transactions on Neural Systems and Rehabilitation Engineering* 21, 697–703.
- Soekadar, S.R., and Birbaumer, N. (2014). Improving the Efficacy of Ipsilesional Brain-Computer Interface Training in Neurorehabilitation of Chronic Stroke. In *Brain-Computer Interface Research*, C. Guger, B. Allison, and E.C. Leuthardt, eds. (Springer Berlin Heidelberg), pp. 75–84.
- Soekadar, S.R., Witkowski, M., Cossio, E.G., Birbaumer, N., and Cohen, L.G. (2014a). Learned EEG-based brain self-regulation of motor-related oscillations during application of transcranial electric brain stimulation: feasibility and limitations. *Front Behav Neurosci* 8, 93.
- Soekadar, S.R., Witkowski, M., Birbaumer, N., and Cohen, L.G. (2014b). Enhancing Hebbian Learning to Control Brain Oscillatory Activity. *Cereb. Cortex*.
- Soekadar, S.R., Birbaumer, N., Slutzky, M.W., and Cohen, L.G. (2015). Brain-machine interfaces in neurorehabilitation of stroke. *Neurobiology of Disease* 83, 172–179.
- Stagg, C.J., Jayaram, G., Pastor, D., Kincses, Z.T., Matthews, P.M., and Johansen-Berg, H. (2011). Polarity and timing-dependent effects of transcranial direct current stimulation in explicit motor learning. *Neuropsychologia* 49, 800–804.
- Strobbe, G. (2015). Advanced forward models for EEG source imaging. PhD Thesis. Ghent University.
- Suffczynski, P., Kalitzin, S., Pfurtscheller, G., and Lopes da Silva, F.H. (2001). Computational model of thalamo-cortical networks: dynamical control of alpha rhythms in relation to focal attention. *International Journal of Psychophysiology* 43, 25–40.
- Sutter, E.E. (1992). The brain response interface: communication through visually-induced electrical brain responses. *Journal of Microcomputer Applications* 15, 31–45.

- Tadel, F., Baillet, S., Moshier, J.C., Pantazis, D., and Leahy, R.M. (2011). Brainstorm: a user-friendly application for MEG/EEG analysis. *Computational Intelligence and Neuroscience* 2011, 8.
- Tan, D., and Nijholt, A. (2010). Brain-Computer Interfaces and Human-Computer Interaction. In *Brain-Computer Interfaces*, D.S. Tan, and A. Nijholt, eds. (Springer London), pp. 3–19.
- Tazoe, T., Endoh, T., Kitamura, T., and Ogata, T. (2014). Polarity specific effects of transcranial direct current stimulation on interhemispheric inhibition. *PLoS ONE* 9, e114244.
- Teplan, M. (2002). Fundamentals of EEG measurement. *Measurement Science Review* 2, 1–11.
- Tohyama, T., Fujiwara, T., Matsumoto, J., Honaga, K., Ushiba, J., Tsuji, T., Hase, K., and Liu, M. (2011). Modulation of event-related desynchronization during motor imagery with transcranial direct current stimulation in a patient with severe hemiparetic stroke: a case report. *Keio J Med* 60, 114–118.
- Úbeda, A., Hortal, E., Iáñez, E., Perez-Vidal, C., and Azorín, J.M. (2015). Assessing Movement Factors in Upper Limb Kinematics Decoding from EEG Signals. *PLOS ONE* 10, e0128456.
- Urigüen, J.A., and Garcia-Zapirain, B. (2015). EEG artifact removal-state-of-the-art and guidelines. *J Neural Eng* 12, 031001.
- Ursino, M., Magosso, E., and Cuppini, C. (2009). Recognition of Abstract Objects Via Neural Oscillators: Interaction Among Topological Organization, Associative Memory and Gamma Band Synchronization. *IEEE Transactions on Neural Networks* 20, 316–335.
- Ursino, M., Cona, F., and Zavaglia, M. (2010). The generation of rhythms within a cortical region: Analysis of a neural mass model. *NeuroImage* 52, 1080–1094.
- Usakli, A.B. (2010). Improvement of EEG signal acquisition: An electrical aspect for state of the art of front end. *Computational Intelligence and Neuroscience* 2010, 12.
- Vidaurre, C., and Blankertz, B. (2010). Towards a cure for BCI illiteracy. *Brain Topography* 23, 194–198.
- Vidaurre, C., Schlögl, A., Cabeza, R., Scherer, R., and Pfurtscheller, G. (2005). Adaptive on-line classification for EEG-based brain computer interfaces with AAR parameters and band power estimates. *Biomed Tech (Berl)* 50, 350–354.
- Vidaurre, C., Schlogl, A., Cabeza, R., Scherer, R., and Pfurtscheller, G. (2006). A fully on-line adaptive BCI. *Biomedical Engineering, IEEE Transactions On* 53, 1214–1219.

- Vidaurre, C., Cabeza, R., Scherer, R., Pfurtscheller, G., and others (2007). Study of on-line adaptive discriminant analysis for EEG-based brain computer interfaces. *Biomedical Engineering, IEEE Transactions On* 54, 550–556.
- Vidaurre, C., Sannelli, C., Müller, K.-R., and Blankertz, B. (2011a). Co-adaptive calibration to improve BCI efficiency. *J Neural Eng* 8, 025009.
- Vidaurre, C., Kawanabe, M., Von Bunau, P., Blankertz, B., and Muller, K.R. (2011b). Toward unsupervised adaptation of LDA for brain–computer interfaces. *Biomedical Engineering, IEEE Transactions On* 58, 587–597.
- Vines, B.W., Nair, D.G., and Schlaug, G. (2006). Contralateral and ipsilateral motor effects after transcranial direct current stimulation. *Neuroreport* 17, 671–674.
- Vines, B.W., Nair, D., and Schlaug, G. (2008). Modulating activity in the motor cortex affects performance for the two hands differently depending upon which hemisphere is stimulated. *Eur. J. Neurosci.* 28, 1667–1673.
- Wade, D.T., Langton-Hewer, R., Wood, V.A., Skilbeck, C.E., and Ismail, H.M. (1983). The hemiplegic arm after stroke: measurement and recovery. *J. Neurol. Neurosurg. Psychiatry* 46, 521–524.
- Waldert, S., Preissl, H., Demandt, E., Braun, C., Birbaumer, N., Aertsen, A., and Mehring, C. (2008). Hand Movement Direction Decoded from MEG and EEG. *J. Neurosci.* 28, 1000–1008.
- Waldert, S., Pistohl, T., Braun, C., Ball, T., Aertsen, A., and Mehring, C. (2009). A review on directional information in neural signals for brain-machine interfaces. *Journal of Physiology-Paris* 103, 244–254.
- Wang, Y., Gao, S., and Gao, X. (2005). Common Spatial Pattern Method for Channel Selection in Motor Imagery Based Brain-computer Interface. In *Engineering in Medicine and Biology Society, 2005. IEEE-EMBS 2005. 27th Annual International Conference of The*, pp. 5392–5395.
- Wang, Y., Wang, R., Gao, X., Hong, B., and Gao, S. (2006). A practical VEP-based brain-computer interface. *IEEE Transactions on Neural Systems and Rehabilitation Engineering* 14, 234–240.
- Wang, Y., Gao, X., Hong, B., Jia, C., and Gao, S. (2008). Brain-Computer Interfaces Based on Visual Evoked Potentials. *IEEE Engineering in Medicine and Biology Magazine* 27, 64–71.
- Wang, Y., Nakanishi, M., Wang, Y.-T., and Jung, T.-P. (2014). Enhancing detection of steady-state visual evoked potentials using individual training data. In *Engineering in Medicine and Biology Society (EMBC), 2014 36th Annual International Conference of the IEEE, (IEEE)*, pp. 3037–3040.

- Wei, J., Song, Y., Sun, L., and Lv, C. (2013a). Comparison of artificial total disc replacement versus fusion for lumbar degenerative disc disease: a meta-analysis of randomized controlled trials. *International Orthopaedics (SICOT)* 37, 1315–1325.
- Wei, P., He, W., Zhou, Y., and Wang, L. (2013b). Performance of motor imagery brain-computer interface based on anodal transcranial direct current stimulation modulation. *IEEE Trans Neural Syst Rehabil Eng* 21, 404–415.
- Wei, Q., Xiao, M., and Lu, Z. (2011). A comparative study of canonical correlation analysis and power spectral density analysis for ssvep detection. In *Intelligent Human-Machine Systems and Cybernetics (IHMSC), 2011 International Conference On*, (IEEE), pp. 7–10.
- Weiskopf, N., Mathiak, K., Bock, S.W., Scharnowski, F., Veit, R., Grodd, W., Goebel, R., and Birbaumer, N. (2004). Principles of a brain-computer interface (BCI) based on real-time functional magnetic resonance imaging (fMRI). *Biomedical Engineering, IEEE Transactions On* 51, 966–970.
- Winkler, I., Haufe, S., and Tangermann, M. (2011). Automatic classification of artifactual ICA-components for artifact removal in EEG signals. *Behavioral and Brain Functions: BBF* 7, 30.
- Wold, S., Sjöström, M., and Eriksson, L. (2001). PLS-regression: a basic tool of chemometrics. *Chemometrics and Intelligent Laboratory Systems* 58, 109–130.
- Wolpaw, J., and Wolpaw, E.W. (2012). *Brain-Computer Interfaces: Principles and Practice* (Oxford University Press, USA).
- Wolpaw, J.R., and McFarland, D.J. (2004). Control of a two-dimensional movement signal by a noninvasive brain-computer interface in humans. *PNAS* 101, 17849–17854.
- Wolpaw, J.R., Birbaumer, N., Heetderks, W.J., McFarland, D.J., Peckham, P.H., Schalk, G., Donchin, E., Quatrano, L.A., Robinson, C.J., Vaughan, T.M., et al. (2000). Brain-computer interface technology: a review of the first international meeting. *IEEE Transactions on Rehabilitation Engineering* 8, 164–173.
- Wolpaw, J.R., Birbaumer, N., McFarland, D.J., Pfurtscheller, G., and Vaughan, T.M. (2002). Brain-computer interfaces for communication and control. *Clinical Neurophysiology* 113, 767–791.
- Xia, B., Zhang, Q., Xie, H., Li, S., Li, J., and He, L. (2012). A Co-adaptive Training Paradigm for Motor Imagery Based Brain-Computer Interface. In *Advances in Neural Networks – ISNN 2012*, J. Wang, G.G. Yen, and M.M. Polycarpou, eds. (Springer Berlin Heidelberg), pp. 431–439.

- Yekutieli, D., and Benjamini, Y. (1999). Resampling-based false discovery rate controlling multiple test procedures for correlated test statistics. *Journal of Statistical Planning and Inference* *82*, 171–196.
- Yeom, H.G., Kim, J.S., and Chung, C.K. (2013). Estimation of the velocity and trajectory of three-dimensional reaching movements from non-invasive magnetoencephalography signals. *J. Neural Eng.* *10*, 026006.
- Yijun, W., Ruiping, W., Xiaorong, G., and Shangkai, G. (2005). Brain-computer interface based on the high-frequency steady-state visual evoked potential. In *Proceedings. 2005 First International Conference on Neural Interface and Control, 2005.*, pp. 37–39.
- Yuan, P., Chen, X., Wang, Y., Gao, X., and Gao, S. (2015). Enhancing performances of SSVEP-based brain-computer interfaces via exploiting inter-subject information. *Journal of Neural Engineering* *12*, 046006.
- Zhang, Y., Zhou, G., Zhao, Q., Onishi, A., Jin, J., Wang, X., and Cichocki, A. (2011). Multiway Canonical Correlation Analysis for Frequency Components Recognition in SSVEP-Based BCIs. In *Neural Information Processing*, B.-L. Lu, L. Zhang, and J. Kwok, eds. (Springer Berlin Heidelberg), pp. 287–295.
- Zhang, Y., Xu, P., Liu, T., Hu, J., Zhang, R., and Yao, D. (2012). Multiple Frequencies Sequential Coding for SSVEP-Based Brain-Computer Interface. *PLOS ONE* *7*, e29519.
- Zhang, Y., Zhou, G., Jin, J., Wang, M., Wang, X., and Cichocki, A. (2013). L1-Regularized Multiway Canonical Correlation Analysis for SSVEP-Based BCI. *IEEE Transactions on Neural Systems and Rehabilitation Engineering* *21*, 887–896.
- Zhang, Y., Zhou, G., Jin, J., Wang, X., and Cichocki, A. (2015). SSVEP recognition using common feature analysis in brain-computer interface. *Journal of Neuroscience Methods* *244*, 8–15.
- Zhang, Y.U., Zhou, G., Jin, J., Wang, X., and Cichocki, A. (2014). Frequency recognition in SSVEP-based BCI using multiset canonical correlation analysis. *International Journal of Neural Systems* *24*, 1450013.
- Zhu, D., Bieger, J., Molina, G.G., and Aarts, R.M. (2010). A survey of stimulation methods used in SSVEP-based BCIs. *Computational Intelligence and Neuroscience* *2010*, 1.